

# **Design and Fabrication Of Tissue-like Phantoms for use in Biomedical Imaging**



**UNIVERSITY OF  
KWAZULU - NATAL**

---

**INYUVESI  
YAKWAZULU-NATALI**

Lindokuhle Charles Ntombela



August, 2022

# **Design and Fabrication Of Tissue-like Phantoms for use in Biomedical Imaging**

by

Lindokuhle Charles Ntombela (214512440)

A thesis submitted to the  
University of KwaZulu-Natal  
in fulfilment of the requirements for the degree  
of  
DOCTOR OF SCIENCE  
in  
PHYSICS

Thesis Supervisor: Prof Naven Chetty

Thesis Co-supervisor: Dr Bamise Adeleye

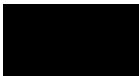


UNIVERSITY OF KWAZULU-NATAL  
SCHOOL OF CHEMISTRY AND PHYSICS  
PIETERMARITZBURG CAMPUS, SOUTH AFRICA

## Declaration - Plagiarism

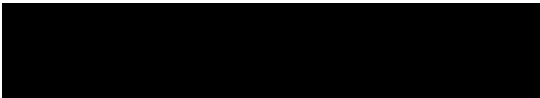
I, Lindokuhle Charles Ntombela (214512440), declare that

1. The research reported in this thesis, except where otherwise indicated, is my original research.
2. This thesis has not been submitted for any degree or examination at any other university.
3. This thesis does not contain other persons' data, pictures, graphs or other information, unless specifically acknowledged as being sourced from other persons.
4. This thesis does not contain other persons' writing, unless specifically acknowledged as being sourced from other researchers. Where other written sources have been quoted, then
  - (a) their words have been re-written but the general information attributed to them has been referenced, or
  - (b) where their exact words have been used, then their writing has been placed in italics and referenced.
5. This thesis does not contain text, graphics or tables copied and pasted from the internet, unless specifically acknowledged, and the source being detailed in the thesis and in the reference sections.

  
\_\_\_\_\_  
Signed: Lindokuhle Charles Ntombela (214512440) (Student)

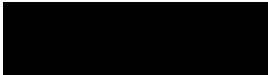
24/01/2023

\_\_\_\_\_  
Date

  
\_\_\_\_\_  
Signed: Prof Naven Chetty (Supervisor)

24/01/2023

\_\_\_\_\_  
Date

  
\_\_\_\_\_  
Signed: Dr Bamise Adeleye (Co-supervisor)

24/01/2023

\_\_\_\_\_  
Date

## **Disclaimer**

This document describes work undertaken as a Doctoral programme of study at the University of KwaZulu-Natal (UKZN). All views and opinions expressed therein remain the sole responsibility of the author, and do not necessarily represent those of the institution.

# Declaration 2: Publications

This thesis consists of two manuscripts, the first paper is published, and the second is under review. The first author (student) contributed towards experimental work, data collection, and manuscript preparation guided by the supervisors.

## Publication (CHAPTER 5)

1. Lindokuhle Ntombela, Naven Chetty, Bamise Adeleye. Effective attenuation coefficient and penetration depth of 630nm laser light in polyvinyl alcohol slime glue phantoms simulating the human brain tumour. *Proceedings of the Estonian Academy of Sciences*, 2022, 3, **71**, 221-226.

## Publication (CHAPTER 6)

1. Lindokuhle Ntombela, Naven Chetty, Bamise Adeleye, 2022. Realistic deformable phantoms with optical properties of human tissues for biomedical research applications. *Result in optics, journal*. (Under review)

# Abstract

The continuous need for tissue-like samples to understand biological systems and the development of new diagnostic and therapeutic applications has led to the adoption of tissue models using potential materials. This work presents a low-cost method for manufacturing PVA slime glue-based phantoms to replicate diseased and healthy biological tissues' optical, mechanical, and structural properties. The deformable phantoms with complex geometries are vital to model tissues' anatomic shapes and chemical composition. Absorption and scattering properties were set by adding black India ink and aluminium oxide ( $\text{Al}_2\text{O}_3$ ) particles in varying quantities to obtain slime phantom tissues with optical properties of the brain, malignant brain tumour, lung carcinoma, and post-menopausal uterus. The phantom properties were characterized and validated using a He-Ne laser emitting at 532 nm and 630 nm wavelengths propagated through various thicknesses of the fabricated phantom. The incident and transmitted intensity were measured to determine the absorption coefficient ( $\mu_a$ ) and scattering coefficient ( $\mu_s$ ).

Furthermore, the effective attenuation coefficient ( $\mu_{eff}$ ) and penetration depth ( $\delta$ ) were deduced from the reduced scattering coefficient ( $\mu'_s$ ) and the anisotropy factor ( $g$ ) obtained through the scattering phase function and Wolfram Mathematica. The anisotropy factor demonstrated a forward scatter, typical of strongly scattering media as real tissues. Such geometrically and optically realistic phantoms would function as effective tools for developing techniques in diagnostic and therapeutic applications such as laser ablation and PDT cancer treatment.

# Acknowledgements

I am highly indebted to my Supervisors Prof Naven Chetty and Dr Bamise Adeleye for their patience and guidance in the course of this study and ensuring that highest standard was maintained throughout. They consistently allowed this study to be my own work, but steered me in the right direction whenever needed.

Other acknowledgments deserve mention, Messrs Mzungezi Mthembu and Ravin Sivraman staffs of the Physics departments Pietermaritzburg campus, for assistance with equipment and their general encouragement.

Lastly, I truly appreciate my friends and family for their support and best wishes.

Lindokuhle Ntombela

# Contents

	<b>Page</b>
<b>List of Figures</b>	<b>viii</b>
<b>List of Tables</b>	<b>x</b>
<b>Abbreviations</b>	<b>xi</b>
<b>Chapter 1: Introduction</b>	<b>1</b>
1.1 Lasers For Imaging Applications . . . . .	5
1.1.1 Therapeutic radiation . . . . .	5
1.1.2 Photodynamic therapy (PDT) . . . . .	5
1.1.3 Tissue welding . . . . .	5
1.1.4 Surgery . . . . .	6
1.2 Significance of the study . . . . .	6
1.3 Aims and objectives . . . . .	7
1.4 Organization of the thesis . . . . .	7
<b>Chapter 2: Theory</b>	<b>9</b>
2.1 Optical Properties of Light in Tissues . . . . .	9
2.1.1 Scattering . . . . .	11
2.1.2 Absorption . . . . .	14
2.1.3 Transmission of Laser Light . . . . .	16
2.2 Light Distribution in Tissue . . . . .	17
2.2.1 Total and Effective Attenuation Coefficient . . . . .	17
2.2.2 Reduced Scattering Coefficient . . . . .	17
2.2.3 Anisotropy Factor ( $g$ ) . . . . .	17
2.2.4 Transport Mean Free Path . . . . .	18
2.2.5 Penetration Depth . . . . .	18
2.2.6 Optical Albedo . . . . .	19
2.3 Scattering Particles . . . . .	19



2.3.1	Single and Multiple Scattering . . . . .	20
2.4	Scattering Function at Small Scattering Angles . . . . .	22
2.5	Light Propagation Models in Tissues . . . . .	23
2.5.1	The Radiative Transfer Equation . . . . .	23
2.5.2	Diffusion Equation Formalism . . . . .	24
2.5.3	Kubelka-Munt (KM) Theory . . . . .	25
2.5.4	Monte Carlo . . . . .	27
2.5.5	Beer-Lambert Law . . . . .	29
2.6	Laser Light Properties . . . . .	29
2.7	Characteristics and Properties of Biological Tissue . . . . .	31
2.7.1	Skin Tissue . . . . .	31
2.7.2	Brain Tissue . . . . .	32
2.7.3	Malignant Brain Tumor . . . . .	33
2.7.4	Lung Carcinoma . . . . .	33
2.7.5	Post-menopausal Uterus . . . . .	34
2.8	Optical Tissue-Equivalent Phantoms . . . . .	34
<b>Chapter 3:</b>	<b>Experimental Details</b>	<b>36</b>
3.1	Optical Tissue Phantom Composition . . . . .	36
3.1.1	Bulk Matrix Material . . . . .	36
3.1.2	Absorbing Media . . . . .	37
3.1.3	Scattering Particles . . . . .	37
3.2	Optical Properties Measuring Apparatus . . . . .	37
3.2.1	The Helium-Neon (He-Ne) Laser . . . . .	37
3.2.2	Laser Meter . . . . .	38
3.2.3	Digital Vernier Caliper . . . . .	38
3.3	Experimental Procedures . . . . .	39
3.3.1	Fabrication Process of the Slime Phantom Tissue . . . . .	39
3.3.2	Slime Phantom Recipe Summary . . . . .	40
3.3.3	Experimental set-up . . . . .	41
3.3.4	Measurements of Optical Properties . . . . .	42
<b>Chapter 4:</b>	<b>Results</b>	<b>43</b>
4.1	Brain Samples . . . . .	43
4.1.1	Analysis of brain slime phantom samples . . . . .	46
4.2	Lung carcinoma Samples . . . . .	48
4.2.1	Analysis of lung carcinoma slime phantom samples . . . . .	50

4.3	Post-menopausal uterus Samples . . . . .	51
4.3.1	Analysis of post-menopausal uterus slime phantom samples . . . . .	53
4.4	Malignant brain tumor Samples . . . . .	55
4.4.1	Analysis of malignant brain tumor slime phantom samples . . . . .	57
4.5	Source of Errors . . . . .	58
<b>Chapter 5: Effective Attenuation Coefficient and Penetration Depth of 630nm Laser Light In Polyvinyl Alcohol Slime Glue Phantoms Simulating the Human Brain Tumour</b>		<b>59</b>
5.1	INTRODUCTION . . . . .	61
5.2	MATERIALS AND METHODS . . . . .	63
5.2.1	Phantom composition and recipe . . . . .	63
5.2.2	Measurements of Optical Properties . . . . .	64
5.3	RESULTS AND DISCUSSION . . . . .	65
5.4	CONCLUSION . . . . .	69
<b>Chapter 6: Realistic deformable phantoms with optical properties of human tissues for biomedical research applications</b>		<b>70</b>
6.1	INTRODUCTION . . . . .	72
6.2	Experimental procedure . . . . .	74
6.2.1	Phantoms materials . . . . .	74
6.2.2	Measurements of Optical Properties . . . . .	75
6.3	Results and discussion . . . . .	77
6.4	CONCLUSION . . . . .	81
<b>Chapter 7: Conclusion and Future work</b>		<b>83</b>
<b>References</b>		<b>98</b>
<b>References</b>		<b>98</b>

# List of Figures

Figure 2.1	Optical Properties of Light in Biological Tissues [53]. . . . .	10
Figure 2.2	Spectrophotometer [54]. . . . .	10
Figure 2.3	Attenuation of laser light through a scattering medium. . . . .	11
Figure 2.4	Light absorption in a phantom tissue. . . . .	15
Figure 2.5	Transmission of light through tissue [61, 62]. . . . .	16
Figure 2.6	Different values of the anisotropy factor. . . . .	18
Figure 2.7	Schematic representation of a photon penetration depth inside a tissue. . . .	19
Figure 2.8	The light energy flow inside the tissue [81]. . . . .	23
Figure 2.9	Random movements of the photon in biological tissue [87]. . . . .	27
Figure 2.10	Stochastic parameters controlling the incident photon movement . . . . .	28
Figure 2.11	The Beer-Lambert Law [90]. . . . .	29
Figure 2.12	Diagram of the four-level energy [91]. . . . .	30
Figure 2.13	Layers of the skin [92]. . . . .	32
Figure 3.1	A Laser Meter. . . . .	38
Figure 3.2	Digital Vernier Caliper. . . . .	39
Figure 3.3	Slime Phantom Samples . . . . .	41
Figure 3.4	The set-up of apparatus for this experiment. . . . .	42
Figure 4.1	A sample calculation of anisotropy factor( $g$ ) using Wolfram Mathematica. .	44
Figure 4.2	Graph of $-\ln\left(\frac{P}{P_0}\right)$ vs $L$ to determine the attenuation coefficient $\mu_t$ , represented by the slope in the equation of the linear fit. . . . .	45
Figure 4.3	Graph of $-\ln\left(\frac{P}{P_0}\right)$ vs $L$ to determine the attenuation coefficient $\mu_t$ , represented by the slope in the equation of the linear fit. . . . .	46

Figure 4.4	Graph of $-\ln\left(\frac{P}{P_0}\right)$ vs $L$ to determine the attenuation coefficient $\mu_t$ , represented by the slope in the equation of the linear fit. . . . .	48
Figure 4.5	Graph of $-\ln\left(\frac{P}{P_0}\right)$ vs $L$ to determine the attenuation coefficient $\mu_t$ , represented by the slope in the equation of the linear fit. . . . .	49
Figure 4.6	Graph of $-\ln\left(\frac{P}{P_0}\right)$ vs $L$ to determine the attenuation coefficient $\mu_t$ , represented by the slope in the equation of the linear fit. . . . .	52
Figure 4.7	Graph of $-\ln\left(\frac{P}{P_0}\right)$ vs $L$ to determine the attenuation coefficient $\mu_t$ , represented by the slope in the equation of the linear fit. . . . .	53
Figure 4.8	Graph of $-\ln\left(\frac{P}{P_0}\right)$ vs $L$ to determine the attenuation coefficient $\mu_t$ , represented by the slope in the equation of the linear fit. . . . .	55
Figure 4.9	Graph of $-\ln\left(\frac{P}{P_0}\right)$ vs $L$ to determine the attenuation coefficient $\mu_t$ , represented by the slope in the equation of the linear fit. . . . .	56
Figure 5.1	Set-up for measurement of optical properties. . . . .	64
Figure 5.2	The logarithmic intensity as a function of thickness with associated linear fitting options to determine the total attenuation coefficient for the pure slime phantom at 630 nm. . . . .	66
Figure 5.3	The logarithmic intensity as a function of thickness with associated linear fitting options to determine the total attenuation coefficient for the slime phantom with absorbers at 630 nm. . . . .	67
Figure 6.1	Schematic illustration of the procedure involved in laser irradiation of phantom slime samples. . . . .	75
Figure 6.2	The logarithmic intensity as a function of thickness to determine the total attenuation coefficient for lung carcinoma slime phantom. . . . .	78
Figure 6.3	Graph of logarithmic intensity data as a function of thickness to determine the total attenuation coefficient for the post-menopausal uterus slime phantom. . .	79
Figure 6.4	Graph of logarithmic intensity data as a function of thickness to determine the total attenuation coefficient for brain tumour slime. . . . .	80

# List of Tables

Table 3.1	Slime phantom recipes with the wavelengths and mimicked tissue types. . .	41
Table 4.1	The power intensities of the 532 nm laser through a pure slime phantom sample, obtained by mixing 30g/l concentration of borax with 100 ml of PVA slime glue. . . . .	44
Table 4.2	The power intensities of the 532 nm laser through the same mixture of 30g/l concentration of borax with 100 ml of PVA slime glue, and 0.4 ml of India Ink, to assess the effects of adding absorbers on total attenuation coefficients. . . . .	45
Table 4.3	The results obtained by calculation and graphically from the slope of the best fit line. . . . .	46
Table 4.4	The power intensities of the 630 nm laser through a pure slime phantom sample, obtained by mixing 30g/l concentration of borax with 100 ml of PVA slime glue. . . . .	48
Table 4.5	The power intensities of the 630 nm laser through the same mixture of 30g/l concentration of borax with 100 ml of PVA slime glue, and 0.6 ml of India Ink, to assess the effects of adding absorbers on total attenuation coefficients. . . . .	49
Table 4.6	The results obtained by calculation and graphically from the slope of the best fit line. . . . .	50
Table 4.7	The power intensities of the 630 nm laser through a mixture of 30g/l concentration of borax with 100 ml of PVA slime glue and 0.4 ml of $Al_2O_3$ , to assess the effects of adding scatterers on total attenuation coefficients. . . . .	51
Table 4.8	The power intensities of the 630 nm laser through the same mixture of 30g/l concentration of borax with 100 ml of PVA slime glue, 0.4 ml of $Al_2O_3$ and 0.4 ml of India Ink, to assess the effects of adding scatterers and absorbers on total attenuation coefficients. . . . .	52
Table 4.9	The results obtained by calculation and graphically from the slope of the best fit line. . . . .	53
Table 4.10	The power intensities of the 630 nm laser through a mixture of 60g/l concentration of borax with 100 ml of PVA slime glue. . . . .	55

---

Table 4.11	The power intensities of the 630 nm laser through the same mixture of 60g/l concentration of borax with 100 ml of PVA slime glue, and 0.4 ml of India Ink, to assess the effects of adding absorbers on total attenuation coefficients. . . . .	56
Table 4.12	The results obtained by calculation and graphically from the slope of the best fit line. . . . .	57
Table 5.1	The power intensities of the 630 nm laser through a mixture of 60g/l concentration of borax with 100 ml of PVA slime glue. . . . .	66
Table 5.2	The power intensities of the 630 nm laser through the 60g/l concentration of borax with 100 ml of PVA slime glue, and 0.4 ml of India Ink, to assess the effects of adding absorbers on total attenuation coefficients. . . . .	67
Table 5.3	Comparison of effective attenuation coefficient and penetration depth values in this study with other work at 630 nm. . . . .	68
Table 6.1	PVA Slime phantom recipes with tissue at different wavelengths. . . . .	75
Table 6.2	The power intensities through different thicknesses of the lung carcinoma slime phantom. . . . .	78
Table 6.3	The power intensities through different thicknesses of the post-menopausal uterus slime phantom. . . . .	79
Table 6.4	The power intensities through different thicknesses of the brain tumour slime phantom. . . . .	80
Table 6.5	Optical coefficients of fabricated tissues at 630 nm from this study . . . . .	81
Table 6.6	Optical properties reported for fabricated tissues in Literature at 630 nm. . .	81

# Abbreviations

CCD	-	Charge-Coupled Device.
CT	-	Computed Tomography.
DNA	-	Deoxyribonucleic Acid.
H-G	-	Henry-Greenstein.
He-Ne	-	Helium-Neon.
IR	-	Infrared Radiation.
KM	-	Kubelka-Munt.
LILT	-	Low Intensity Laser Therapy.
LITT	-	Laser Interstitial Thermo Therapy.
LLLT	-	Lower Level Laser Therapy.
MC	-	Monte Carlo.
MFP	-	Mean Free Path.
MR	-	Magnetic Resonance.
MRI	-	Magnetic Resonance Imaging.
MRS	-	Magnetic Resonance Spectroscopy.
NIR	-	Near-Infrared.
OD	-	Optical Density.
OCT	-	Optical Coherence Tomography.
PDMS	-	Poly (vinyl alcohol).
PDT	-	Photodynamic Therapy.
PEO	-	Poly (ethylene oxide).
PET	-	Positron Emission Tomography.
PUVA	-	Psoralen UltraVioletA.
PVA	-	Polyvinyl Alcohol.
PVC	-	Polyvinyl Chloride.
R	-	Reflectance.
RTE	-	Radiative Transfer Equation.
SAR	-	Specific Absorption Rate.
SPECT	-	Single-Photon Emission Computed Tomography.
T	-	Transmittance.
TSE	-	Turbo Spin Echo.
US	-	UltraSound.
UV	-	Ultraviolet.

# Chapter 1

## Introduction

Recent advances in biomedical tissue optics involving tissue characterization with laser radiation are gaining significance as a tool for early diagnosis of pathological changes in biological tissues [1]. This progress yielding new and powerful biomedical imaging methods of investigating tissues from single molecules to specific organs, identify bimolecular distributions within cells, in vivo imaging of enzymes pathways, and selective treatment of tumors [2]. It involves modalities, such as optical imaging, positron emission, computed tomography, magnetic resonance imaging, and conventional radiography [3–5], among others that map a functional and anatomical cross-sectional image of the biological tissues and their basic structure [6]. Each modality holds unique characteristics in the diagnosis of a particular disease. However, several imaging modalities are needed to visualize and diagnose more than one region of the tissue. The imaging techniques' primary dissimilarity is the energy source employed to produce the images [7].

Biomedical imaging is a powerful improving molecular diagnostic method that uses photons' visible light to create images of various organs and tissues together with smaller structures (molecules and cells) [8]. These tissues are typically mimicked and modeled with tissue-like materials due to the limited availability for ethical reasons and the complexities of actual biological tissues [9, 10]. Specifically, in biomedical imaging, the tissue phantoms are adopted to validate systems and procedures for imaging a specific area of tissues. The tissue-equivalent phantom consists of a bulk material to which scattering agents and absorbing agents were added to form a complete tissue phantom [11]. These materials are selected based on similarities to biological tissues in optical properties, particularly scattering and absorption coefficients, and structural characteristics, such as density, stretching strength, and hardness. This includes other properties defining the optical phantom's suitability and usefulness, such as stability and ease of production [12].



---

Currently, biomedical imaging techniques are increasing rapidly as non-invasive medical therapy and diagnostic tools [12]. This is a consequence of the continuous use of optical phantoms as the tissue replica to study light transport in complex and multi-layered tissues and organs [13, 14]. Moreover, optical phantoms are employed in numerous studies focusing on the precise tracking of metabolites utilized as biomarkers for disease identification, progression, and treatment response [15]. These methods and processes have significantly reduced biological tissue's exposure to harmful radiations and controlled specific damages in the irradiated tissues [16].

Additionally, optical phantoms are desired to understand lesions of healthy biological tissues caused by radiation during various cancer treatments, such as hyperthermia (heating the tumor region by electromagnetic radiation in the near-infrared range). Kato et al. [17] designed optical phantom with the same electric properties as actual tissue under a range (5-40 MHz) to model and optimize cancer-treating modality (Hyperthermia). The phantom created with agar powder, sodium azide ( $\text{NaN}_3$ ), and polyvinyl chloride (PVC) showed electrical conductivity ( $0.02 - 1.23 \text{ Sm}^{-1}$ ) and permittivity ( $35 - 80$ ) similar to human tissues. It was stable for over a year in the heating experiment with no deterioration with the  $\text{NaN}_3$  essentially acting as a preservative.

In 1997, Georges et al. [18] presented optical phantoms with scattering and absorption coefficients equivalent to the actual biological tissues in a broad spectral (400-650nm). The phantoms were composed of agarose and various amounts of particles such as intralipid, ink, blood, and azide for light absorption and scattering. Photosensitizers and fluorochromes were added to simulate a cancer photodetection procedure. The fabricated tissues efficiently accessed and compared various cancer photodetection procedures utilizing light-induced fluorescence. The main limitations of this approach were the short lifetime and the probable variations in optical properties due to the imperfect reproducibility of the preparation process [19].

Firbank and Delpy described a method to machine a solid inhomogeneous phantom with resin as base material, organic dye as absorber, and titanium dioxide particle as scatterer for use in NIR spectroscopy and imaging [9]. The phantom was effectively used for imaging purposes, however the settling of scattering and absorbing substances in the resin caused unwanted spatial variations of the phantom optical properties [9].

---

A different approach by Cubeddu et al. (1997) [19], involves a solid tissue phantom made of agar, intralipid and black ink. The homogeneity of the agar phantom was superior since both ink and intralipid are well dissolved and dispersed in the agar solution [19]. The phantom can become a proper hardening with stable optical properties. The phantom characterized using time-resolved transmittance measurements was found to be stable in its optical properties and typical of biological tissues in the red and near-infrared. The values of the optical parameters reported were typical for biological tissues in the red and near-infrared. The phantom nonetheless requires antibiotics to increase its life [19].

By May 2000, Nelson et al. [20] developed and evaluated a tissue phantom for experimental studies in Laser Interstitial Thermo Therapy (LITT) and treatment of small breast tumors at 980 nm. The tissue phantoms consist of a polyacrylamide hydrogel matrix with different scatterer (Intralipid 10%) and absorber (Nigrosin) concentrations for adjustable optical properties. The phantoms had temperature curves comparable to those in the ex-vivo tissue and were valuable for determining optimum laser treatment parameters in laser interstitial thermotherapy of breast cancer.

Optical tissue-like phantoms closely matching the human skin's characteristics (averaged for 260 patients) over a range of wavelengths (400-1000 nm) were simulated by Manuela et al. [21]. The phantoms consist of suitably adjusted amounts of transparent silicone,  $\text{Al}_2\text{O}_3$  particles, and cosmetic powder. Furthermore, the applicability to numerous light tissue interactions validated the correctability of the phantoms.

Srinivasan et al. [1] attempt to measure the optical scattering of various biological organs using a laser reflectometer and tissue-like phantoms composed of paraffin wax material. Three parameters, namely reduced scattering ( $\mu'_s$ ), anisotropy factor ( $g$ ), and absorption coefficient ( $\mu_a$ ), were determined by the Monte Carlo Simulation method. The created phantoms were useful for optical imaging of diseased and healthy organs.

A recipe of highly compressible polyvinyl alcohol (PVA) slime phantoms for diffuse optical tomography was presented by Hebden et al. (2006) [22]. The created phantoms were deformable to different tissue geometries, but their long-term stability is still undetermined, and the results were not conclusive due to the small number of phantoms studied.

Bergamn et al. [23] developed a skin phantom with behenic acid, cholesterol, and ceramides as the epidermis. Fluorescent dyes were used to achieve optical prop-

---

erties of the skin tissue with the optical coefficients measured by reflectance-based confocal microscopy and fluorescence technique.

Portakal et al. [24] aimed to fabricate tissue-equivalent for relaxometry, non-Gaussian diffusion imaging, and ultrasound elastography. They compared parameters for cancer patients such as prostate condition. The tissue manufactured with agar gel of various concentrations successfully mimicked the MRI and elastography parameters similar to those found in the healthy and diseased prostate.

Yusoff et al. (2019) recently produced MRI phantoms considering potentially new and cheap slime material for their suitability and capability [25]. The slime phantoms were prepared by mixing polyvinyl alcohol (PVA) glue and distilled water with various borax concentrations,  $\rho = 0.0075$  g/ml, 0.0125 g/ml, 0.0175 g/ml, and 0.0225 g/ml. The longitudinal relaxation time (T1) and transverse relaxation time (T2) images were monitored by a 3-T MRI through a turbo spin echo pulse (TSE) sequence for homogeneity. The (T1 and T2) images showed good agreement with average values of human tissues and were stable for 7 days after preparations [25]. However, the experimental technique was not sufficient enough to quantitatively determine its homogeneity and stability [25]. Furthermore, the high cost of phantom tissue creation and the laborious nature of the method proposed is not suitable for several phantoms [25].

Laser radiation plays a crucial role in medical systems for therapy, tissue welding, and surgery (soft tissue cutting and blood coagulation) [26–28]. A laser stimulates atoms or molecules to emit light with a narrow wavelength spectrum or coherent light, defining the laser's power (energy). Due to their coherent nature, all laser lights cause an increase in light interference patterns and dark bands as the relative path lengths varied. This is a valuable property in medical diagnostics as the total energy across the pattern inside biological tissues remains the same with no light disturbance caused by the interference [29, 30].

The optimal use of laser light as a therapeutic, surgical, and diagnostic modality commonly entails understanding the optical properties of various tissues involved in the process [31]. The optical properties (absorption, scattering, refraction, and reflection) are crucial for describing light propagation through biological tissue and provide vital information about the tissue's state [31]. The laser energy also modifies tissue structure in photothermal and photochemical processes during medical treatments depending on the power level [32]. However, knowledge of all-optical effects of various tissues to an incident laser beam and the damage of the absorbed

radiation by different target tissue is of paramount importance [31]. The knowledge of absorption levels gives a good understanding of laser choice for a specific application. It makes it possible to precisely control the tissue's thermal energy and circumscribe the effects to the treated volume [31]. This is aided by the laser output radiation's critical characteristics, including working modes, intensity, and possible interaction time interval [33, 34].

## **1.1 Lasers For Imaging Applications**

### **1.1.1 Therapeutic radiation**

Radiation therapy generally involves ionizing radiation, as part of cancer treatment, by controlling or killing malignant cells [26]. The radiation stimulates tissue healing while helping resolve pain and inflammation [26]. The photon energy of the radiation changes essential biomolecules such as protein, collagen, and DNA and modifies cell metabolism. This mechanism expands cell replication capability and stimulates various tissue cells for reproduction [26].

### **1.1.2 Photodynamic therapy (PDT)**

Photodynamic therapy (PDT) is a powerful modality involving the distribution of photosensitizing agents into the body (bloodstream) [27]. These chemical agents are absorbed in normal and cancerous tissues with oxygen yield in the cancerous environment [27]. The interaction between the light of a particular frequency and the body activates photosensitising agents, causing photochemical reactions, effectively killing the cancerous cells without undue typical tissue injury [35]. The photosensitizer distribution varies depending on the treated tissue's characteristics, the incident light's wavelengths, optical scattering within the tissue, and light absorption by the sensitizing agent [36, 37]. The deposited light energy is the PDT dose, which is directly proportional to the product of the photosensitizer absorption coefficient and the light fluence [36].

The primary light sources for PDT are broad-spectrum lamps, diode lamps, and lasers. These sources emit large radiation fields with deeper penetration, enabling deeper areas of cancerous tissue treatment [38, 39].

### **1.1.3 Tissue welding**

Tissue welding is a relatively new conventional technique aiming to seal surgical wound sites using laser light without sutures. It depends on the coagulation of an

organic soldering material of two tissue parts binding them until the tissue heals [28]. This technique brings innovative settings where suturing difficulties such as endoscopic interventions are managed [40]. It is also effective for blood vessel and nerve bundle anastomosis [41, 42]. However, water tightness of tissue closure is essential for neurosurgical procedures and cardiovascular surgery. Therefore, laser tissue welding intervenes to repair cerebrospinal fluid leaks. The most common lasers for successful tissue welding are CO<sub>2</sub> (10600 nm) and Nd:YAG (1064 nm), including the Ultrapulsed diode (980 nm) [43, 44].

#### **1.1.4 Surgery**

##### **Soft tissue cutting (incision)**

Most surgical branches employ a high-power laser instead of a knife and ablate to cut soft tissues with photothermal effects. The heat reproduction capability of lasers is functional and demanded in practical surgical applications. The beam's thermal effect on the targeted area enables the suitability of high-power lasers as a surgical tool for cutting precisely the tissue at smaller spot sizes [45]. As a result, employing erbium lasers during incision on the mucosa (water-rich component) is advantageous to other wavelengths based on its low collateral thermal effect and high specificity [46]. Furthermore, surgical procedures in ophthalmology, and incision geometry, demand high precision for transparent tissue at a specific depth [47].

##### **Blood coagulation (hemostasis)**

In hemostasis, the laser's wavelength coagulates the blood and stops bleeding with its photothermal efficiency. This provides a clear vision for the surgeon and less edema in regions such as the oral cavity with high bleeding tendency [48–50]. Moreover, laser use in coagulation is vital for scalpel surgery and in patients receiving anticoagulant therapy due to its blood-stopping effect [51, 52].

## **1.2 Significance of the study**

The construction of multi-layered tissue-like phantoms with relatively inexpensive preparation and optical properties determination technique is beneficial for quick evaluation and standardization of medical devices and procedures.

Additionally, phantom creation is significant for minimally invasive surgical training, understanding underlying anomalies in the planning of complex surgery, and

improving clinical outcomes.

The cost-effective recipe presented handles the creation and evaluation of tissue simulating phantoms made up of PVA gel, aluminium oxide ( $Al_2O_3$ ), and Indian ink as scatterer and absorber, respectively. The primary matrix (polyvinyl alcohol (PVA) slime) and borax powder (relaxation modifier) including the beam splitter and laser check meter for the power intensities through each sample slice was locally purchased.

Furthermore, the optical properties of the fabricated tissue, namely the absorption coefficient  $\mu_a$ , the scattering coefficient  $\mu_s$ , the reduced scattering coefficient  $\mu'_s = \mu_s(1 - g)$ , the effective attenuation coefficient  $\mu_{eff}$ , and the anisotropy factor  $g$ , respectively were determined following basic ray optics technique. Consequently, a procedure for developing optical tissue phantoms based on PVA with desired optical properties was found.

### 1.3 Aims and objectives

The principal objectives of this study are to:

- produce tissue phantoms using a potentially new material called slime.
- investigate the relevant optical characteristics of the slime phantom at a specific wavelength.
- develop a low-cost modality of simulating optical tissue-like phantoms for biomedical imaging.
- fabricate tissue-like phantoms with controllable and adjustable scattering and absorption properties.
- create a phantom type that can be easily deformed and compressed with optical properties appropriate to actual human tissue for developing therapeutic protocols.

### 1.4 Organization of the thesis

- **Chapter 1:** This chapter presented the background for this work and concluded by describing the significance and aims of the study.
- **Chapter 2:** The knowledge and formalism required to understand tissue optics and different approaches for determining the optical properties of biological tissues were provided in this chapter.

- **Chapter 3:** Presents the experimental procedures and apparatus utilized in fabricating the optical tissues from this study.
- **Chapter 4:** This chapter provides the experimental results with analysis and probable sources of errors during the study.
- **Chapter 5:** Is a published manuscript in the Proceedings of the Estonian Academy of Sciences. The study investigates Effective Attenuation Coefficient and Penetration Depth of 630 nm Laser Light In Polyvinyl Alcohol Slime Glue Phantoms Simulating the Human Brain Tumour. The conclusions feed into efforts at obtaining deformable and compressible tissue phantoms for biomedical applications.
- **Chapter 6:** Is a manuscript entitled "Realistic deformable phantoms with optical properties of human tissues for biomedical research applications" under review in the Optica review journal. This work explored the potential of (cheap and readily available) slime materials as a primary medium for fabricating phantoms with reproducible and stable optical and mechanical properties as diseased and healthy biological tissues.
- **Chapter 7:** This chapter summarizes the contribution to present knowledge and gives suggestions for future work.

## Chapter 2

# Theory

### 2.1 Optical Properties of Light in Tissues

Light incident on a turbid media such as biological tissues with added optical agents experiences multiple processes, including reflection, refraction, absorption, and scattering [53]. These optical properties determine the total transmission at a particular wavelength, as illustrated in Figure 2.1 [53]. However, multiple scattering effects complicate the light propagation producing a wide range of paths varying with absorption and scattering. The radiative transfer theory, Monte Carlo (MC) simulation, and diffusion theory are significant in analyzing light interaction with tissues [3, 5]. The absorption coefficient describes the concentration of various chromophores. The scattering coefficient and the anisotropy factor provide information about the form, size, and concentration of different scattering components in biological tissues [53].



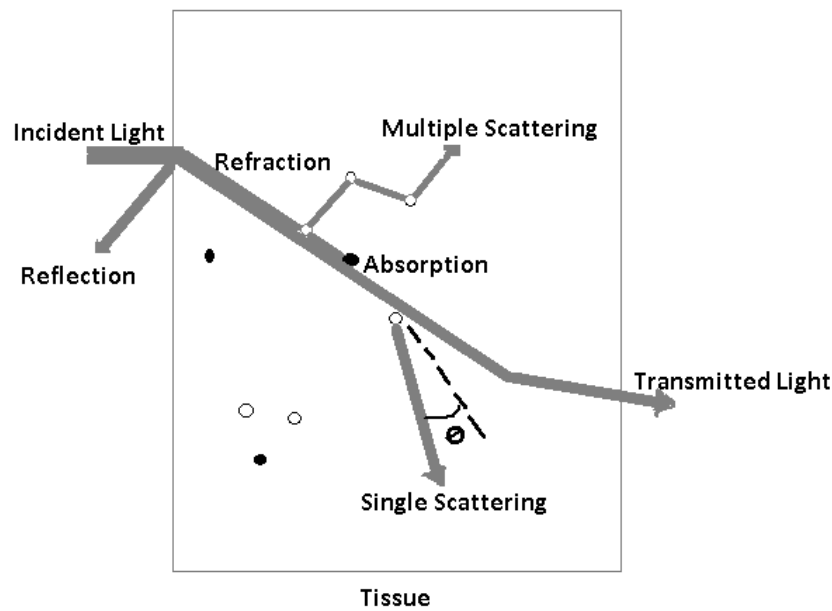


Figure 2.1: Optical Properties of Light in Biological Tissues [53].

The most common instruments used to extract the optical properties are spectrophotometers, depicted in Figure 2.2. These bulky instruments measure the fraction of light incident, transmitted, and reflected on the surface of the biological tissue. Faster and accurate readings from the spectrophotometers are with an integrating sphere diffusing the incident light into a spectrum of wavelengths [54]. Furthermore, the intensities are graphically and digitally detected using a charge-coupled detector device [54].

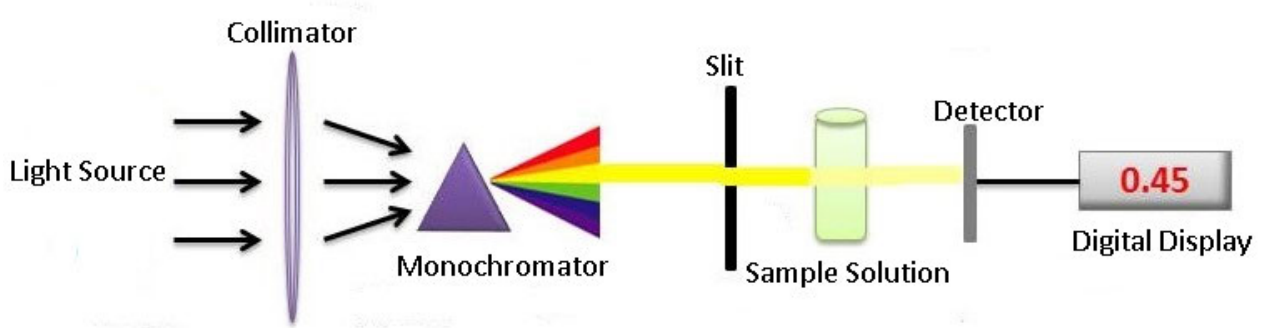
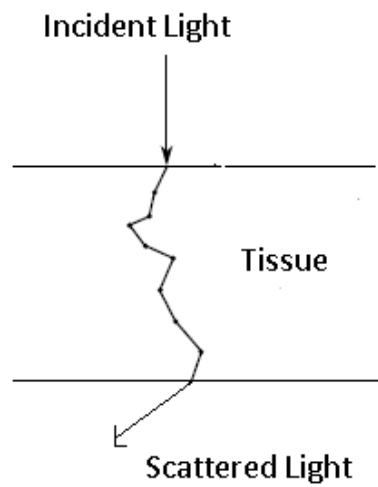


Figure 2.2: Spectrophotometer [54].

### 2.1.1 Scattering

Scattering in tissue results from random variations in the refractive index at the cellular scale, changing the direction of light propagation (Figure 2.3). The scattering depends on tissue components' size, morphology, and structure [55]. The scattering event is classified as either elastic or inelastic depending on the energy conservation. Inelastic scattering, such as Raman and Brillouin scattering, is described by a change in wavelength of the incident photon when the incident light interacts at vibrational and rotational molecular levels, resulting in a shift between these levels. This changes the power of the scattered light relative to the incoming light [56].



**Figure 2.3:** Attenuation of laser light through a scattering medium.

Elastic scattering occurs when the photons of the incident and scattered light have the same power (energy). Mie and Rayleigh scattering are two models of elastic scattering in biological tissues [56, 57].

#### Mie Theory of Light Scattering

In 1908, Gustav Mie developed the exact theory of the scattering of light by a solid sphere [58]. The internal and external scattered electromagnetic fields are defined as a function of the size parameter ( $x$ ) and the relative refractive index ( $m$ ) [59].

$$x = \frac{2\pi na}{\lambda}; m = \frac{n_1}{n}, \quad (2.1)$$

where  $n$  and  $n_1$  refer to the complex refractive indices of the medium and particle respectively and  $a$  describes the radius of the scattering particle. The solutions are based on infinite series of Bessel and modified Bessel functions; for an incident

wave-number ( $k$ ) passing in the x direction [59],

$$\mathbf{E}_i = E_0 e^{ikr \cos \theta} \hat{e}_x \quad (2.2)$$

The electric and magnetic fields of the scattered wave are defined by [59],

$$\mathbf{E}_\delta = \sum_{n=1}^{\infty} E_n (ia_n N_{eln} - b_n M_{oln}) \quad (2.3)$$

$$\mathbf{H}_\delta = \frac{k}{\omega p} \sum_{n=1}^{\infty} E_n (ib_n N_{oln} + a_n M_{eln}) \quad (2.4)$$

Where,

$$\mathbf{M}_{on} = \cos \phi \pi_n (\cos \theta) h_n^{(1)}(kr) \hat{e}_\theta - \sin \phi \tau_n (\cos \theta) h_n^{(1)}(kr) \hat{e}_\phi$$

$$\mathbf{M}_{en} = -\sin \phi \pi_n (\cos \theta) h_n^{(1)}(kr) \hat{e}_\theta - \cos \phi \tau_n (\cos \theta) h_n^{(1)}(kr) \hat{e}_\phi$$

$$\begin{aligned} \mathbf{N}_{on} = & \cos \phi n(n+1) \sin \theta \pi_n (\cos \theta) \frac{h_n^{(1)}(kr)}{kr} \hat{e}_r + \\ & \cos \phi \tau_n (\cos \theta) \frac{[kr h_n^{(1)}]' }{kr} \hat{e}_\theta - \sin \phi \pi_n (\cos \theta) \frac{[kr h_n^{(1)}]' }{kr} \hat{e}_\phi \end{aligned}$$

$$a_n = \frac{pm^2 j_n(mx) [x j_n(x)]' - p_1 j_n(x) [mx j_n(mx)]'}{pm^2 j_n(mx) [x h_n^{(1)}(x)]' - p_1 h_n^{(1)}(x) [mx j_n(mx)]'}$$

$$b_n = \frac{p_1 j_n(mx) [x j_n(x)]' - p j_n(x) [mx j_n(mx)]'}{p_1 j_n(mx) [x h_n^{(1)}(x)]' - p h_n^{(1)}(x) [mx j_n(mx)]'}$$

and

$$E_n = i^n E_0 \frac{(2n+1)}{n(n+1)}$$

$$\pi_n = \frac{P'_n}{\sin \theta}$$

$$\tau_n = \frac{dP'_n}{d\theta}$$

Where  $\theta$  and  $\phi$  describe the planar and azimuthal spherical polar angles,  $p$  and  $p_1$  describe the permeability of the medium and sphere respectively,  $h_n^{(1)}$  is a spherical Bessel function of the third kind,  $j_n$  defines a spherical Bessel function, and  $P'_n$  is a Legendre Polynomial.

The rate of energy scatter ( $W_\delta$ ) can be determined using equation 2.3 and 2.4 [59]:

$$W_\delta = \frac{1}{2} Re \int_0^{2\pi} \int_0^\pi (E_{\delta\theta} H_{\delta\phi}^* - E_{\delta\phi} H_{\delta\theta}^*) r^2 \sin \theta d\theta d\phi \quad (2.5)$$

The scattering and extinction cross-sections, ( $\sigma_s$ ) and ( $\sigma_a$ ) respectively:

$$\sigma_s = \frac{W_s}{I_0}; \sigma_a = \frac{W_a}{I_0}, \quad (2.6)$$

where  $I_0$  describes the total intensity on the particle,  $W_s$  the rate of energy scattering by the particle, and  $W_a$  the rate of energy absorption by the particle.

Using equation 2.6,  $\sigma_\delta$  can be determined.

$$\sigma_\delta = \frac{2\pi}{k^2} \sum_{n=1}^{\infty} (2n+1) Re[a_n + b_n] \quad (2.7)$$

Solutions to these equations are evaluated numerically by a computer with slight modifications in these equations for ease of calculation and convergence [59]. When the convergence speed is increasing, the particle is becoming smaller [59]. The scattering and extinction cross-sections and the angular dependence of scatter can be determined in the scattered fields. The angular scatters function for particles of size greater or equal to the wavelength is highly forward weighted [59]. Additionally, Mie's theory has been employed in other simple geometries, such as elliptical particles and hollow spheres, however, this is not strictly valid for particles of arbitrary geometry [59]. This is the only theory that applies to particles of size comparable with the wavelength [59]. When the particle size is less than  $\frac{1}{4}$  of the wavelength the theory simplifies, and Rayleigh scattering theory applies [59].

### Rayleigh Theory of Light Scattering

Rayleigh's theory analyses the scattering of light by particles much smaller than the wavelength [59]. A derivation of this theory considers the dimensions of the variables included, the volume ( $V$ ) of the particle, the distance ( $r$ ) at which observations are observed, and the wavelength ( $\lambda$ ) of the light. The scattered intensity ( $I_s$ ) is given by [59]:

$$I_s \propto \frac{V^2}{r^2 \lambda^4} \quad (2.8)$$

A similar equation can be derived from Mie's theory by taking the first few terms of the Bessel series expansion. For unpolarized incident light ( $I_i$ ), the scattered light

( $I_s$ ) at angle  $\theta$  is [59]:

$$I_s = \frac{8\pi^4 na^6}{\lambda^4 r^2} \left( \frac{m^2 - 1}{m^2 + 2} \right)^2 (1 + \cos^2 \theta) I_i \quad (2.9)$$

Thus, the angular dependence of scatter is a sinusoidally varying function, and as the particle's radius ( $a$ ) approaches zero, the distribution becomes isotropic [59].

Scattering in optically inhomogeneous media is characterized by the scattering coefficient ( $\mu_s$ ), known as the distribution probability per unit length. It describes the average times per unit length a photon changes its direction. In most biological tissues, light is scattered in the forward direction [56].

### Scattering Cross-Section and Coefficient

The effective scattering cross-section ( $\sigma_s$ ) refers to the ability of a molecule to scatter a photon of a particular wavelength. The scattering cross-section is defined as follows,

$$\sigma_s = D_s A_s, \quad (2.10)$$

Where  $D_s$  is the scattering efficiency and  $A_s$  is the geometrical cross section for scattering element.

The scattering coefficient is given as:

$$\mu_s = \rho \sigma_s, \quad (2.11)$$

Where  $\rho$  is a particle number density,  $\sigma_s$  is the scattering cross-section, and  $\mu_s$  is a quantity that measures light scattering as it passes through a tissue.

### 2.1.2 Absorption

Absorption is the attenuation of incident light as it transverses through biological tissues, Figure 2.4. The absorption process involves light transformation to other energy(power) states such as heat, sound, and fluorescence as the light passes through the tissue [55]. The molecular electronic, vibrational, or rotational states become excited by the energy transmitted by the incident photon leading to partial energy conversion. Conversely, there is no conversion of light energy without absorption. The intensity of absorption in tissue directly depends on the wavelength of radiation, the concentration of absorbing agents, and the thickness of the absorbing layer [57]. Among these, the incident wavelength mainly determines the absorption coefficient.

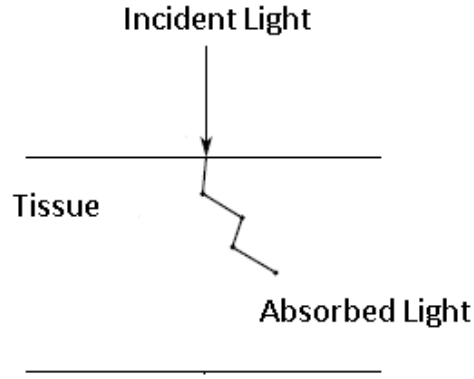


**Figure 2.4:** Light absorption in a phantom tissue.

The absorbance ( $A$ ) of the tissue is described by the ratio of absorbed and incident intensities [60]:

$$A = \frac{I_A}{I_0} \quad (2.12)$$

#### **Absorption Cross-Section and Coefficient**

The ability of a molecule to absorb a photon of a particular wavelength is the absorption cross-section ( $\sigma_a$ ). It is a term used to specify the absorption properties of a single molecule [60]. Absorption cross-section can be expressed as,

$$\sigma_a = D_a A_a, \quad (2.13)$$

Where  $D_a$  is the absorbing effectiveness and  $A_a$  is the absorbing element geometric cross section.

The absorption coefficient is used to measure the amount of light attenuated in tissue, which is defined as:

$$\mu_a = \rho \sigma_a, \quad (2.14)$$

Where  $\rho$  is the density of particles,  $\sigma_a$  is the cross-section of absorption and  $\mu_a$  is the absorption coefficient of light attenuation as it moves through the tissue.

### 2.1.3 Transmission of Laser Light

Light transmission refers to the tendency of light to pass through an object (Figure 2.5). The phenomenon has been extensively measured for various biological tissues as a function of the sample thickness and the incident light wavelength [61, 62]. Tanikawa et al. [63] utilized optical tomography to image optical properties distribution in human bodies by measuring transmitted light at skin surfaces. Guiselini et al. (2016) [64] gathered information on the effective transmission of red (660 nm) and infrared (780 nm) low-intensity lasers through the anterior, middle, and posterior regions of human maxillary and mandibular alveolar bone. They aim to determine more efficient parameters for low-intensity laser therapy (LILT) in postoperative oral surgery involving bone tissue. Light transmission was explored and determined through albino skin using a 1440 nm near-infrared laser diode by Abdussamad [65]. Findings demonstrated that this method could lead to a non-invasive approach to enhancing wound healing. In 2000, Young et al. [66] studied the behaviour of NIR light transmission models in the adult human head. They determined the relative effects of the extracerebral tissue layers on the passage of NIR photons.

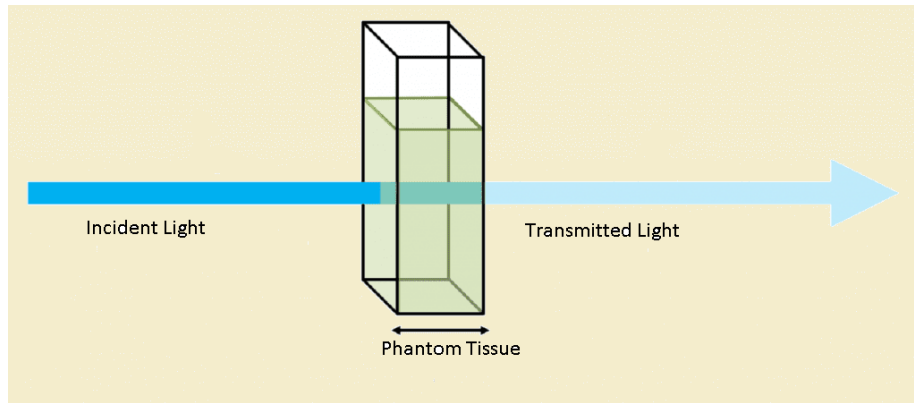


**Figure 2.5:** Transmission of light through tissue [61, 62].

The transmittance ( $T$ ) is described as the ratio of transmitted intensity  $I_T$  to the incident intensity  $I_0$  of the medium [62]:

$$T = \frac{I_T}{I_0} \quad (2.15)$$

The transmission can also be expressed as :

$$T = \exp(-\sigma_a N_a l) = \exp(-\mu_a l), \quad (2.16)$$

where  $\sigma_a$  is the efficient absorption cross-section ( $\text{cm}^2$ ),  $N_a$  is the absorbing molecular density ( $\text{cm}^3$ ),  $l$  is the optical path (cm) and  $\rho$  is the optical density ( $OD$ ) or

extinction. Lastly, this optical property helps to identify the optimal light intensities in medical applications.

## 2.2 Light Distribution in Tissue

The behaviour of a laser beam through biological tissue in a solid or liquid state depends on tissue properties such as:

### 2.2.1 Total and Effective Attenuation Coefficient

The attenuation is the reduction of light energy as it passes through the biological tissues [67]. It is regarded as the rate of energy loss per unit penetration length due to the absorption and scattering of photons.

The total attenuation coefficient ( $\mu_t$ ) describes the propagation of laser light inside a biological tissue as the sum of the scattering and absorption coefficients [68]:

$$\mu_t = \mu_s + \mu_a \quad (2.17)$$

The exponential attenuation of laser light in the biological tissue is predominantly described by the effective attenuation coefficient ( $\mu_{eff}$ ) [68]:

$$\mu_{eff} = [(3\mu_a(\mu_a + \mu'_s))^{\frac{1}{2}}], \quad (2.18)$$

Where  $\mu'_s$  is the reduced scattering coefficient.

### 2.2.2 Reduced Scattering Coefficient

The reduced scattering coefficient ( $\mu'_s$ ) is the function of scattering coefficient ( $\mu_s$ ) and anisotropy factor ( $g$ ), as shown in the following equation:

$$\mu'_s = \mu_s(1 - g) \quad (2.19)$$

This parameter is mostly used to describe media, such as biological tissue that are strongly forward scattering and  $g \approx 0.9$ .

### 2.2.3 Anisotropy Factor ( $g$ )

A measure of the degree of forward scattering in biological tissues is determined by the anisotropy factor ( $g$ ). When a particle scatters a photon, its trajectory is deflected by scattering angle ( $\theta$ ), and the component of the new path aligned in the



forward direction is  $\cos(\theta)$  [55]. The anisotropy factor ( $g$ ) is the average cosine of the scattering angle [69]:

$$g = \langle \cos(\theta) \rangle, \quad (2.20)$$

$$g = \frac{\int_{4\pi} p(\theta) \cos\theta dw}{\int_{4\pi} p(\theta) dw}, \quad (2.21)$$

Where  $p(\theta)$  is the phase function and  $dw$  is the elementary solid angle, expressed as:

$$dw = \sin\theta d\theta d\phi \quad (2.22)$$

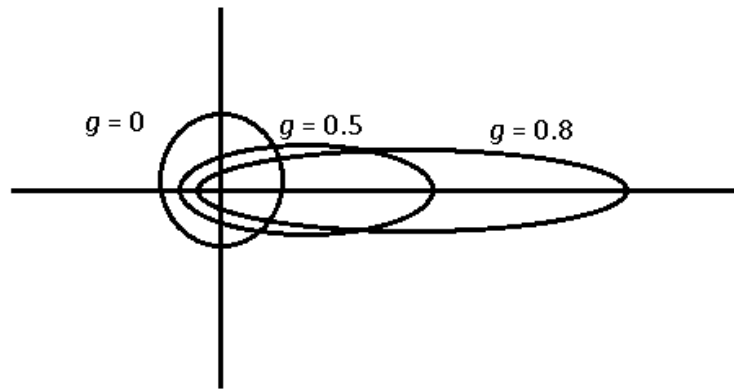


Figure 2.6: Different values of the anisotropy factor.

#### 2.2.4 Transport Mean Free Path

Transport mean free path ( $l^*$ ) is the distance light radiation needs to travel before losing its original direction of propagation relative to the anisotropy factor ( $g$ ) and reduced scattering coefficient ( $\mu'_s$ ):

$$l^* = \frac{1}{\mu'_s} = \frac{1}{(1 - g)\mu_s} \quad (2.23)$$

#### 2.2.5 Penetration Depth

The laser beam's penetration depth ( $\delta$ ) in biological tissue is the most critical parameter that indicates light transmittance through the tissue and its suitability for surgical procedures. It is also known as the mean free path length ( $MFP$ ), the mean distance a laser beam travels through the absorption or scattering events as the total fluence rate ( $Wmm^{-2}$ ) drops to  $e^{-1}$  (Figure 2.7) [70].

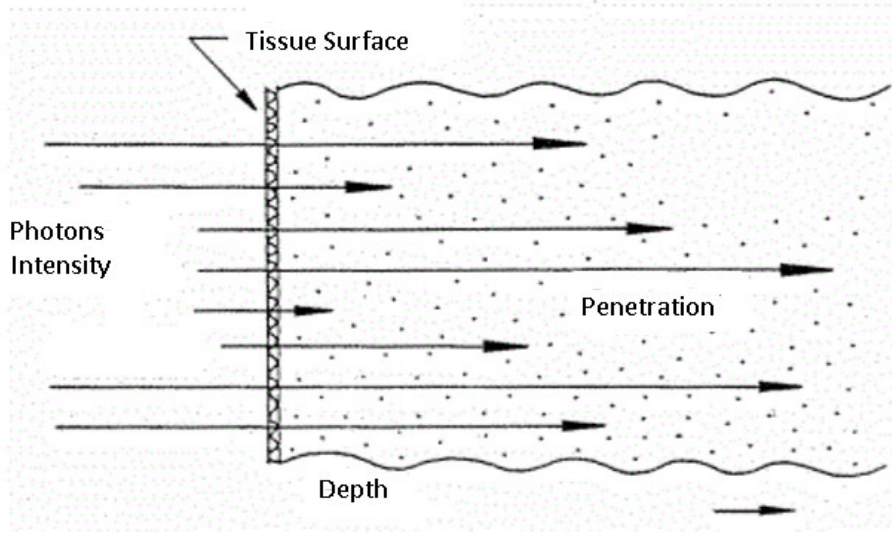


**Figure 2.7:** Schematic representation of a photon penetration depth inside a tissue.

The reciprocal of the effective transport coefficient is arbitrarily equal to the optical penetration depth:

$$\delta = \frac{1}{\mu_{eff}} \quad (2.24)$$

The penetration depth increases with the laser radiation wavelength [71].

### 2.2.6 Optical Albedo

This parameter is essential for predicting light propagation in tissue for single scattering [55]. The optical albedo ( $a$ ) is described as the ratio of the scattering coefficient ( $\mu_s$ ) to the transport coefficient ( $\mu_t$ ).

$$a = \frac{\mu_s}{\mu_t}, \quad (2.25)$$

Where  $a = 0$  for a completely absorbing medium and  $a = 1$  for a completely scattering medium [55].

## 2.3 Scattering Particles

Scattering particles with rough surface in biological tissues and cells are typically assumed to be homogeneous spherical, internally symmetric, and does not interact with each other [72]. Optical scattering originates from the interaction of electromagnetic radiation and biological tissue particles, leading to light diffusion in biological tissue [72]. This interaction is vital in various processes, such as cell biology and heat transfer. The classical electromagnetic theory is used to explain and understand light

scattering particles [73].

In most optical tissue phantoms, the choice of a scattering agent is based on the volume fraction, shape, and concentration of the scattering particles, differentiating it from other matrix compositions. Three main choices of scattering agents are identified: polymer microparticles, lipid microparticles, and white metal oxide powders [69]. Lipid microparticles act as biological scattering agents such as cells' organelles and bilipid membranes found in actual tissues. Another common choice is the polymer microsphere made in several forms of sizes and shapes with good quality to control the refraction index [69]. The third choice is white metal oxide powders, such as aluminum oxide and titanium dioxide powder, otherwise regarded as the pigment in white plastic and paint. They provide high scattering coefficients found in well-controlled spherical formulations where exceptional high scatter and low absorption are highly demanded. The main disadvantage of these powders is that they reside in suspension in most media and require continuous stirring for even distribution [69].

### 2.3.1 Single and Multiple Scattering

Studying biological cells and organelles requires an extensive understanding of light-waves scattered by particles, which is by the single and multiple scattering model. Single scattering occurs when the incident light wave undertakes a single collision with particles of the medium it propagates [74]. It is observed in healthy transparent animals and the human eye tissues, such as the eye lens, cornea, and vitreous body [74].

Single-particle scattering is also due to the collection of the dipoles emitting an oscillating electrical field [74]. Scattering by such a coherence array is by the scattering shape and size, polarization state, and incident radiation frequency. The total energy of the incident light wave scattered is a function of the cross-section of the scattering particle ( $\sigma_s$ ). In contrast, the total energy absorbed is a function of the absorption cross-section ( $\sigma_a$ ). The sum of these cross-sections is the extinction cross-section, expressed as [62]:

$$\sigma_{ext} = \sigma_s + \sigma_a \quad (2.26)$$

The extinction cross-section is by the accurate measurements of the radiation transmitted via a plate of  $N$  equivalent scattering particles per unit volume. The incident light wave ( $I_i$ ) and the transmitted light wave ( $I_t$ ) are associated with the following

equation assuming multiple scattering is significantly small [62].

$$I(h) = I_0 e^{N\sigma_{ext}L}, \quad (2.27)$$

Where  $L$  is the thickness of the slab provided that multiple scattering is negligible.  $N\sigma_{ext}$  is replaced by the generalized from Equation 2.25 for similar particles to account for differences between particles.

$$\sum_j N_j \sigma_{ext}, \quad (2.28)$$

Where  $j$  denotes all parameters differentiating one particle from another.

The single-scattering events control the angular scattering in biological tissues approximated by the Henyey-Greenstein scattering function:

$$P(\theta) = \frac{1}{4\pi} \frac{1 - g^2}{(1 + g^2 \cos(\theta))^{\frac{3}{2}}}, \quad (2.29)$$

$P(\theta)$  describes the phase function,  $\theta$  is the scattering angle and  $g$  is the anisotropic factor.

In contrast, in most in-vivo tissues such as skin, brain, and breast, an incident photon undertakes many scattering events (multiple scattering) [74]. The mean free path ( $MFP$ ) describes the scattering regime [74]. The Mean free path length, defined as the mean distance between two successive interactions with scattering or absorption experienced by a photon traveling in a scattering-absorption medium, is expressed as [74]:

$$MFP = I_{ph} = \frac{1}{\mu_t} \quad (2.30)$$

The radiation transfer theory (RTT) is the basic theory used to approximate light distributions in multiple scattering media with absorption as tissue [74]. The approach, also known as the linear transport equation, introduces a balanced equation describing the flow of particles, such as photons in a specific elemental volume, by considering its velocity, location, and changes due to scattering [74].

The integral equation also allows the calculation of the fluctuating field in the multiple scattering processes. This fluctuating field is an integral of the average field ( $\langle E_j \rangle$ ) at the location of some arbitrary particles ( $j$ ), as shown in the following equation:

$$\langle E_j \rangle = E^0 + \int S_j \langle E_j \rangle G(\mathbf{r}_j) d\mathbf{r}_j \quad (2.31)$$

This technique only works well in biological tissues with a significantly small fractional scatterers volume [73].

## 2.4 Scattering Function at Small Scattering Angles

Scattering function  $P(\theta)$  describes the probability for a photon scattered per unit solid of an angle ( $\theta$ ) from the direction of propagation [75]. This function is determined using goniometric measurements, and the small angle refers to the slight deflection of light ( $0.1^\circ - 10^\circ$ ). The light scattered at small angles is accurately captured by the photometer. With significantly small phantom tissue's optical thickness, multiple scattering effects are negligible, and the measured energy (power) is closely related to the scattering function [75]. The single-scattering condition also requires the reduction of the microspheres concentration in the tissue sample as per below:

$$\frac{1}{\mu_{s,d}} \gg L, \quad (2.32)$$

Where  $L$  describes the slice thickness length and subscript  $d$  in the scattering coefficient refers to the spheres dilution in phantom. Furthermore, placing the tissue sample in a saline solution [76] or between pair of semi-cylinders glass [77] helps determine the difference between the refractive index and the external medium during goniometer measurements.

The main disadvantage of goniometric measurements is difficulty distinguishing the scattered light from unscattered components when measurements are from small scattering angles. Goniometric measurements of scattering function are applicable only for angles larger than  $\approx 2$  degrees [75]. Considerably smaller angles are generally measured using an extrapolation procedure [78].

Biological tissues scattered approximately 50% of the energy emitted through a narrow forward lobe, enabling the measurements at small scattering angles with information comparable to that obtained from the remaining angular range. However, this shifts everything to the scattering function at small scattering angles. The scattering function  $P(\theta)$  value is extracted from the repeated transmissometric measurements by employing various values for the receiver's angular field of view ( $\alpha$ ). Applying a light beam with a bit of divergence and performing measurements in the single scattering method, the mean value  $P_{i,j}$  of the scattering function in the angular range  $[\alpha_i, \alpha_j]$  is defined as [79]:

$$P_{ij} = \frac{1}{2\pi \left( \cos \frac{\alpha_i}{n} - \cos \frac{\alpha_j}{n} \right)} \frac{P(\alpha_j) - P(\alpha_i)}{a\eta I_T}, \quad (2.33)$$

where  $a = \frac{\mu_s}{\mu_t}$  describes the single scattering albedo,  $I_T$  defines the transmitted light,  $n$  is the refractive index and  $\eta$  is the optical thickness factor, expressed as:

$$\eta = \ln \frac{I_T}{I_0} \quad (2.34)$$

## 2.5 Light Propagation Models in Tissues

The mathematical models heavily rely on the absorption coefficient ( $\mu_a$ ) and scattering coefficient ( $\mu_s$ ) to describe the light propagation inside the biological tissue.

### 2.5.1 The Radiative Transfer Equation

The transfer of laser light energy (power) in biological tissue is described by the Transport theory [80], analyzing the light energy movement in a small volume element of the biological tissue, as shown in Figure 2.8 [81]. Transport theory used the superposition of an electromagnetic field to eliminate unwanted wave properties of light, such as polarization and interference [80].

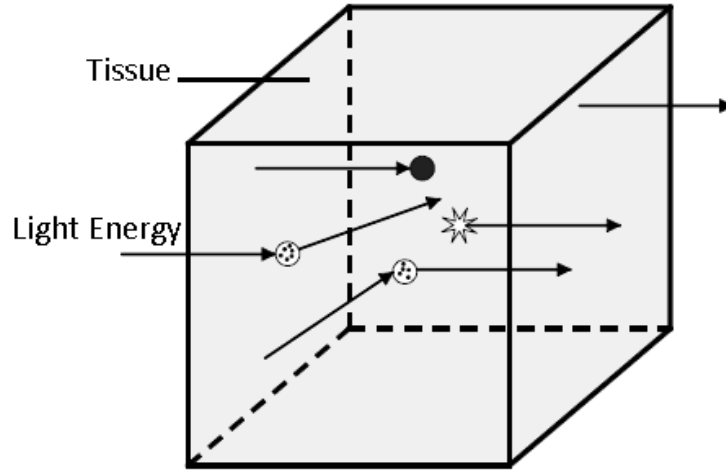


Figure 2.8: The light energy flow inside the tissue [81].

The radiative transfer equation (RTE) is the mathematical model that describes light migration in biological tissue, expressed as [82]:

$$\frac{\partial L(\vec{r}, \hat{\Omega})}{\partial t} + \hat{\Omega} \cdot \nabla L(\vec{r}, \hat{\Omega}, t) = -(\mu_a + \mu_s)L(\vec{r}, \hat{\Omega}, t) + \mu_s \int_{4\pi} p(\hat{\Omega}, \hat{\Omega}') L(\vec{r}, \hat{\Omega}', t) d\hat{\Omega}' + s(\vec{r}, \hat{\Omega}, t), \quad (2.35)$$

describing the change of energy radiance  $L(\vec{r}, \hat{\Omega}, t)$  at position  $\vec{r}$  in direction  $\hat{\Omega}$  due to losses by absorption and scattering.

Where  $\mu_a$  represents the absorption coefficient,  $\mu_s$  is the scattering coefficient,  $s(\vec{r}, \hat{\Omega}, t)$  is the phase function, and  $S(\vec{r}, \hat{\Omega}, t)$  is the radiation source.

The Radiative Transfer Equation (RTE) considers the radiant energy balance in an arbitrary tissue volume. It is a balance equation relating the change in energy radiance to the shift in energy flow, loss due to absorption and scattering, and gains due to scattering and radiation sources. The exact solution of the RTE exists only in the isotropic distribution of simple geometrics. Therefore, a further approximation is required [82].

### 2.5.2 Diffusion Equation Formalism

The radiation transport equation models the photon propagated through biological tissues with some approximations. The diffusion approximation is preferred to solve the radiative transfer equation by expanding  $L(\vec{r}, \Omega, t)$  in terms of spherical harmonics  $Y_{n,m}$ , considering only the first two terms [83].

$$L(\vec{r}, \hat{s}, t) = \sum_{n=0}^1 \sum_{m=-n}^n L_{n,m}(\vec{r}, t) Y_{n,m}(\hat{s}) \quad (2.36)$$

Multiplying equation 2.35 by  $(\hat{s})$  and substituting it into the current density equation 2.36:

$$J(\vec{r}, t) = \int_{4\pi} \hat{s} L(\vec{r}, \hat{s}, t) d\Omega \quad (2.37)$$

we get:

$$L(\vec{r}, \hat{\Omega}, t) \approx \frac{1}{4\pi} \Phi(r, t) + \frac{3}{4\pi} \vec{j}(\vec{r}, t) \cdot \vec{\Omega} \quad (2.38)$$

Substituting equation 2.37 into the radiative transport equation, multiplying both sides by  $s$ , and integrating over the full  $4\pi$ , assuming the fractional change in  $j(\vec{r}, t)$  is small.

$$\frac{\partial j(\vec{\Omega}, t)}{\partial t} \ll v(\mu_a + \mu'_s) = v\mu'_t \quad (2.39)$$

We obtain[27],

$$\frac{1}{v} \frac{\partial \Phi(r, t)}{\partial t} = \nabla \cdot D \nabla \Phi(\vec{r}, t) - \mu_a \Phi(\vec{r}, t) + S(\vec{r}, t), \quad (2.40)$$

Where  $v$  is the speed of light in the medium,  $\Phi(\vec{r}, t)$  is the fluence rate,  $D = (\frac{1}{3})(\mu_a +$

$\mu'_s$ ) is diffusion constant and  $\mu'_s$  is the reduced scattering coefficient.

The diffusion theory can modulate light transport faster, but it is not useful when absorption is stronger than scattering ( $\mu_a \gg \mu_s$ ). This leads to the employment of other models such as Monte Carlo Simulation [83].

### 2.5.3 Kubelka-Munt (KM) Theory

The Kubelka-Munt model theoretically describes uniform and diffuse irradiance propagation in turbid media and provides a clear analytical solution. A diffusion model is equivalent to this model with a forward and backward peaked phase function [84]. Furthermore, the KM technique is well known as a good approximation of the general radiative transport equation in one-dimensional (1D) theoretical investigations. However, the KM model does not provide an exact solution for highly absorbing and weakly-scattering media [85]. In principle, the KM model is a two-flux model having two fluxes ( $F_+(x)$  and  $F_-(x)$ ) of light passing through the medium in forward and reverse directions [85]. The differential equations of this model are [85]:

$$\frac{dF_+(x)}{dx} = (K + S)F_+(x) + SF_-(x) \quad (2.41)$$

$$\frac{dF_-(x)}{dx} = (K + S)F_-(x) - SF_+(x) \quad (2.42)$$

These equations describe the radiant energy balance on  $dx$  of the medium. Where the optical properties of the medium are defined by the scattering ( $S$ ) and absorption ( $K$ ) coefficients.

Equation 2.41 and 2.42 have exact analytical solutions [85]:

$$F_+(x) = C_1 e^{-\alpha x} + C_2 e^{\alpha x} \quad (2.43)$$

$$F_-(x) = C_1 A_- e^{-\alpha x} + C_2 A_+ e^{\alpha x} \quad (2.44)$$

Where,

$$\alpha = \sqrt{K(K + 2S)} \quad (2.45)$$

$$A_+ = \frac{(K + 2S + \alpha)}{(K + 2S - \alpha)} \quad (2.46)$$

$$A_- = \frac{1}{A_+} \quad (2.47)$$

It is important to determine a backscattered  $F_{bs} = F_-(0)$  and a transmitted radiation by a tissue flux  $F_T = F_+(H_0)$  in biomedical non-invasive applications. This



calculation further includes determination of optical properties of biological tissue in transport coefficients  $S$  and  $K$  for correct medical diagnosis purposes. The calculations yield as [85]:

$$F_{bs} = F_-(0) = F_0.R.e^{-\mu_a h} + F_-^{i=1}(0).(1-R).e^{-\mu_a h/2} \quad (2.48)$$

$$F_T = F_+^{i=N}(h).(1-R).e^{-\mu_a h/2} \quad (2.49)$$

Using the KM approach, the general illustration of the differential equations from Equations 2.41 and 2.42 is [85]:

$$\frac{dF_+(x)}{dx} = -\beta_1 F_+(x) + \beta_2 F_-(x) \quad (2.50)$$

$$\frac{dF_-(x)}{dx} = \beta_1 F_-(x) - \beta_2 F_+(x) \quad (2.51)$$

Equations 2.50 and 2.51 have standard solutions for backscattered and transmitted radiation [86],

$$F_{bs} = F.P.\frac{1 - e^{-2LH_0}}{1 - P^2 e^{-2LH_0}} \quad (2.52)$$

$$F_T = F_0.e^{-LH_0}.\frac{1 - P^2}{1 - P^2 e^{-2LH_0}} \quad (2.53)$$

Where  $H_0$  represents the thickness of medium,  $L = \sqrt{\beta_1^2 - \beta_2^2}$  and  $P = (\beta_1 - L)/\beta_2$

The transport density of heterogeneities [85]:

$$\mu_\rho = \frac{N}{H_0} \quad (2.54)$$

The simplest form of the external boundary conditions:

$$F_+(0) = F_0; F_-(H_0) = 0$$

Finally, the general dependencies expressed as [85]:

$$\beta_1 = \omega.\frac{\mu_a - \mu_\rho \ln(1-R) + \mu_\rho \ln\left(1 - \omega + \sqrt{\omega^2 - R^2 e^{-2\mu_a/\mu_\rho}}\right)}{\sqrt{\omega^2 - R^2 e^{-2\mu_a/\mu_\rho}}} \quad (2.55)$$

$$\beta_1 = R^2 e^{-2\mu_a/\mu_\rho}.\frac{\mu_a - \mu_\rho \ln(1-R) + \mu_\rho \ln\left(1 - \omega + \sqrt{\omega^2 - R^2 e^{-2\mu_a/\mu_\rho}}\right)}{\sqrt{\omega^2 - R^2 e^{-2\mu_a/\mu_\rho}}} \quad (2.56)$$

Where:

$$\omega = \frac{1 - (1 - 2R).e^{-2\mu_a/\mu_p}}{2} \quad (2.57)$$

#### 2.5.4 Monte Carlo

Monte Carlo Method is widely used in biomedical tissue optics to solve RTE even in the complexity of biological tissues such as blood. This method employs the probability distribution model, where a laser beam incident on a tissue determines the probability of the scattered or absorbed photon per unit length [87]. These probability models are used to generate the random sampling of photon trajectories.

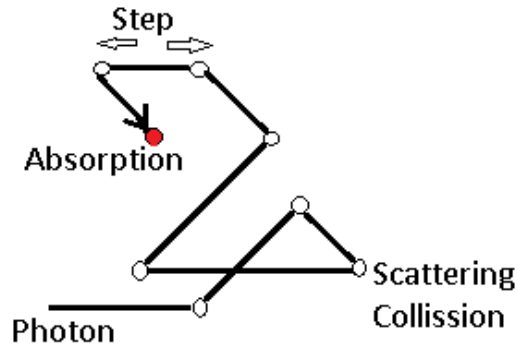


**Figure 2.9:** Random movements of the photon in biological tissue [87].

The simple Monte Carlo algorithm for photon propagation is to propagate a photon at a specific source position in a certain direction [87]. The photon is either scattered or absorbed, depending on the optical properties of media at that specific site. This approach is very inefficient and was improved by using different variance reduction techniques. These techniques reduce the number of photons needed to achieve the desired accuracy for a Monte Carlo determination and are mostly applied in the following procedure [87].

The approach propagates many photons (packet) simultaneously along each path. Typically only one photon follows each pathway, and at each step, the photon may either be absorbed or scattered. When a packet with a specific weight ( $W$ ) of photons followed each pathway, a part of the packet would be absorbed and the remainder scattered at each step. Where weight ( $W$ ) describes the size of the packet, which initial starts from the unity [87].

The application of various step-size of the photon has been described as an effective and efficient method, where each photon is propagated with small different incremental step-sizes [87]. The probability density function for the step-size is aligned

with the Beer-Lambert law. The probability ( $P$ ) is sampled as:

$$P = e^{-\mu_t \Delta s} \quad (2.58)$$

$$\Delta s = \frac{-\ln \xi}{\mu_t}, \quad (2.59)$$

Where step-size  $\Delta s$  (Equation 2.59) is for a random variable function ( $\xi$ ) equidistributed between  $[0,1]$  and describes the photon's distance before interaction with biological tissue (unattenuated photon) [88].

The photon packet is split into two portions for every step size, and each portion either gets absorbed or scattered. The amount of photon packet scattered is given by [89]:

$$W' = W \times \frac{\mu_s}{\mu_t}, \quad (2.60)$$

Where  $W'$  describes the weight of the scattered photon after each interaction and  $W$  is the original weight before interaction, as shown in Figure 2.10. The direction of the scattered photon is computed by the scattering function known as the Henyey-Greenstein phase function, where the deflection angle ( $\theta$ ) is specified as [89]:

$$\cos(\theta) = \frac{1}{2g} \left[ 1 + g^2 - \left( \frac{1 - g^2}{1 - g + 2g\xi} \right)^2 \right], \quad (2.61)$$

Where  $g$  represents the anisotropic factor and  $\Psi$  is the azimuthal angle distributed between  $[0, 2\pi]$  and is defined as [89]:

$$\Psi = 2\pi\xi \quad (2.62)$$

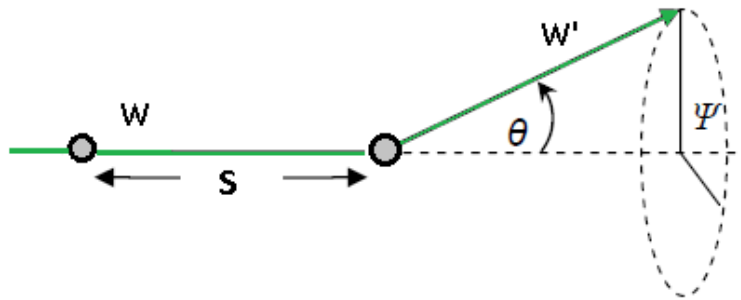


**Figure 2.10:** Stochastic parameters controlling the incident photon movement

However, Fresnel's equation determines the internal reflection after the photon packet interaction with the tissue surface [89].

### 2.5.5 Beer-Lambert Law

The Beer-Lambert Law describes the relationship between the transmitted light power ( $P$ ) through an absorbing sample (biological tissue), and the absorption concentration through the absorbing species as a monochromatic light of initial power ( $P_0$ ) travels through the model thickness ( $L$ ), as shown in Figure 2.11 [90].

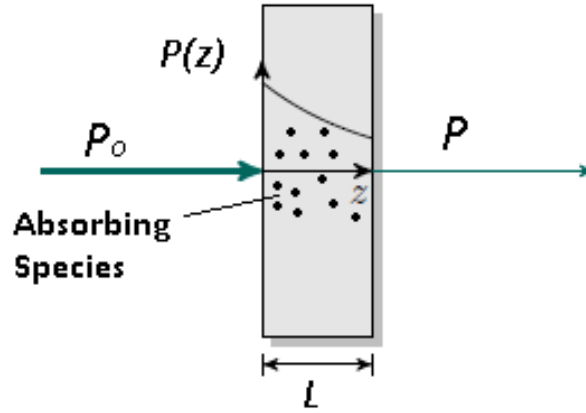


Figure 2.11: The Beer-Lambert Law [90].

Furthermore, the Beer-Lambert Law defines the attenuation of light exponentially as it passes through the tissue:

$$P = P_0 e^{(-\mu_t L)}, \quad (2.63)$$

$$P = P_0 e^{(-kcL)}, \quad (2.64)$$

Where  $c$  is the concentration of optical agents,  $k$  is the factor controlled by internal parameters, and  $\mu_t$  is the total attenuation coefficient, which is defined as [90]:

$$\mu_t = \mu_a + \mu_s, \quad (2.65)$$

Where  $\mu_a$  is the absorption coefficient and  $\mu_s$  is the scattering coefficient.

Applying logarithms in equation 2.63, Beer-Lambert Law is also expressed as:

$$\mu_t = -\frac{1}{L} \ln\left[\frac{P}{P_0}\right] \quad (2.66)$$

## 2.6 Laser Light Properties

Laser light is the optical source of the energy produced by raising the atom in the ground state ( $e_1$ ) to an excited state ( $e_2$ ) and allowed to interact with a photon with

energy ( $e_2 - e_1$ ). The atom drops from energy  $e_2$  to  $e_1$ , as shown in Figure 2.12. This movement generates another photon in phase and propagates in the same direction as the excitation photon (stimulated emission) [91].

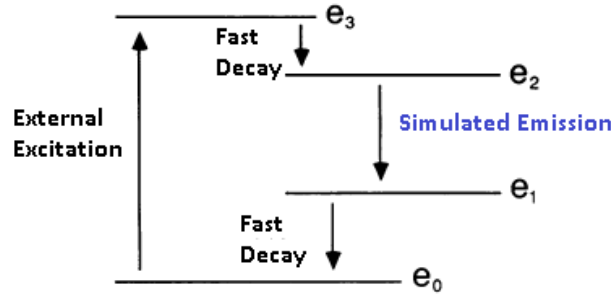


Figure 2.12: Diagram of the four-level energy [91].

Laser light has three fundamental properties used extensively in the biomedical field. The light is monochromatic with intense color in contrast to natural light, combining various wavelengths and breaking into a spectrum when passing through a prism. The energy illustrated in Figure 2.12 determines the laser's characteristic color through the relation Eq 2.67 [91].

$$E = \frac{hc}{\lambda}, \quad (2.67)$$

Where  $h$  is Planck's constant,  $c$  is the speed of light, and  $\lambda$  is the wavelength. Visible wavelengths in lasers are characterized by color, the He-Ne laser beam is red or green and the argon laser beam is blue or blue-green.

Another primary property of lasers is that, unlike other sources (sun, light bulb, or candle), they emit light in a specific direction from the source. Furthermore, collimation and low divergence of the laser lights increase their intensities, resulting in sufficient damage to targeted tissues. Hence, utmost care is highly demanded when working with higher-power lasers (20-watt, 30-watt, and 40-watt). Laser lights are coherent, in phase in both space and time. There are two types: spatial and temporal coherence. Spatial coherence is when the waves' crests and troughs coincide along lines perpendicular to the rays, and temporal coherence occurs with constant frequency, wavelength, and travel speed. Light interference patterns form bright and dark bands when the rays travel slightly different paths.

## 2.7 Characteristics and Properties of Biological Tissue

### 2.7.1 Skin Tissue

A collection of cells holding a similar structure is known as biological tissues, while a collection of these tissues are called organs. The largest organ of the human or animal body in terms of volume and surface is the skin, consisting of approximately 20% of the total body weight [92]. It performs several vital functions, such as protection from external physical, chemical, and biological assailants, aiding thermoregulation and water binding [92]. The skin structure is a complex, multilayered, continuous, and inhomogeneous tissue, with mucous membranes lining the body's surface [93]. The skin is composed of the following layers:

#### Epidermis

The epidermis is the outermost layer of the skin with an average thickness of 0.2 mm. It is protective from the environment and represents the various stages of cell differentiation [94]. The main layers are the stratum corneum (outermost layer), granular cell layer, prickle cell layer, and basal cell layer [94]. These layers sustain the organism and perform diverse functions to repel water, act as a barrier against bacterial and viral intrusion, and protect internal organs such as muscles, nerves, blood vessels, and others from external injuries. Anatomically, melanocytes, the special cells in the epidermis, produce the pigment melanin that provides the skin's colour [94]. The melanin acts as an absorber in the visible and near-infrared wavelength regions. Further, it reduces the fluence rate of light penetrating through the epidermis to a treatment site.

#### Dermis

The dermis comprises the sebaceous, blood vessels and nerves, sweat glands, and hair follicles [94]. The blood cells in dermis tissue contain three types of chromophores: bilirubin,  $\beta$ -carotene, and hemoglobin, which give the blood its red color [94]. Furthermore, the absorption of NIR light in the dermis tissue depends on the concentration of tissue chromophores conventionally given as [95]:

$$\Delta A = L \times \mu_a, \quad (2.68)$$

Where  $\Delta A$  is the amount of light attenuation,  $L$  describes the differential photon pathlength through tissue, and  $\mu_a$  is the absorption coefficient of chromophore  $X$ , defined as [95]:

$$X = [X] \times \varepsilon, \quad (2.69)$$

Where  $[X]$  describes the tissue concentration of chromophores  $X$ , and  $\varepsilon$  is the extinction coefficient of the chromophore. The blood flow is assumed to be uniformly distributed in the dermis layer during the determination of the chromophore (hemoglobin) concentration on light propagation [72].

### Hypodermis

The hypodermis is the subcutaneous layer lying under the dermis and consists of cells known as fat, connective tissues, blood, vessels, larger nerves, and macrophages [96, 97]. It provides the main structural support for the skin, insulating the body from cold and helping shock absorption [96, 97]. Three main functions of hypodermis are protection, thermoregulation, and sensation with thickness ranging from 1-6mm [96, 97].

The hypodermis is the subcutaneous layer lying under the dermis and consists of cells known as fat, connective tissues, blood vessels, large nerves, and macrophages [96, 97]. It provides structural support for the skin, insulating the body from cold and helping shock absorption [96, 97]. The three primary functions of hypodermis are protection, thermoregulation, and sensation, with thickness ranging from 1 to 6mm [96, 97].

The layers of the skin are presented schematically in Fig 2.13, below.

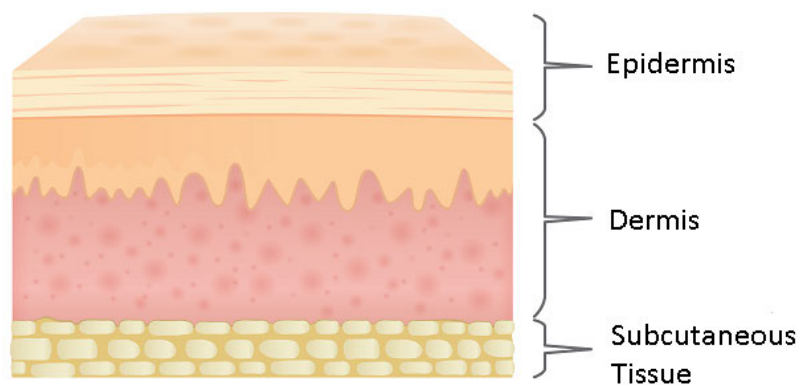


**Figure 2.13:** Layers of the skin [92].

### 2.7.2 Brain Tissue

The brain anatomical structure is immensely complex and responsible for various nervous functional systems. The human brain tissue is composed by gray matter

that constituting the brain (cerebral) cortex and the white matter which consists primarily of the myelinated nerve cell projections (axons), binding the gray matter regions of the brain to each other [98]. The cerebral cortex refers to the primary site of cognition in the brain and is divided into numerous functional areas such as memory, reasoning, senses and language.

The gray matter is formed by neuronal cell bodies or soma. It's considered to be nearly isotropic due to large differences in directional properties [98]. Conversely, the white matter tissue made up oriented nerve fibers is considered anisotropic and stiffer than gray matter [98, 99].

### 2.7.3 Malignant Brain Tumor

A brain tumor is a growth of abnormal cells in any part of the brain or skull such as its protective lining, skull base, brainstem, sinuses, and nasal cavity [100]. A malignant brain tumor refers to a cancerous and aggressive form of primary brain tumor also known as a high-grade tumor (grade 3 or 4) and it's likely to grow back after treatment [100].

Neurologists use tissue models for analysis and brain tumor diagnoses in surgery and treatment planning. Furthermore, these models help to determine the tumor grade and examine the tumorous tissue for any biomarkers to aid in the treatment approach. The main goal is to remove the cancer cells without damaging healthy areas of the brain [100].

### 2.7.4 Lung Carcinoma

Lung carcinoma is a type of cancer that begins in the lung tissues [101]. The lungs are two spongy organs in the chest that take in oxygen for inhaling and release carbon dioxide for exhaling. As lung carcinoma cells keep growing and multiplying, they form solid masses called tumors [101]. The cancer cells can break away from tumors and travel to other areas of the body and bloodstream (metastasize) [101]. The spread of lung carcinoma can be classified into three categories [101]:

- Carcinoma in situ: cancer cells have not spread.
- Invasive carcinoma: cancer cells have spread to surrounding tissue close to where it formed.
- Metastatic carcinoma: cancer cells have spread to other regions of the body or bloodstream.



Lung carcinoma treatment depends on the overall health and stage of the tumor. Optical imaging including ultrasounds, MRIs, and CT scans among others, assists to detect lung carcinoma early and visualize the cells spread [101].

### **2.7.5 Post-menopausal Uterus**

The uterus is an inverted pear-shaped muscular organ of the female reproductive system, located between the bladder and the rectum. The function of the uterus is to nourish and house a fertilized egg until the fetus is ready to be delivered [102]. The uterus consists of four major regions including the fundus, body (the main part of the uterus), isthmus, and cervix [102]. According to pathological findings, the uterus of a post-menopausal is 7-8 cm long, 5 cm wide, 2.5 cm in diameter, and shaped like an inverted pear with a 6 cm long triangular-shaped uterine cavity and a cervical length of 1-2 cm [102].

## **2.8 Optical Tissue-Equivalent Phantoms**

Radiation consists of electromagnetic waves and subatomic particles, especially high-energy particles that cause ionization [103]. When radiation propagates through biological tissues, it transfers energy, and the interaction can consequently destroy the tissue by causing strand breaks in genetic molecules known as deoxyri-bonucleic acid (DNA) in the nucleus [103]. Such damages are a significant cause of cancers. Therefore, it is imperative to carefully evaluate the radiation energy distribution and absorbed (dose) during imaging procedures [103]. Researchers have developed, and simulated biological tissues or organs herein called phantoms.

Optical phantoms are toxic-free materials that mimic the optical properties of different biological tissues in the visible and near-infrared (NIR) regions for biomedical imaging purposes. These tissue-mimicking materials are created to estimate radiation dose and energy deposition in biological tissues. Furthermore, they play an essential role in training new developing systems. They are designed with optical properties, such as scattering, absorption, refraction, reflection, and transmission, which are experimentally determined using integrating sphere, time-domain diffuse-reflectance, and optoacoustic [104].

Most optical phantoms have low absorption and scattering properties. However, various scattering, absorption materials, and concentrations are added to fabricate

the results of the required tissue. Wrobel et al. (2015) [105] constructed skin phantoms with varying concentrations of gelatin and agar. Optical absorption and scattering in skin phantoms were provided by adding India ink, synthetic melanin, and intralipids. Solid phantoms were fabricated using silicone rubber as the base material by Kennedy et al. (2017) [106]. The phthalocyanine dye and titanium oxide powder were added to obtain the required near-infrared absorption and scattering. This work used PVA slime glue and borax as base materials to produce the slime phantoms. These phantoms have relaxation times similar to actual tissues, are flexible to be moulded with identical size and shape to real biological organs, have good reproducibility, are easy to handle, and are stable over a long period [25].

Optical phantoms can be formed in two states, either liquid or solid. Liquid phantoms are easy to fabricate but difficult to create inhomogeneities such as layered structures, unlike solid phantoms, which are more suitable for reference measurement for living tissue [25]. However, their common characteristic is the controllability of the optical properties during the creation process [25].

## Chapter 3

# Experimental Details

This chapter presents the materials and fabrication process of the polyvinyl alcohol (PVA) slime-based phantoms tuned to specific optical properties of diseased and healthy biological tissues at 532 and 630 nm wavelengths. The phantoms consist of an absorbing medium (Indian ink) and scattering medium ( $Al_2O_3$ ) mixed to correct proportions to the desired intrinsic optical properties of the simulated tissue. Relevant optical characteristics with the phase function of the phantom material were performed by collimated laser beam arrangement and goniometric light scattering measurements.

### 3.1 Optical Tissue Phantom Composition

#### 3.1.1 Bulk Matrix Material

The bulk matrix for phantoms from this work was a slime material formulated by mixing Polyvinyl Alcohol (PVA) slime glue with natural borax powder. Following the mixture, the effective chemical component in borax cross-linked the polyvinyl acetate molecules in the glue to form the viscoelastic slime.

The PVA slime glue (Port Elizabeth, EC, 6025, South Africa) allowed for an easier and more efficient tissue fabrication, unlike PVA dry powders, demanding considerable amount of heating and stirring to dissolve and form the slime material. The synthetic polymer (slime)  $[-CH_2-CH(OH)-]$  is a slow-flowing visco-elastic non-Newtonian fluid that becomes significantly more viscous and brittle when subjected to shear stress. The optically clear and colorless PVA slime glue possess low turbidity and negligible absorption. The slime phantom can be easily compressed and deformed to certain shapes.

Borax powder (Allied drug company, South Africa) also known as sodium borate, sodium tetraborate, or disodium, tetraborate is a boron compound with the chemical formula  $[\text{Na}_2\text{B}_4\text{O}_7 \cdot 10\text{H}_2\text{O}]$ , [107]. This dry powder is a highly alkaline salt hydrolyzed in a water solution to produce a boric acid-borate buffer:  $\text{B}(\text{OH})_3 + 2\text{H}_2\text{O} \rightleftharpoons \text{B}(\text{OH})_4^- + \text{H}_3\text{O}^+$  [107]. Thus, the borate buffers (close to pH 9) act as the cross-linking agent reacting with the -OH group of substances such as PVA slime glue [107].

### 3.1.2 Absorbing Media

India ink (PRO-4100, Pro Art) was selected as the primary absorber. It is a readily available and cheap absorber widely used in tissue simulating phantoms at specific wavelengths [108]. It is added to suspensions of low absorbing diffusive media such as the PVA slime glue to increase the absorption coefficient affected by insoluble carbon particles in an aqueous medium [108]. This absorbing agent (India Ink) is chemically and spectroscopically stable, non-toxic, does not fluoresce, and diffuses in all liquid or solid phantoms states [108]. However, the India ink is not pure absorber exhibiting scattering tendencies due to a small fraction of micron-sized particles.

### 3.1.3 Scattering Particles

Scattering was achieved by adding of Aluminium Oxide ( $\text{Al}_2\text{O}_3$ )(64271, Darmstadt, Germany), an inexpensive and commonly used scattering agent in phantom tissue creation. The aluminium oxide is an effective scatterer because of its high refractive index ( $>2.2$ ). These white metal powders are embedded in suspensions of the low scattering diffuse media to provide the desired scattering coefficient. It does not dissolve entirely in a solution, making it suitable for use in PVA slime glue-based optical tissue phantoms. The main disadvantage of  $\text{Al}_2\text{O}_3$  resides in its suspension in most media, such as PVA slime glue. Therefore, continuous stirring is needed for even distribution.

## 3.2 Optical Properties Measuring Apparatus

### 3.2.1 The Helium-Neon (He-Ne) Laser

To measure the optical properties of the tissue phantoms, we perform light transmission measurements using the experimental set-up depicted in Figure 3.4. Collimated green and red He-Ne 532 nm and 630 nm laser lights (PMS Electro-Optics Div, CO 80301, United States) were employed. The lasers work continuously with an average output of 1W for the green He-Ne laser and 50 mW for the red He-Ne laser.

The laser features includes high stability, efficiency, low noise, excellent beam quality. They are regularly employed for tumour destruction in photodynamic therapy (PDT) following an oral or intravenous administration of a photosensitizing drug.

### 3.2.2 Laser Meter

A Laser power meter detector (Edmund Optics) with an equivalent noise power of  $>10$  mW capable of measuring the power in an optical signal in single-shot power mode and a spectral range of 400-1064 nm was used to measure the power intensities. This easy-to-use device provides traceable measurements at a low cost.



**Figure 3.1:** A Laser Meter.

### 3.2.3 Digital Vernier Caliper

Digital vernier calipers are high-tech precision instruments made of stainless steel to measure the phantom slice thicknesses. Measurements were displayed with superior accuracy (Least count of 0.01mm and accuracy of  $\pm 0.02$ mm). The floating zero feature allows incremental reading values without further calculation, as shown in Figure 3.2.



Figure 3.2: Digital Vernier Caliper.

### 3.3 Experimental Procedures

#### 3.3.1 Fabrication Process of the Slime Phantom Tissue

The following summarizes the procedure adopted in the fabrication of the slime phantoms. The borax powder mixed with distilled water was heated on the hot plate to a temperature between  $65 - 70^{\circ}\text{C}$ , adequate for dissolving the powder. The temperature was measured using a Techgear TG732TK dual channel digital thermometer modified to use a thermocouple attached on the side of a velcro strap with an accuracy of  $\pm 5^{\circ}\text{C}$ . During heating, considerable stirring is required until borax powder is utterly dissolved. The borax solution was allowed to cool and added to the slime glue to produce viscoelastic slime with the chains of PVA cross-linking. The material was, however, subjected to shear stress for brittleness. The quantity of scatterer ( $\text{Al}_2\text{O}_3$ ) and absorber (India ink) used in this experiment were ascertained by a digital balance (with 0.01 g readability) enough to measure the small masses of these components accurately.

### 3.3.2 Slime Phantom Recipe Summary

The tissue-like slime phantoms were fabricated as follows:

- 1) PVA slime glue was placed in the beaker.
- 2) In another beaker, a mixture of borax powder and deionized water was prepared.
- 3) The borax solution was stirred vigorously using a magnetic stirrer on a hot plate until it reached 70°C to allow for the dissolution of all powder granules. The powder's appearance from murky to crystal clear indicates that borax powder was utterly dissolved, and the solution is in a uniform distribution state at this temperature.
- 4) The solution was allowed to cool to about 20°C. An equal concentration of scatterers or absorbers were added in a PVA slime glue and borax solution separately to control homogeneity within the final slime phantom.
- 5) The borax solution was gradually added to PVA slime glue using a 0.3mL syringe, and the substances were blended continuously by a wooden rod after each drop.
- 6) The slime was formed when the borax was completely diffused with PVA slime glue and was then subjected to the shear stress to reach proper hardening and stable optical properties (Figure 3.3).
- 7) Finally, the slime was filled into a beaker, then wrapped with a foil, and placed overnight in a refrigerator to prevent extreme changes in temperature and humidity.

It is imperative to subject a force continuously to the sample to improve the cross-linking process. It usually takes around 30 minutes to become brittle and stable (Figure 3.3).



a). Pure Phantom.



b). Phantom with India Ink.

**Figure 3.3:** Slime Phantom Samples

The quantity of PVA slime glue, borax solution,  $Al_2O_3$  and India Ink used are given in Table 3.1:

**Table 3.1:** Slime phantom recipes with the wavelengths and mimicked tissue types.

Mimicked tissue	PVA slime glue (ml)	Borax (g/l)	$Al_2O_3$ (g)	India Ink (ml)	$\lambda$ (nm)
Brain	100	30		0.4	532
Lung Carcinoma	100	30		0.6	630
Post-menopausal Uterus	100	30	0.4	0.4	630
Malignant Brain Tumor	100	60		0.4	630

### 3.3.3 Experimental set-up

The experimental set-up to determine the optical properties of the created phantom tissues is shown in Figure 3.4.



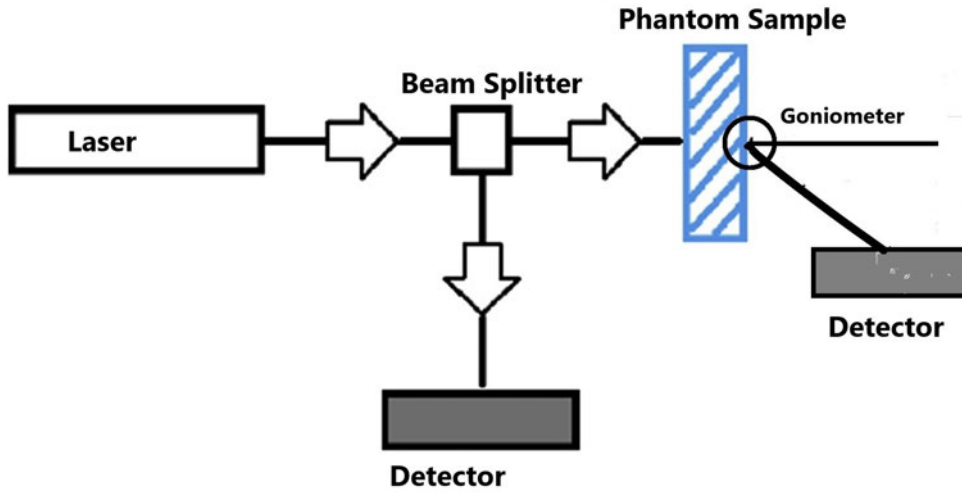


**Figure 3.4:** The set-up of apparatus for this experiment.

The laser beams 532 nm and 630 nm placed at a constant distance from the sample were directed on each sample slice. The incident beam power was continuously monitored by a 25 mm diameter cube beam splitter (Edmund Optics, USA). Varying thickness ( $L$ ) was mounted on a holder, a slice holder perpendicular to the incident light power ( $P_0$ ) with) and the transmitted light power ( $P$ ) as the function of  $\theta$  ranging between ( $0-90^\circ$ ). Light incident on the phantom is scattered into an element of solid angle  $d\Omega$  direction ( $\theta, \phi$ ). These power intensities were collected in mW using an EO 54-018 digital handheld laser power meter (Edmund Optics, USA). The ray optics technique detected the single scattered light relative to the normal line, and the scattering angle was estimated using a goniometer.

### 3.3.4 Measurements of Optical Properties

Measurements of the laser light power incident and transmitted through each slice were obtained (in mW) by directly squeezing varying thicknesses of the slime sample between glasses for appropriateness. The optical contact between the slime surfaces was improved for perfect scattering with a saline solution. The actual thickness was measured using digital vernier calipers. All measurements were performed at room temperature.

A comprehensive optical measuring technique specific to desired tissue phantoms is illustrated in the published manuscripts in chapters 5 and 6.

## Chapter 4

# Results

### The Optical Properties of Simulated Tissue Samples

The optical properties of the fabricated samples at 532 and 630 nm wavelengths are presented in this chapter. Measurements of scattering function at small scattering angles ( $<10^\circ$ ) were carried out on thin slices. The range of optical thicknesses ( $L$ ) was tested, and  $L \leq 3$  mm showed significant minor multiple scattering effects. Each value reported is the average of the four repeated measurements on each thickness. The optical properties were determined by plotting the logarithmic intensities  $-\ln[\frac{P}{P_0}]$  of the collimated laser beam as a function of sample thickness  $L$  for each sample.

The absorption of the PVA slime glue base material was negligible; hence the assumption,  $\mu_t \approx \mu_s$ , was made in all samples.

#### 4.1 Brain Samples

The tissue-like samples created to mimic the optical properties of the human brain tissues at 532 nm.

**Table 4.1:** The power intensities of the 532 nm laser through a pure slime phantom sample, obtained by mixing 30g/l concentration of borax with 100 ml of PVA slime glue.

$L(\text{mm})$	Incident Power(mW)	Transmitted Power(mW)	$-\ln[\frac{P}{P_0}]$	$u_t \approx \mu_s$	$\theta(\text{deg})$	$g$
0.53	38.07	26.07	0.379	0.714	1	0.923
1.10	39.97	23.07	0.550	0.500	2,5	0.985
1.53	38.97	19.17	0.709	0.464	3	0.988
2.04	38.77	15.07	0.945	0.463	5	0.991
2.55	38.17	11.17	1.229	0.482	5.5	0.980
3.10	36.27	8.07	1.503	0.485	6	0.986
1.81				0.518		0.976

A sample calculation for the results obtained in Table 4.1, for the first measurement of attenuation coefficient:

$$\begin{aligned}\mu_t &= -\frac{1}{L} \ln\left(\frac{P}{P_0}\right) \\ \mu_t &= -\frac{1}{0.53} \ln\left(\frac{26.07}{38.07}\right) \\ \mu_t &= 0.741 \text{ mm}^{-1}\end{aligned}$$

The first measurement of anisotropy factor ( $g$ ), obtained by using **Wolfram Mathematica** program:

$$\begin{aligned}P(\theta) &= K \left[ \frac{1 - g^2}{1 + g^2 - 2 \cos(\theta) g} \right]^{3/2} \\ \text{In[39]} &= \text{Solve}\left[26.07 == 0.0796 \times \left[ \frac{1 - g^2}{1 + g^2 - 2 \times (1) g} \right]^{3/2}, g\right] // \text{N} \\ \text{Out[39]} &= \{\{g \rightarrow 0.923367\}\}\end{aligned}$$

**Figure 4.1:** A sample calculation of anisotropy factor( $g$ ) using Wolfram Mathematica.

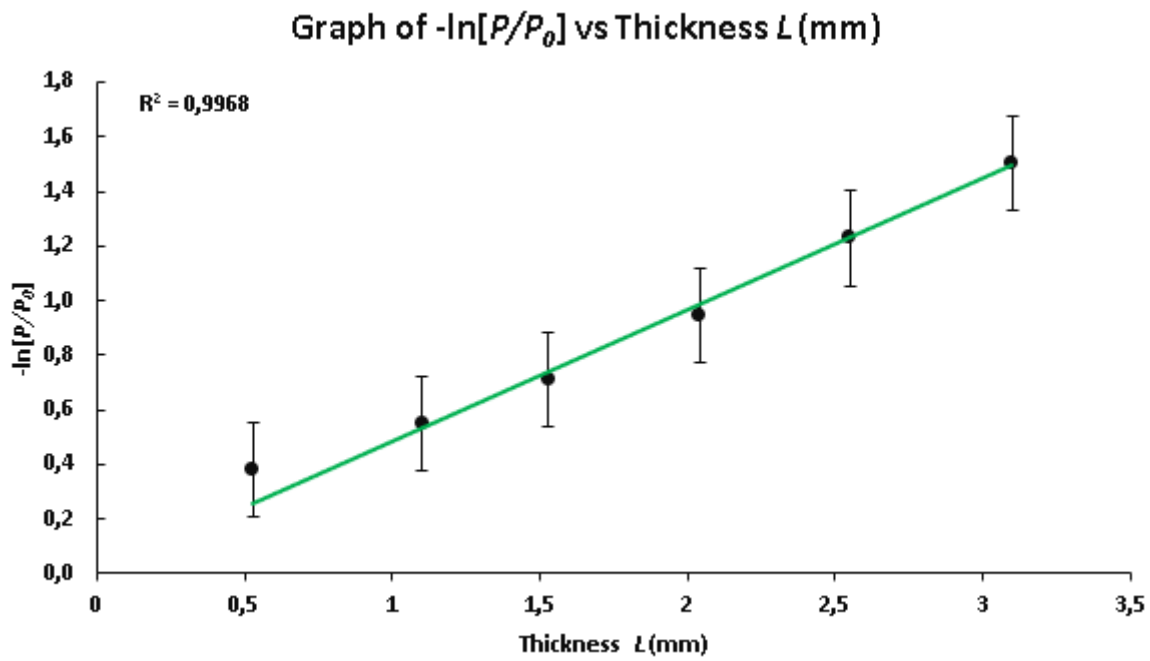


**Figure 4.2:** Graph of  $-\ln\left(\frac{P}{P_0}\right)$  vs  $L$  to determine the attenuation coefficient  $\mu_t$ , represented by the slope in the equation of the linear fit.

**Table 4.2:** The power intensities of the 532 nm laser through the same mixture of 30g/l concentration of borax with 100 ml of PVA slime glue, and 0.4 ml of India Ink, to assess the effects of adding absorbers on total attenuation coefficients.

$L$ (mm)	Incident Power(mW)	Transmitted Power(mW)	$-\ln\left[\frac{P}{P_0}\right]$	$u_t$
0.52	35.17	20.97	0.517	0.994
1.01	36.07	16.17	0.802	0.794
1.51	35.77	11.97	1.095	0.725
2.02	36.07	8.97	1.392	0.689
2.55	37.77	5.57	1.914	0.751
3.01	36.97	3.27	2.425	0.806
1.77				0.793

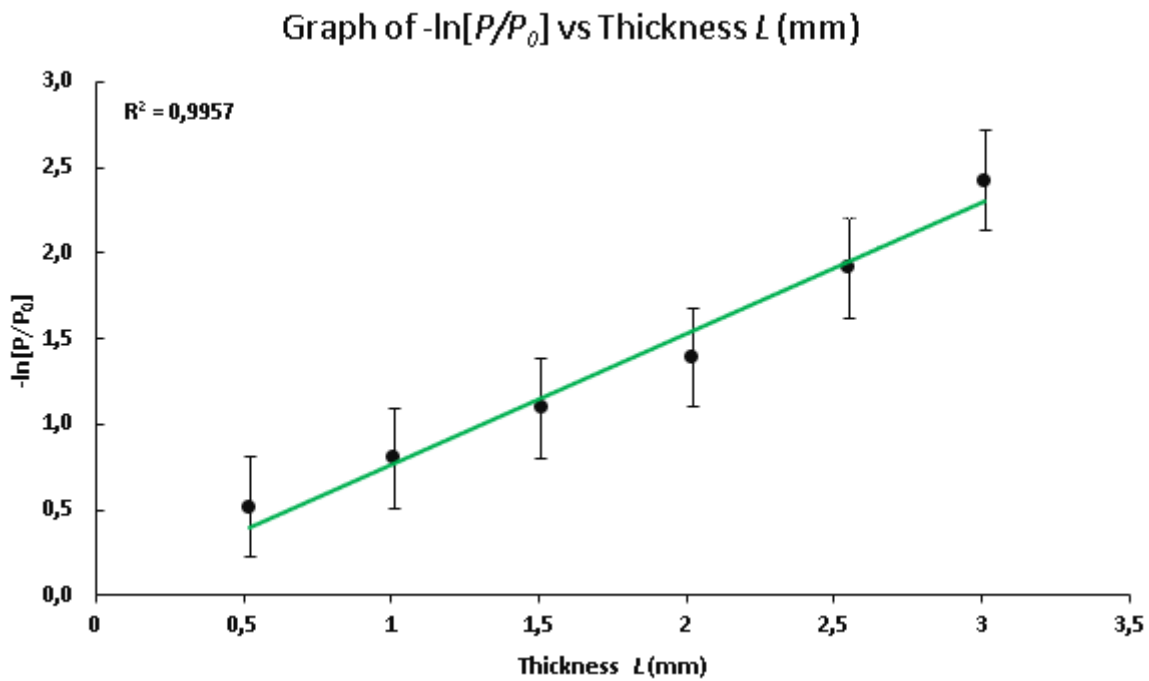


**Figure 4.3:** Graph of  $-\ln\left(\frac{P}{P_0}\right)$  vs  $L$  to determine the attenuation coefficient  $\mu_t$ , represented by the slope in the equation of the linear fit.

#### 4.1.1 Analysis of brain slime phantom samples

##### Attenuation Coefficients

**Table 4.3:** The results obtained by calculation and graphically from the slope of the best fit line.

PVA slime glue sample	[Calculated] $\mu_t(mm^{-1})$	[Graphical] $\mu_t(mm^{-1})$
Pure	0.518	0.482
0.4 ml of India Ink	0.793	0.764

The attenuation coefficient is greater in PVA slime phantom with 0.4 ml of India Ink, a good indication of the effectiveness of the India Ink (absorbers) at this wavelength.

##### Reduced Scattering Coefficient

By considering the assumption ( $\mu_t \approx \mu_s$ ) for the pure sample, the average scattering coefficient obtained graphically (Table 4.3) and the anisotropy factor (Table 4.1) was

used to estimate the reduced scattering:

$$\begin{aligned}\mu_t' &= (1 - g) \mu_s \\ \mu_t' &= (1 - 0.976)(0.482) \\ \mu_t' &= 0.0116 \text{ mm}^{-1}\end{aligned}$$

### Determination of the Absorption Coefficient

The phantom sample with India Ink had a higher attenuation coefficient  $\mu_t$  of  $0.764 \text{ mm}^{-1}$  and a scattering coefficient  $\mu_s$  of  $0.482 \text{ mm}^{-1}$ . From this, it was possible to deduce the absorption attributable to the added India Ink using the equation,

$$\begin{aligned}\mu_a &= \mu_t - \mu_s \\ \mu_a &= 0.764 - 0.482 \\ \mu_a &= 0.282 \text{ mm}^{-1}\end{aligned}$$

### Optical Albedo

$$\begin{aligned}a &= \frac{\mu_s}{\mu_t} = \frac{0.482}{0.764} \\ a &= 0.63\end{aligned}$$

Hence 63% of the attenuation in the sample was due to scattering property and the other portion (37 %) was caused by absorption.

### Effective Attenuation Coefficient

It is the function of reduced scattering and absorption coefficient:

$$\begin{aligned}\mu_{eff} &= [(3\mu_a(\mu_a + \mu_s'))^{\frac{1}{2}}] \\ \mu_{eff} &= [(3(0.282)(0.282 + 0.0116))^{\frac{1}{2}}] \\ \mu_{eff} &= 0.498 \text{ mm}^{-1}\end{aligned}$$

### Penetration Depth

The reciprocal of the effective attenuation coefficient provides the penetration depth:

$$\begin{aligned}\delta &= \frac{1}{\mu_{eff}} \\ \delta &= \frac{1}{0.498} \\ \delta &= 2.008 \text{ mm}\end{aligned}$$

## 4.2 Lung carcinoma Samples

The tissue-like samples were created to mimic the optical properties of the human lung carcinoma tissues at 630 nm.

**Table 4.4:** The power intensities of the 630 nm laser through a pure slime phantom sample, obtained by mixing 30g/l concentration of borax with 100 ml of PVA slime glue.

$L(\text{mm})$	Incident Power(mW)	Transmitted Power(mW)	$-\ln[\frac{P}{P_0}]$	$u_t \approx \mu_s$	$\theta(\text{deg})$	$g$
0.51	4.22	3.61	0.156	0.306	1.5	0.999
1.08	4.42	3.36	0.274	0.254	4	0.992
1.48	4.38	3.02	0.372	0.251	5.25	0.986
2.05	4.48	2.70	0.507	0.247	6.5	0.973
2.52	4.32	2.26	0.649	0.257	7	0.973
3.06	4.24	1.90	0.804	0.263	7.5	0.972
1.78				0.263		0.983

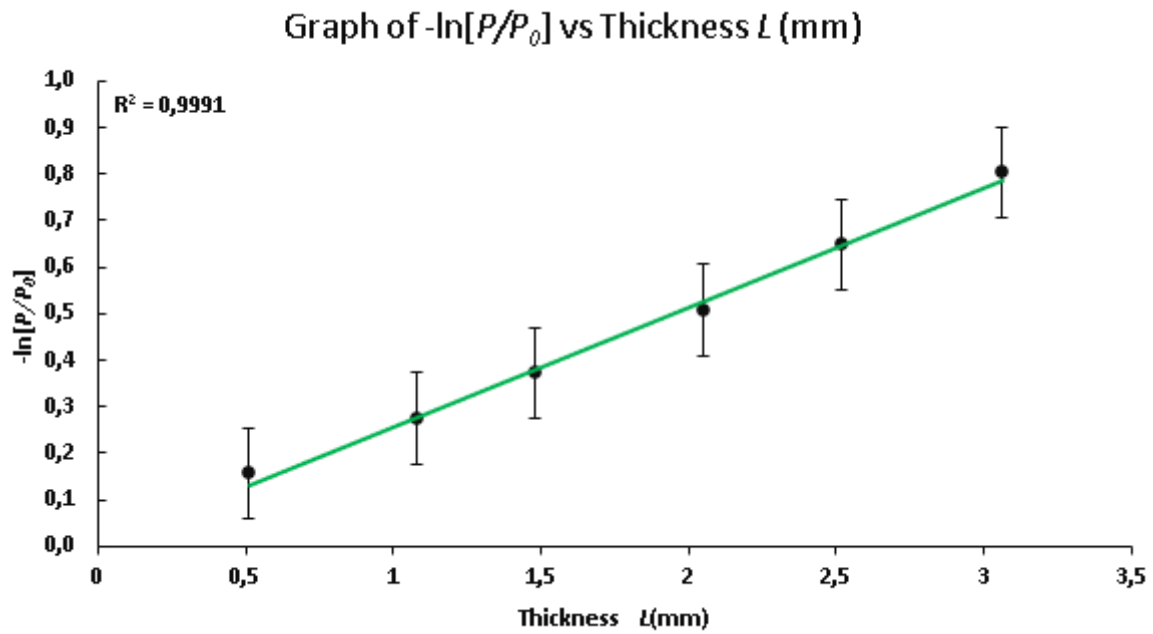


**Figure 4.4:** Graph of  $-\ln\left(\frac{P}{P_0}\right)$  vs  $L$  to determine the attenuation coefficient  $\mu_t$ , represented by the slope in the equation of the linear fit.

**Table 4.5:** The power intensities of the 630 nm laser through the same mixture of 30g/l concentration of borax with 100 ml of PVA slime glue, and 0.6 ml of India Ink, to assess the effects of adding absorbers on total attenuation coefficients.

$L(\text{mm})$	Incident Power(mW)	Transmitted Power(mW)	$-\ln\left[\frac{P}{P_0}\right]$	$u_t$
0.51	4.30	3.08	0.334	0.655
1.08	4.95	2.60	0.644	0.597
1.56	4.99	2.13	0.852	0.546
2.03	5.00	1.66	1.104	0.544
2.56	4.88	1.14	1.456	0.569
3.02	4.97	0.72	1.935	0.592
1.79				0.584

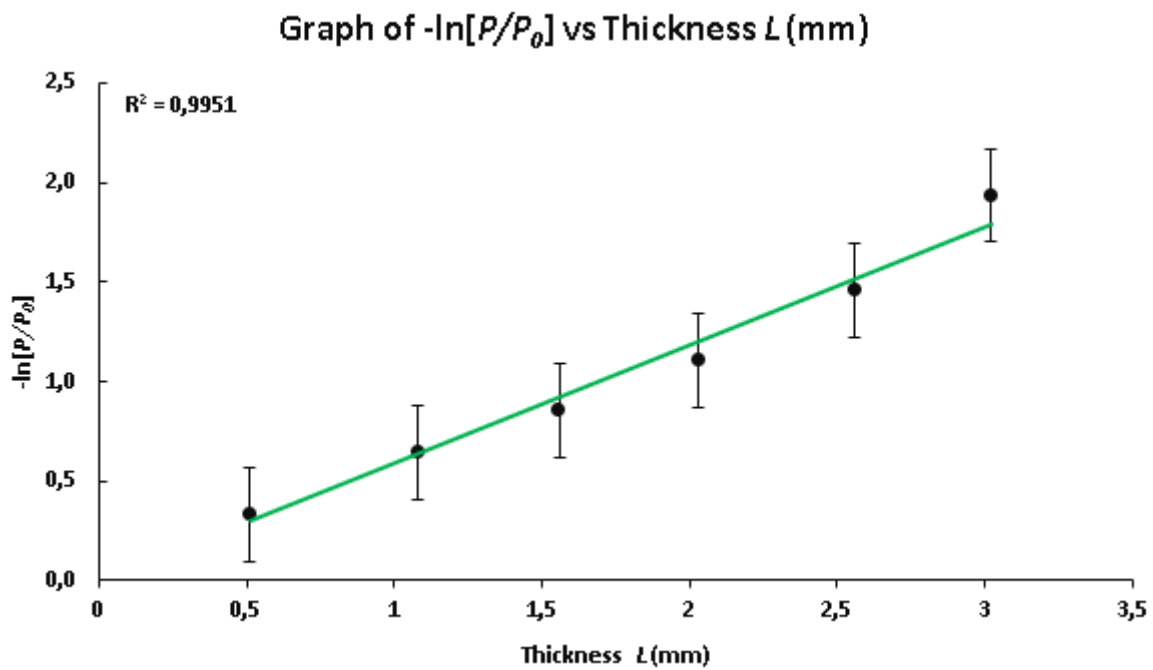


**Figure 4.5:** Graph of  $-\ln\left(\frac{P}{P_0}\right)$  vs  $L$  to determine the attenuation coefficient  $\mu_t$ , represented by the slope in the equation of the linear fit.



### 4.2.1 Analysis of lung carcinoma slime phantom samples

#### Attenuation Coefficients

**Table 4.6:** The results obtained by calculation and graphically from the slope of the best fit line.

PVA slime glue sample	[Calculated] $\mu_t(mm^{-1})$	[Graphical] $\mu_t(mm^{-1})$
Pure	0.263	0.258
0.6 ml of India Ink	0.584	0.592

The attenuation coefficient is greater in PVA slime phantom with 0.6 ml of India Ink, a good indication of the effectiveness of the India Ink (absorbers) at this wavelength.

#### Reduced Scattering Coefficient

The average scattering coefficient obtained from the graph (Table 4.6) based on the assumption ( $\mu_t \approx \mu_s$ ), and the anisotropy factor (Table 4.4) was used to estimate reduced scattering as follows,

$$\begin{aligned}\mu_t' &= (1 - g) \mu_s \\ \mu_t' &= (1 - 0.983)(0.258) \\ \mu_t' &= 0.00439 \text{ mm}^{-1}\end{aligned}$$

#### Determination of the Absorption Coefficient

The phantom sample with India Ink had a higher attenuation coefficient  $\mu_t$  of 0.592  $\text{mm}^{-1}$  and a scattering coefficient  $\mu_s$  of 0.258  $\text{mm}^{-1}$ . From this, it was possible to deduce the absorption attributable to the added India Ink using the equation:

$$\begin{aligned}\mu_a &= \mu_t - \mu_s \\ \mu_a &= 0.592 - 0.258 \\ \mu_a &= 0.334 \text{ mm}^{-1}\end{aligned}$$

#### Optical Albedo

$$\begin{aligned}a &= \frac{\mu_s}{\mu_t} = \frac{0.258}{0.592} \\ a &= 0.44\end{aligned}$$

Hence 44% of the attenuation in the sample was due to scattering property and the other portion (56 %) was caused by absorption.

### Effective Attenuation Coefficient

$$\begin{aligned}\mu_{eff} &= [(3\mu_a(\mu_a + \mu'_s))^{\frac{1}{2}}] \\ \mu_{eff} &= [(3(0.334)(0.334 + 0.00439))^{\frac{1}{2}}] \\ \mu_{eff} &= 0.582 \text{ mm}^{-1}\end{aligned}$$

### Penetration Depth

$$\begin{aligned}\delta &= \frac{1}{\mu_{eff}} \\ \delta &= \frac{1}{0.582} \\ \delta &= 1.718 \text{ mm}\end{aligned}$$

## 4.3 Post-menopausal uterus Samples

The tissue-like samples were created to mimic the optical properties of the human post-menopausal uterus tissues at 630 nm.

**Table 4.7:** The power intensities of the 630 nm laser through a mixture of 30g/l concentration of borax with 100 ml of PVA slime glue and 0.4 ml of  $Al_2O_3$ , to assess the effects of adding scatterers on total attenuation coefficients.

$L(\text{mm})$	Incident Power(mW)	Transmitted Power(mW)	$-\ln[\frac{P}{P_0}]$	$u_t \approx \mu_s$	$\theta(\text{deg})$	$g$
0.54	4.02	2.79	0.366	0.677	5.5	0.985
1.00	4.02	2.39	0.520	0.520	6	0.982
1.50	4.59	1.96	0.852	0.568	7	0.977
2.03	4.95	1.61	1.124	0.554	9	0.957
2.53	4.91	1.21	1.403	0.554	9	0.969
3.00	5.00	0.84	1.787	0.596	10	0.972
1.77				0.578		0.974

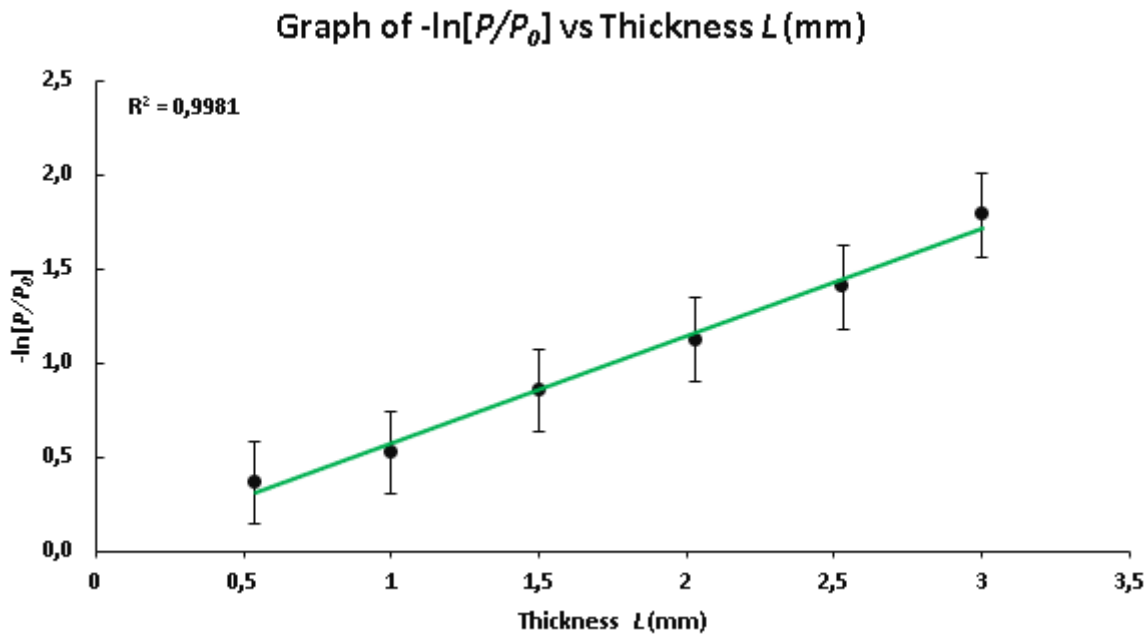


**Figure 4.6:** Graph of  $-\ln\left(\frac{P}{P_0}\right)$  vs  $L$  to determine the attenuation coefficient  $\mu_t$ , represented by the slope in the equation of the linear fit.

**Table 4.8:** The power intensities of the 630 nm laser through the same mixture of 30g/l concentration of borax with 100 ml of PVA slime glue, 0.4 ml of  $Al_2O_3$  and 0.4 ml of India Ink, to assess the effects of adding scatterers and absorbers on total attenuation coefficients.

$L(\text{mm})$	Incident Power(mW)	Transmitted Power(mW)	$-\ln\left[\frac{P}{P_0}\right]$	$u_t$
0.55	4.04	2.48	0.488	0.888
1.00	4.05	1.97	0.721	0.721
1.53	5.11	1.56	1.188	0.776
2.01	5.01	1.17	1.456	0.725
2.55	5.10	0.79	1.868	0.733
3.05	5.09	0.39	2.576	0.845
1.78				0.781

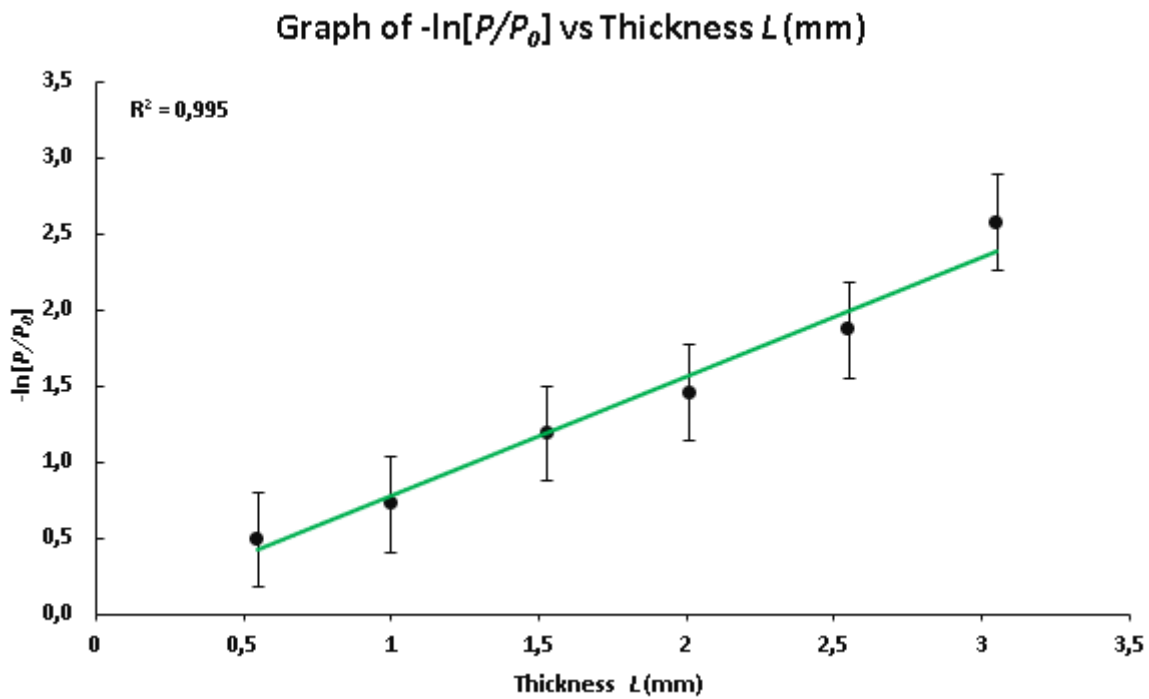


**Figure 4.7:** Graph of  $-\ln\left(\frac{P}{P_0}\right)$  vs  $L$  to determine the attenuation coefficient  $\mu_t$ , represented by the slope in the equation of the linear fit.

#### 4.3.1 Analysis of post-menopausal uterus slime phantom samples

##### Attenuation Coefficients

**Table 4.9:** The results obtained by calculation and graphically from the slope of the best fit line.

PVA slime glue sample	[Calculated] $\mu_t(mm^{-1})$	[Graphical] $\mu_t(mm^{-1})$
sample with 0.4 ml of $Al_2O_3$	0.578	0.572
0.4 ml of India Ink and 0.4 ml of $Al_2O_3$	0.781	0.782

The attenuation coefficient is greater in PVA slime phantom with 0.4 ml of  $Al_2O_3$  and 0.4 ml of India Ink, a good indication of the effectiveness of the India Ink (absorbers) and  $Al_2O_3$  (scatterers) at this wavelength.

### Reduced Scattering Coefficient

By considering the assumption ( $\mu_t \approx \mu_s$ ) for the pure sample, the average scattering coefficient obtained graphically (Table 4.9) and the anisotropy factor (Table 4.7) was used to estimate the reduced scattering:

$$\begin{aligned}\mu_t' &= (1 - g) \mu_s \\ \mu_t' &= (1 - 0.974)(0.572) \\ \mu_t' &= 0.0149 \text{ mm}^{-1}\end{aligned}$$

### Determination of the Absorption Coefficient

The phantom sample with India Ink and  $Al_2O_3$  had a higher attenuation coefficient  $\mu_t$  of  $0.782 \text{ mm}^{-1}$  and a scattering coefficient  $\mu_s$  of  $0.572 \text{ mm}^{-1}$ . From this, it was possible to deduce the absorption attributable to the added India Ink using the equation:

$$\begin{aligned}\mu_a &= \mu_t - \mu_s \\ \mu_a &= 0.782 - 0.572 \\ \mu_a &= 0.21 \text{ mm}^{-1}\end{aligned}$$

### Optical Albedo

$$\begin{aligned}a &= \frac{\mu_s}{\mu_t} = \frac{0.572}{0.782} \\ a &= 0.73\end{aligned}$$

Hence 73 % of the attenuation in the sample was due to scattering property and the other portion (27 %) was caused by absorption.

### Effective Attenuation Coefficient

$$\begin{aligned}\mu_{eff} &= [(3\mu_a(\mu_a + \mu_s'))^{\frac{1}{2}}] \\ \mu_{eff} &= [(3(0.21)(0.21 + 0.0149))^{\frac{1}{2}}] \\ \mu_{eff} &= 0.376 \text{ mm}^{-1}\end{aligned}$$

### Penetration Depth

$$\begin{aligned}\delta &= \frac{1}{\mu_{eff}} \\ \delta &= \frac{1}{0.376} \\ \delta &= 2.66 \text{ mm}\end{aligned}$$

## 4.4 Malignant brain tumor Samples

The tissue-like samples were created to mimic the optical properties of the human malignant brain tumor tissues at 630 nm.

**Table 4.10:** The power intensities of the 630 nm laser through a mixture of 60g/l concentration of borax with 100 ml of PVA slime glue.

$L(\text{mm})$	Incident Power(mW)	Transmitted Power(mW)	$-\ln[\frac{P}{P_0}]$	$u_t \approx \mu_s$	$\theta(\text{deg})$	$g$
0.53	4.46	3.27	0.311	0.586	4	0.993
1.01	4.18	2.83	0.390	0.387	4.8	0.989
1.52	4.81	2.39	0.700	0.461	6	0.982
2.04	4.94	1.96	0.925	0.454	7	0.977
2.50	4.60	1.61	1.051	0.420	8	0.973
3.02	4.72	1.19	1.380	0.457	9.5	0.966
1.77				0.461		0.980

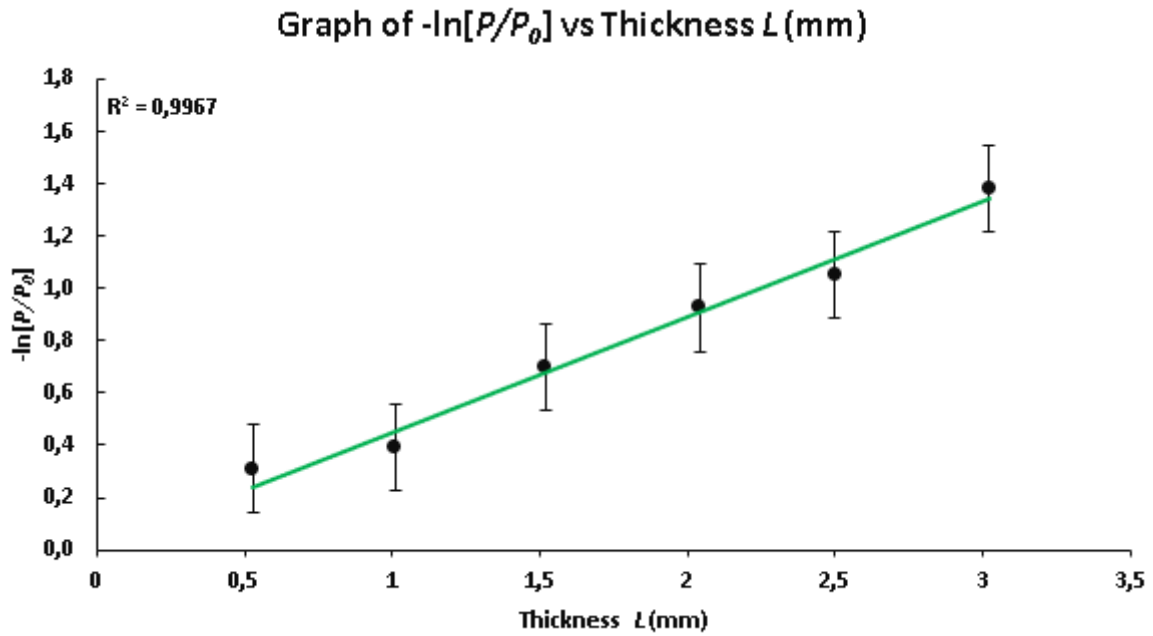


**Figure 4.8:** Graph of  $-\ln\left(\frac{P}{P_0}\right)$  vs  $L$  to determine the attenuation coefficient  $\mu_t$ , represented by the slope in the equation of the linear fit.

**Table 4.11:** The power intensities of the 630 nm laser through the same mixture of 60g/l concentration of borax with 100 ml of PVA slime glue, and 0.4 ml of India Ink, to assess the effects of adding absorbers on total attenuation coefficients.

$L(\text{mm})$	Incident Power(mW)	Transmitted Power(mW)	$-\ln\left[\frac{P}{P_0}\right]$	$u_t$
0.49	4.03	2.89	0.333	0.679
1.03	4.21	2.34	0.588	0.571
1.52	4.39	1.89	0.830	0.546
2.01	4.62	1.40	1.195	0.595
2.56	4.58	1.07	1.453	0.568
3.11	4.67	0.71	1.888	0.607
1.79				0.594

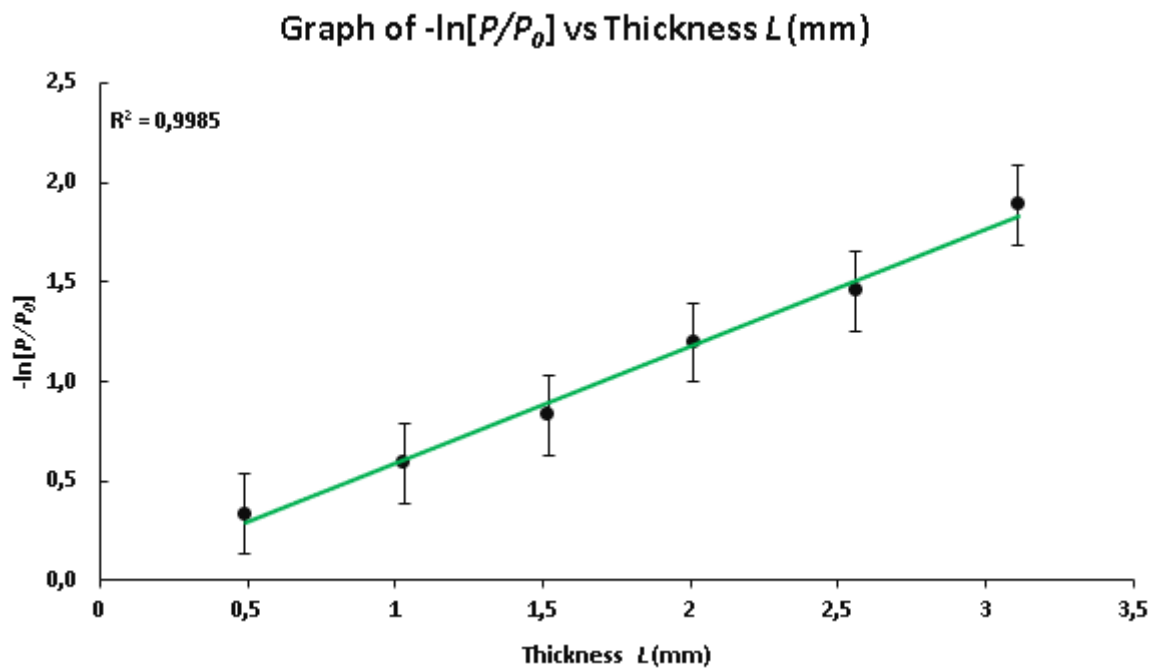


**Figure 4.9:** Graph of  $-\ln\left(\frac{P}{P_0}\right)$  vs  $L$  to determine the attenuation coefficient  $\mu_t$ , represented by the slope in the equation of the linear fit.

#### 4.4.1 Analysis of malignant brain tumor slime phantom samples

##### Attenuation Coefficients

**Table 4.12:** The results obtained by calculation and graphically from the slope of the best fit line.

PVA slime glue sample	[Calculated] $\mu_t(mm^{-1})$	[Graphical] $\mu_t(mm^{-1})$
Pure	0.461	0.445
0.4 ml of India Ink	0.594	0.587

The attenuation coefficient is greater in PVA slime phantom with 0.4 ml of India Ink, a good indication of the effectiveness of the India Ink (absorbers) at this wavelength.

##### Reduced Scattering Coefficient

The average scattering coefficient obtained from the graph (Table 4.14) based on the assumption ( $\mu_t \approx \mu_s$ ), and the anisotropy factor (Table 4.12) was used to estimate reduced scattering as follows,

$$\begin{aligned}\mu_t' &= (1 - g) \mu_s \\ \mu_t' &= (1 - 0.980) (0.445) \\ \mu_t' &= 0.0089 \text{ mm}^{-1}\end{aligned}$$

##### Determination of the Absorption Coefficient

The phantom sample with India Ink had a higher attenuation coefficient  $\mu_t$  of 0.587  $\text{mm}^{-1}$  and a scattering coefficient  $\mu_s$  of 0.445  $\text{mm}^{-1}$ . From this, it was possible to deduce the absorption attributable to the added India Ink using the equation:

$$\begin{aligned}\mu_a &= \mu_t - \mu_s \\ \mu_a &= 0.587 - 0.445 \\ \mu_a &= 0.142 \text{ mm}^{-1}\end{aligned}$$

##### Optical Albedo

$$\begin{aligned}a &= \frac{\mu_s}{\mu_t} = \frac{0.445}{0.587} \\ a &= 0.76\end{aligned}$$



Hence 76 % of the attenuation in the sample was due to scattering property and the other portion (24 %) was caused by absorption.

### Effective Attenuation Coefficient

$$\begin{aligned}\mu_{eff} &= [(3\mu_a(\mu_a + \mu'_s))]^{\frac{1}{2}} \\ \mu_{eff} &= [(3(0.142)(0.142 + 0.0089))]^{\frac{1}{2}} \\ \mu_{eff} &= 0.254 \text{ mm}^{-1}\end{aligned}$$

### Penetration Depth

$$\begin{aligned}\delta &= \frac{1}{\mu_{eff}} \\ \delta &= \frac{1}{0.254} \\ \delta &= 3.94 \text{ mm}\end{aligned}$$

## 4.5 Source of Errors

The experimental setup was sufficient enough to provide significant results. However, possible source of errors might includes:

- The measuring ability of the hand-held power meter and correcting the power to three figures.
- Inherent challenges with creating a homogeneous sample with evenly distributed scatterers and absorbers.
- Air bubbles during vigorous mixing in the slime lead to additional and irreproducible scattering.
- Obtaining precise values on the goniometer.
- The unaccounted multiple scattering effects of the laser light.

## Chapter 5

# Effective Attenuation Coefficient and Penetration Depth of 630nm Laser Light In Polyvinyl Alcohol Slime Glue Phantoms Simulating the Human Brain Tumour

1

---

<sup>1</sup>Lindokuhle Ntombela, Naven Chetty, Bamise Adeleye. Effective attenuation coefficient and penetration depth of 630nm laser light in polyvinyl alcohol slime glue phantoms simulating the human brain tumour. *Proceedings of the Estonian Academy of Sciences*, 2022, **71**, 3, 221-226.

---

## Effective Attenuation Coefficient and Penetration Depth of 630nm Laser Light In Polyvinyl Alcohol Slime Glue Phantoms Simulating the Human Brain Tumour

Lindokuhle Ntombela, Naven Chetty\* (0000-0002-0916-578X), Bamise Adeleye  
(0000-0003-0964-8973)

School of Physics and Chemistry, University of KwaZulu–Natal,  
Private Bag X01, Scottsville 3209, South Africa  
**Email:** : chettyn3@ukzn.ac.za and **Tel** : +27721295525

### ABSTRACT

The effectiveness of optical methods such as photodynamic therapy (PDT) depends on the amount of light distribution within the tissue to aid their potential for early cancer detection in a quantitative and non-invasive manner. Knowledge of the effective attenuation coefficient and penetration depth for the laser light is crucial to ensuring the tumour tissue receives adequate optical energy. This study investigated the effective attenuation coefficient and penetration depth of He-Ne 630 nm red laser light in polyvinyl alcohol slime glue phantoms simulating the human brain tumorous tissues. The effective attenuation coefficient ( $\mu_{eff}$ ) and penetration depth ( $\delta$ ) were deduced from absorption coefficient ( $\mu_a$ ), scattering coefficient ( $\mu_s$ ), and anisotropy factor ( $g$ ) obtained from Henyey-Greenstein (H-G) function with collimated laser beam measurements. We found the effective attenuation coefficient ( $\mu_{eff}$ ) and penetration depth ( $\delta$ ) as  $0.25 \pm 0.02 \text{ mm}^{-1}$  and 4.00 mm in the simulated phantoms. These values were in reasonable agreement with values reported for malignant human brain tumours tissue in literature. The constructed phantoms would be an excellent tool for the continued evaluation of PDT as an essential therapeutic procedure in cancer management.

**Keywords:** Biomedical physics, Polyvinyl alcohol (PVA) slime, Effective attenuation coefficient, Penetration depth, He-Ne Laser.

## 5.1 INTRODUCTION

An accurate and early diagnosis of cancerous tissue is a crucial factor in reducing mortality and management costs. The cancer cells multiply uncontrollably to crowd healthy areas of the affected tissue, consequently forming a tumour lump. Brain tumours known as intracranial tumours occur when brain cells show abnormal growth ranging from benign to malignant and eventually metastatic [109].

Biomedical imaging techniques have emerged as a useful resource in all phases of cancer management, including screening, detection, staging, and treatment [110, 111]. Existing imaging modalities to have shown great capabilities for cancer cells are positron emission tomography (PET), computed tomography (CT), magnetic resonance imaging (MRI), and optical imaging [112–116]. The several contrast mechanisms for identifying normal from pathologic process and tissues of optical imaging with relatively simple instrumentation and speed have raised interest in the technology [117, 118]. Laser light interaction with tissues includes the attenuation and penetration of light as a function of absorption and scattering properties. These optical properties are utilized to obtain biochemical and morphological information about specific cells [111, 117]. However, it is still challenging to accurately heat a deep-seated tumour, such as a malignant brain tumour, with appropriate power intensity [119]. The probability that an interaction will occur when photon energy passes through a target tissue depends on the tissue's energy, composition, and thickness [120], which magnitude varies among different tissues. Measurement employing a phantom with appropriate optical properties to the desired tumour tissue are essential to thoroughly estimate the amount of laser light needed to heat a tumour [119]. Phantoms mimicking the brain tumour should be of non-toxic materials, practical imaging applications, specifically ultrasound attenuation and CT contrast. Such optical phantoms must also hold important vital properties as durability, similar mechanical behaviour to the human tissue so that it can be handled and used repeatedly [121, 122]. The phantom slime material considered for this study was formulated by mixing Polyvinyl Alcohol (PVA) slime glue with natural borax powder [ $\text{Na}_2\text{B}_4\text{O}_7 \cdot 10\text{H}_2\text{O}$ ]. After mixing the substances, the effective chemical component in borax cross-linked the polyvinyl acetate molecules in glue together to form the viscoelastic slime [123].

A major advantage of PVA based phantoms is their superior mechanical properties, which are readily adjustable over the range found in tissue by varying its freeze-thaw cycles [121, 122]. They show good optical transparency, a high degree of elasticity, lower surface friction resistance suitable for applications such as blood vessel biomedeling, with good acoustic and durability properties [121, 124, 125].

Considerable studies on PVA slime-based phantoms have already been performed

with valuable results. Hebden et al [123]. presented a novel design of highly compressible phantoms for diffuse optical tomography with polyvinyl alcohol (PVA) slime as the principal component mixed with scattering or absorbing agents for reproducible optical properties. They established that phantoms of arbitrary size and shape might be produced by containing the slime within a thin latex shell with constant properties for at least three months [123]. The effect of poly (ethylene oxide) (PEO) on the mechanical properties of PVA/ borax gels and capability of retaining and improving interactions with miscible organic solvents in conservation applications was investigated by Riedo et al [126]. The addition of PEO to the PVA/ borate dispersion modifies the viscoelastic behaviour of the gels and the liquid phase retention with an increase of the apparent gel relaxation time, the dispersions stability, and their ability to maintain the shape after use. Yusoff et al [127]. investigated the homogeneity and stability of poly (vinyl alcohol) (PVA) slime phantom and its suitability and potential as MRI phantoms. The results were promising as the signal-to-noise (SNR), T1, and T2 values of the fabricated phantoms were stable over time and in good agreement with the average values of human tissues.

This study designed and developed PVA slime phantom tissues to determine the effective attenuation coefficient and optical penetration depth compatible with values reported for a malignant human brain tumour at 630 nm. The low-power red light (emitting 630 nm) is regularly employed for tumour destruction following the oral or intravenous administration of a photosensitizing drug in photodynamic therapy (PDT). Evaluating the penetration depths for tissues with phantom materials with relative ease of fabrication and controllable properties to real tissues is essential for correct dosimetry.

## 5.2 MATERIALS AND METHODS

### 5.2.1 Phantom composition and recipe

The slime phantoms were prepared with Poly (vinyl alcohol) slime glue (Port Elizabeth, EC, 6025, South Africa), Borax powder (sodium tetraborate decahydrate (Allied drug company, South Africa), and India ink (PRO-4100, Pro Art). The fabrication process involved the following steps:

- 3 g of Borax powder [ $\text{Na}_2\text{B}_4\text{O}_7 \cdot 10\text{H}_2\text{O}$ ] was dissolved in a beaker containing 50 ml of deionized water. The borax solution was stirred vigorously on the hot plate with a magnetic stirrer until it reached  $70^\circ\text{C}$  to dissolve the powder granules completely.
- The powder appearance changed from murky to crystal clear, indicating that the borax powder was utterly dissolved and the solution in uniform distribution at this temperature.
- The borax solution was allowed to cool to about  $20^\circ\text{C}$  while 100 ml of PVA slime glue was prepared in a second beaker.
- The absorption properties were induced by adding 0.4 ml of India ink while the borax solution was gradually added using a 20-ml syringe, and the solution was stirred gently with a wooden rod.
- The India ink (PRO-4100, Pro Art) was added slowly to increase the internal absorption of the slime phantom.
- The slime phantom was formed when the borax completely diffused with the PVA glue chains. The fabricated phantom was then subjected to shear stress for brittleness.
- Lastly, the slime phantom was filled into a beaker, wrapped with foil, and placed overnight in a refrigerator to allow for full cross-link and prevent extreme changes in temperature and humidity.
- During the heating process, the temperature of the sample was monitored using a techgear TG732TK dual channel digital thermometer modified to utilize a thermocouple attached on the reverse side of a Velcro strap. The digital thermocouple strapped around the beaker provides accurate temperature measurements of the heated solution on the accuracy of  $\pm 5^\circ\text{C}$

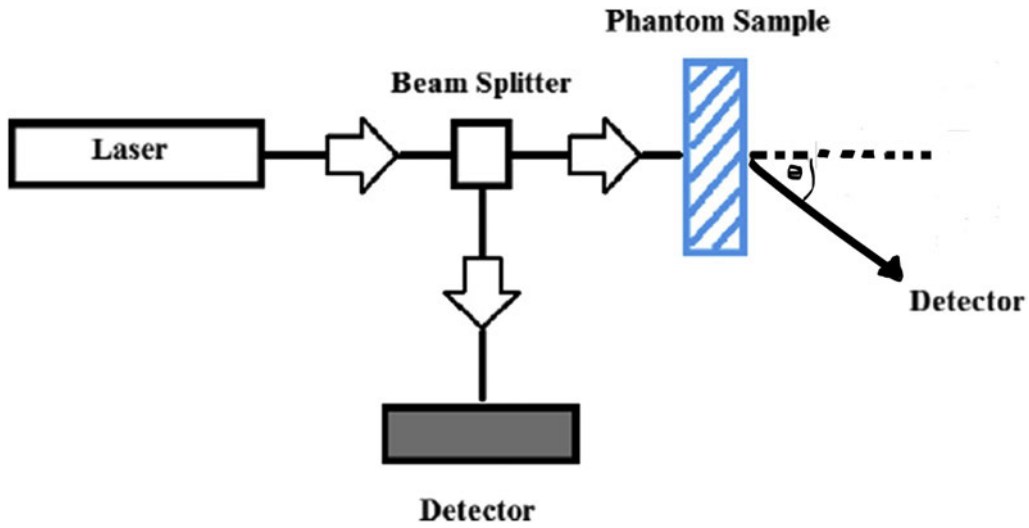


Figure 5.1: Set-up for measurement of optical properties.

### 5.2.2 Measurements of Optical Properties

The red laser wavelength 630 nm was incident on slices of the phantom sample with the beam positioned at a fixed distance (0.4m) away from the sample. The samples were mounted on a slice holder perpendicular ( $0^\circ$  of incidence angles) to the incident light power ( $P_0$ ) with the transmitted power at an angle (Fig. 5.1). A 25 mm diameter cube splitter (Edmund Optics, USA) was used to continuously monitor the incident beam power. Measurements of the laser light power incident and transmitted through each slice were obtained by directly compressing thin samples of the slime phantom of various sizes between two optical glasses ( $n = 1.52$ ) and the actual thickness ( $L$ ) measured using a digital vernier calliper. A drop of saline solution was used to improve the optical contact between the tissue and glass and minimize rough effects for perfect scattering. The powers of the laser source were estimated in mW using an EO 54-018 collimated digital handheld laser power meter with a response time of 2 to 10 ms (Edmund Optics, USA). The singly unscattered light relatives to the normal line was detected by the ray optics technique. The scattering angle was measured using a goniometer since the light is mostly forward scattered (anisotropy scattering) [128]. All measurements were at room temperature.

The total attenuation coefficient ( $\mu_t$ ) was computed from the Lambert-Beer law relation (Eq 5.1), assuming multiple scattering does not occur:

$$\mu_t = -\frac{1}{L} \ln\left[\frac{P}{P_0}\right] \quad (5.1)$$

Where  $L$  is the sample thickness,  $P_0$  is the power of the incident beam and  $P$  is the power of transmitted light.

A graph of  $-\ln[\frac{P}{P_0}]$  against thickness  $L$  was plotted for each phantom-sample tissue and the attenuation coefficient  $\mu_t$  is represented by the slope of the linear fit. In a turbid medium, the attenuation coefficient  $\mu_t$  is also described as the sum of the absorption and scattering coefficients as:

$$\mu_t = \mu_a + \mu_s \quad (5.2)$$

The effective attenuation coefficient ( $\mu_{eff}$ ) and penetration depth ( $\delta$ ) were deduced from the absorption coefficient ( $\mu_a$ ), scattering coefficient ( $\mu_s$ ), and anisotropy ( $g$ ). The anisotropy factor  $g$  was computed using the Henyey-Greenstein (H-G) phase function (Eq. 5.3) valid in the limit of single scattering. Wherein the exit angle dependence of transmitted intensity is expressed as [129]:

$$P(\theta) = K \left[ \frac{1 - g^2}{(1 + g^2 - 2g\cos(\theta))^{\frac{3}{2}}} \right], \quad (5.3)$$

This information allowed for the evaluation of the effective attenuation coefficient with (Equation 5.4)

$$\mu_{eff} = \sqrt{3\mu_a[\mu_a + (1 - g)\mu_s]} \quad (5.4)$$

The reciprocal of the effective attenuation coefficient gives an estimation of the penetration depth:

$$\delta = \frac{1}{\mu_{eff}} \quad (5.5)$$

### 5.3 RESULTS AND DISCUSSION

In this study, PVA slime phantoms were developed to determine the effective attenuation coefficient and optical penetration depth of the 630 nm laser light in grade III malignant brain tumour tissues, as found in the literature. Table 5.1 and 5.2 present the incident and transmitted laser power intensities through different thicknesses of the pure phantom and samples with added absorption. The range of optical thicknesses ( $L$ ) was tested in this experiment, and  $L \leq 3$  mm showed significantly negligible multiple scattering effects. The pure phantom scattered the light beam at small angles ( $<10^\circ$ ) measured with a goniometer. The anisotropy factor ( $g$ ) values computed from Equation 5.3 using Wolfram Mathematica applied only to the pure scattering samples were typical of cancerous tissues for visible light wavelengths [130]. Each value reported is the average of four reaped measurements on each



slice's thickness.

**Table 5.1:** The power intensities of the 630 nm laser through a mixture of 60g/l concentration of borax with 100 ml of PVA slime glue.

$L(\text{mm})$	Incident Power(mW)	Transmitted Power(mW)	$-\ln[\frac{P}{P_0}]$	$\theta(\text{deg})$	$g$
0.53	4.46	3.27	0.311	4	0.993
1.01	4.18	2.83	0.390	4.8	0.989
1.52	4.81	2.39	0.700	6	0.982
2.04	4.94	1.96	0.925	7	0.977
2.50	4.60	1.61	1.051	8	0.973
3.02	4.72	1.19	1.380	9.5	0.966

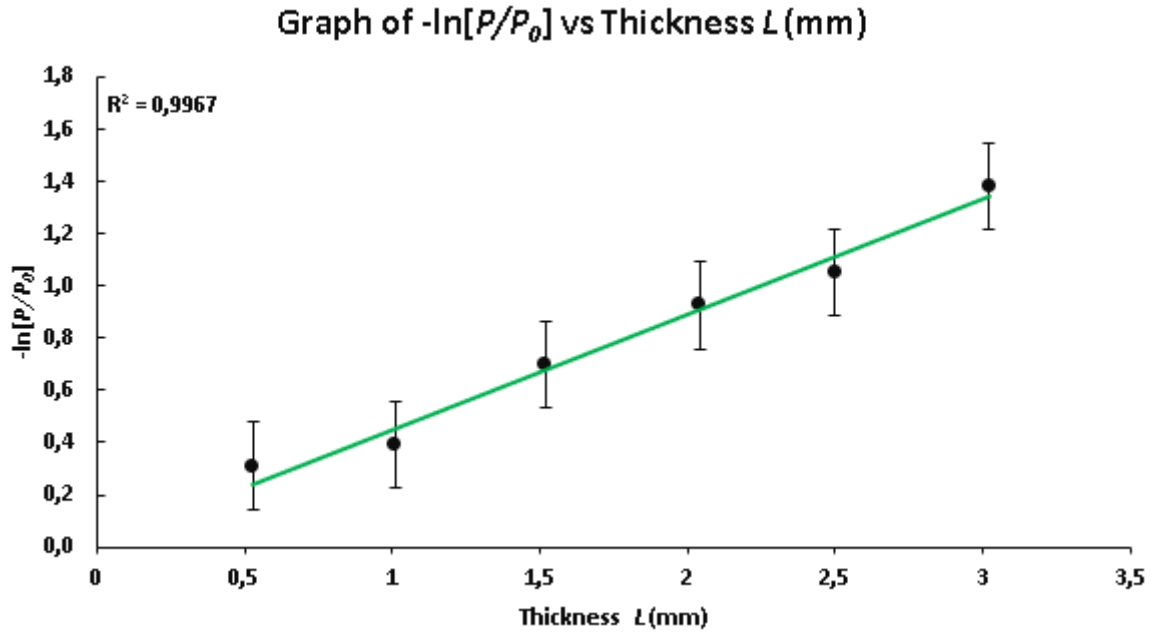


**Figure 5.2:** The logarithmic intensity as a function of thickness with associated linear fitting options to determine the total attenuation coefficient for the pure slime phantom at 630 nm.

**Table 5.2:** The power intensities of the 630 nm laser through the 60g/l concentration of borax with 100 ml of PVA slime glue, and 0.4 ml of India Ink, to assess the effects of adding absorbers on total attenuation coefficients.

$L(\text{mm})$	Incident Power(mW)	Transmitted Power(mW)	$-\ln[\frac{P}{P_0}]$
0.49	4.03	2.89	0.333
1.03	4.21	2.34	0.588
1.52	4.39	1.89	0.830
2.01	4.62	1.40	1.195
2.56	4.58	1.07	1.453
3.11	4.67	0.71	1.888

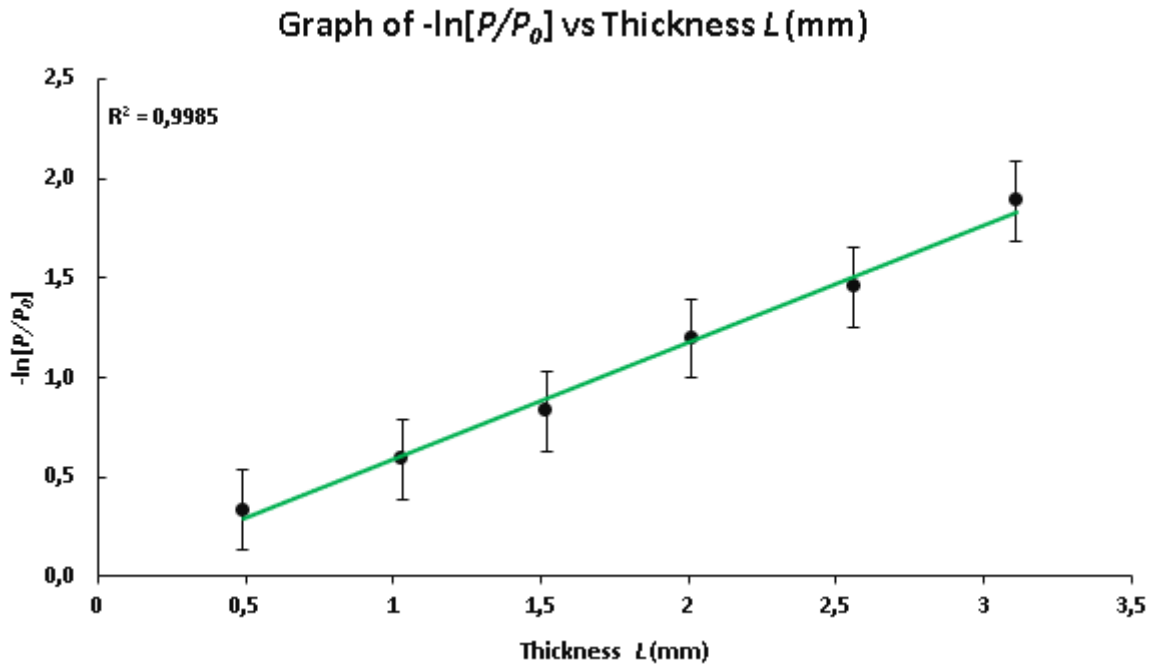


**Figure 5.3:** The logarithmic intensity as a function of thickness with associated linear fitting options to determine the total attenuation coefficient for the slime phantom with absorbers at 630 nm.

Figs. 5.2 and 5.3 shows the graph of  $\ln(\frac{P}{P_0})$  plotted as a function of thickness for all phantom samples with error bar plots showing the standard deviation of uncertainty. The total attenuation coefficient corresponds to the slope of the linear fit. The statistical measure ( $R^2 \approx 1$ ) overall samples indicated a robust correlation between

the values of  $\ln(\frac{P}{P_0})$  and  $L$ . Therefore, increasing the incident intensities with large thicknesses will be an effective way to deliver adequate light to deeper areas of the tumour tissue. The phantom slime material possesses negligible optical absorption properties; hence the assumption:  $\mu_t \approx \mu_s$  was considered for the pure phantom sample and the absorption properties ( $\mu_a$ ) of the ink act additionally to create the  $\mu_t$  of the phantom.

The scattering coefficient ( $\mu_t = 0.445 \text{ mm}^{-1}$ ), anisotropy factor ( $g = 0.980$ ), reduced scattering coefficient ( $\mu'_s = 0.0089 \text{ mm}^{-1}$ ), absorption coefficient ( $\mu_a = 0.142 \text{ mm}^{-1}$ ) were obtained from (Eq. 5.2) considering ( $\mu_t \approx \mu_s$ ) for the pure slime phantom sample. These optical properties allowed for the estimation of the effective attenuation coefficient and penetration depth (Table 5.3)

**Table 5.3:** Comparison of effective attenuation coefficient and penetration depth values in this study with other work at 630 nm.

Brain tumour tissue	$\mu_{eff}(\text{mm}^{-1})$	$\delta$ (mm)
Present study	$0.25 \pm 0.02$	4.00
[131]	0.24	4.17
[132]	0.22 - 0.66	1.52 - 4.55
[133]	0.38 - 0.588	1.7 - 2.6

Despite the relative simplicity of the methodology developed to measure the optical properties with several approaches to minimizing artefacts from this study, the results obtained were comparable to reported values in the literature (Tables 5.3). However, Svaasand et al. [133] found lower penetration depth values compared to this study and that by Wilson et al. [131] and Muller et al. [132], respectively. These observed differences may be due to the varying tissue samples, theoretical models employed and approximations made. The penetration depth was evaluated for five human brains (two neonatal and three adults) immediately after autopsies by Svaasand et al. [133], following interstitial irradiation of the tissues. They concluded that the degree of myelination influences the penetration depth, which increases the scattering of light and reduces the diffusion coefficient. The slight variation in values may also be attributed to changes in the real issues such as blood drainage and deoxygenation with time after resection or alterations in blood flow or oedema caused by irradiation [131]. Moreover, the tissues were probably a mix of both normal brain matter and tumour. Discrepancies among the results may also be from undetectable

multiple scattering in our study. This much impacted the transmitted powers and scattering angles recorded. To satisfy the condition of single scattering, the samples were sliced to significantly small thickness while maintaining rigidity. Besides, the distance between the sample holder and the detector was enough to reduce the scattering effects at optical properties measurements. Generally, the depth of light penetration into normal tissues is considerably less than tumorous tissues. Nevertheless, the ability of light-based techniques like PDT to treat deep-seated pathologies is limited by a significant attenuation in potency as the light penetrates deeper into the tissue [134]. Clinically, the delivery of lights into deeper and complex treatment sites is achieved through thin optical fibers that deliver light and simultaneously act as diagnostic sensors to gauge vital PDT parameters, critically impacting the therapeutic response [134].

## 5.4 CONCLUSION

This study confirms that PVA slime glue-based phantoms with optical properties evaluating the effective attenuation coefficient ( $\mu_{eff}$ ) and penetration depths ( $\delta$ ) of red laser (630 nm) in malignant brain tumours tissues could be fabricated. The repeatability of the recipe was verified and showed the capability to reproduce the desired properties. Undoubtedly, the developed phantoms can be used with further investigations to optimize PDT irradiation procedures and establish accurate light dosimetry for brain tumour treatments.

## ACKNOWLEDGEMENTS

This work was funded from the research allowance given to one of the authors by the University of KwaZulu-Natal, South Africa.

## Chapter 6

# Realistic deformable phantoms with optical properties of human tissues for biomedical research applications

1

---

<sup>1</sup>Lindokuhle Ntombela, Naven Chetty, Bamise Adeleye, 2022. Realistic deformable phantoms with optical properties of human tissues for biomedical research applications. *Result in optics, journal*. (Under review)

---

## Realistic deformable phantoms with optical properties of human tissues for biomedical research applications

Lindokuhle Ntombela<sup>a</sup>, Naven Chetty<sup>a\*</sup>, Bamise Adeleye<sup>a</sup>

<sup>a</sup>School of Physics and Chemistry, University of KwaZulu-Natal,  
Private Bag X01, Scottsville 3209, South Africa

\*Corresponding author : chettyn3@ukzn.ac.za and Tel : +27721295525

### ABSTRACT

A matrix of poly (vinyl alcohol) (PVA) slime phantoms was investigated to replicate the published optical properties of the lung carcinoma, post-menopausal uterus, and brain tumorous tissues at 630nm wavelength. The effective attenuation coefficients ( $\mu_{eff}$ ) and penetration depths of light in the tissue phantoms were deduced from measurements of its optical properties and the anisotropy factor ( $g$ ), obtained using the Henyey-Greenstein (H-G) phase function and Wolfram Mathematica. The mechanical response of the fabricated phantom materials was characterized and found to be flexible and mouldable into shapes and sizes comparable to desired tissue types.

In the context of accuracy and stability, the phantoms were monitored for over two months and managed to preserve their optical properties with inconsiderable changes, possibly due to dehydration. Further data analysis is required to clarify if the optical properties would significantly change for long periods. We conclude that the fabrication of deformable tissue phantoms capable of uniformly incorporating any inserted lesion-like objects with relatively available materials and clear procedure is realizable. These phantoms are promising for testing and calibrating new optical imaging systems and developing disease diagnosis and treatment techniques.

**Keywords:** Lung carcinoma, optical properties, penetration depth, slime materials.

## 6.1 INTRODUCTION

Materials that simulate the optical properties and geometries of real biological tissues are highly demanded and desirable for performance evaluation and validation of new methods and technologies [135]. Such materials, called optical phantoms, mimic the idealized tissue to understand their characteristics and distributions of laser light through them during imaging procedures [136, 137]. Moreover, optical phantoms are invaluable in treating the threats and management of cancer diseases and comparing different cancer photodetection tools in human tissues [138, 139]. Phantoms are an effective alternative to real tissue in the initial test of modalities for diagnosing and treating many cancer types since it allows for systems or human tissue simulation with varying levels of complexity [139, 140].

Several efforts have been devoted to describing the recipes for phantom materials with tissue-equivalent properties under controlled experimental conditions and different imaging technologies [141–143]. For instance, Silicone-based composite phantoms were designed and fabricated to mimic human breast tissue's ultrasonography, mammography, and surgical responses [144]. The performance of two different additives: i) silicone oil and ii) vinyl terminated poly (dimethylsiloxane) (PDMS), were monitored by a homemade acoustic arrangement in the design of the ultrasonography model [144]. A significant challenge in the design was the realization of the acoustic close to that of human tissues. Similarly, Silicone (PDMS) was implemented for phantoms tuned to specific optical properties in the near-infrared spectrum for optical system calibration and performance testing [145]. Though the process was efficient and controllable, silicone is incompatible with organic materials as tissue constituents. Consequently, a material system to which cellular components may be added is readily employed [142].

Gelatin-Agar phantoms have been used for their accessibility, excellent optical and chemical properties, and mechanical properties [138]. These gelatinous phantoms can be easily machined and moulded into different shapes with a conventional cutter [138, 146]. However, there are several fundamental issues with Agar gel phantoms. The properties are often subject to random variability due to irregularities in several parameters controlled during phantom creation [146]. They dehydrate rapidly and have short durability of about a week, making them unsuitable for some applications [139, 142]. Epoxy resin-based optical phantoms have also been used extensively [147, 148], but they are much stiffer than soft tissue, limiting their applicability [142].

although values of elasticity properties of materials are reported, little attention has been given to the degree to which elastography phantom materials also This study

explores the potential of slime as a suitable base material for fabricating phantoms with reproducible and stable optical and mechanical properties as different human tissues. Slime is a viscous material generated by mixing solutions of polyvinyl alcohol (PVA) and sodium tetraborate decahydrate (Known as Borax) [135]. The polyvinyl alcohol (PVA) slime-based phantoms have long-term optical stability and greater shaping flexibility without distortion to their structural integrity [149]. Their optical properties are controlled by adding appropriate quantities of scattering (e.g., aluminium oxide ( $\text{Al}_2\text{O}_3$ ), titanium dioxide ( $\text{TiO}_2$ ), or polystyrene microspheres) and absorbing materials as water-soluble dye or ink [135].

To our knowledge, limited studies have been conducted on tissue-equivalent slime phantoms. Hebden et al [135] developed a recipe of highly compressible and deformable slime phantoms with excellent tissue-like optical properties for diffuse optical tomography. Yusoff et al [149] investigated the homogeneity and stability of the PVA slime phantom and its suitability as a magnetic resonance imaging (MRI) phantom. The results were promising as the measured T1 and T2 values were stable over time and comparable to various soft tissues. Sha [150] also tested the slime material's suitability to develop a phantom material able to change its shape automatically to simulate the different morphologies of breast imaging in the prone and supine positions.

In this work, a functional but cheap method of fabricating tissues-like slime phantoms with optical properties such as lung carcinoma, post-menopausal uterus, and malignant brain tumour tissues at 630nm was presented. Although values of optical properties are reported for varying phantom materials at this wavelength, we consider this a novel study with polyvinyl alcohol (PVA) slime as the primary medium. The development of tissue-mimicking phantoms that can be compressed and moulded to a similar shape and size as real organs/tissues are crucial for disease diagnosis and treatment processes such as Photodynamic Therapy (PDT) of cancerous tissues and in the introduction of new imaging techniques.



## 6.2 Experimental procedure

### 6.2.1 Phantoms materials

Since the PVA polymer does not dissolve easily and to ensure the slime material's consistency, a PVA glue solution was obtained from local providers at Port Elizabeth, EC, 6025, South Africa. Borax powder (sodium tetraborate decahydrate)  $[\text{Na}_2\text{B}_4\text{O}_7 \cdot 10\text{H}_2\text{O}]$  was purchased from Allied drug company, South Africa. The desired optical properties of the phantom were reached by adding appropriate quantities of aluminium oxide ( $\text{Al}_2\text{O}_3$ ) (64271, Darmstadt, Germany) as the scattering agent and India ink (PRO-4100, Pro Art) as the absorbing agent.

#### Phantom Fabrication

- Different amounts (1.5 g and 3 g) of borax powders determined using a digital balance (readability of 0.01 g) were added separately into beakers containing 50 ml of deionized water. The mixture was then heated and stirred vigorously using a magnetic stirrer until the solution reached a temperature of approximately 70°C and all the powder granules were dissolved.
- This resulted in concentrations of 30g/L and 60g/L. The appearance was crystal-clear, indicating the solution was homogenous distribution at this temperature.
- 100 ml of PVA glue solution was prepared in a second beaker while the borax solution was allowed to cool to about 20°C.
- To ensure uniform mixing within the slime material, suitable amounts of optical agents (Absorbing and Scattering) to simulate the optical properties of the targeted tissues at the imaging wavelength(s) were added to the borax solution before combining the two solutions.
- The borax solution was gradually added to the 100 ml PVA glue solution using a syringe while the mixture was gently stirred until the slimes produced were uniform.
- The samples are poured into convenient moulds with specific geometry while carefully removing any bubbles or disturbance.
- Finally, the slime phantom was wrapped with foil and placed overnight in a refrigerator to allow for full cross-link and prevent extreme changes in temperature and humidity.

The sample temperature was monitored using a Techgear TG732TK dual channel digital thermometer adapted to utilize a thermocouple attached on the reverse side

of a Velcro strap. The digital thermocouple provides accurate temperature measurements of the heated solution on the accuracy of  $\pm 5^\circ\text{C}$ . Table 6.1 summarizes the quantities of significant materials for phantom fabrication.

**Table 6.1:** PVA Slime phantom recipes with tissue at different wavelengths.

Mimicked tissue	PVA slime glue (ml)	Borax (g/l)	$\text{Al}_2\text{O}_3$ (g)	India Ink (ml)	$\lambda$ (nm)
Lung Carcinoma	100	30		0.6	630
Post-menopausal Uterus	100	30	0.4	0.4	630
Malignant Brain Tumor	100	60		0.4	630

### 6.2.2 Measurements of Optical Properties

The experimental setup to characterize the optical properties of the fabricated phantom tissues is shown in Figure 6.1.

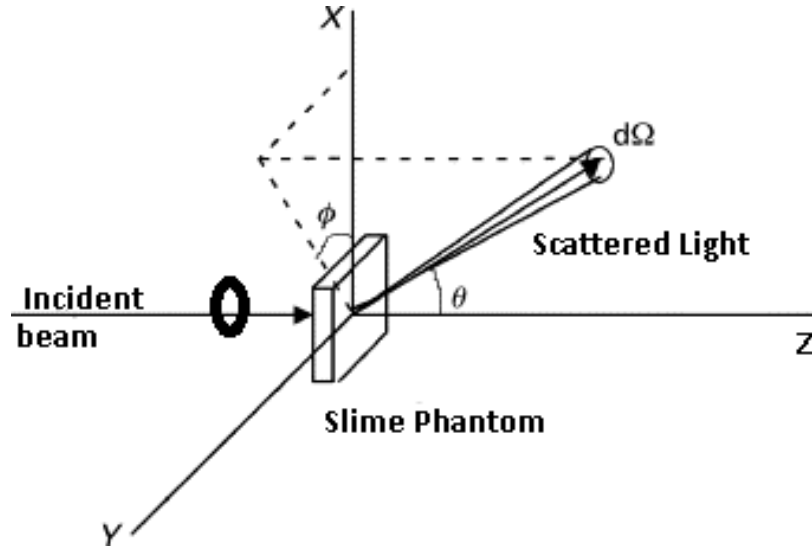


**Figure 6.1:** Schematic illustration of the procedure involved in laser irradiation of phantom slime samples.

A red He-Ne laser source emitting at 630 nm was incident on slices of the phantom of a thickness ( $L$ ) mounted on a slice holder perpendicular to the incident light power ( $P_0$ ) with the scattered light power at angles (range between  $0 - 90^\circ$ ) as shown in Fig 6.1. The incident beam was first passed through a 25 mm diameter cube splitter (Edmund Optics, USA) to monitor the power before illuminating the sample.

The light through the sliced sample is scattered into an elemental solid angle  $d\Omega$  in direction  $(\theta, \phi)$  and was detected in (mW) using an EO 54 - 018 digital handheld laser power meter (Edmund Optics, USA) with aperture size 8 mm, positioned a considerable distance from the sample. The slime phantom was squeezed between two optical glasses to obtain slices of suitable thickness determined using an LCD 150mm electronic digital vernier callipers. With a drop of 0.9 % saline solution, the optical contact between the slime phantom and glass was improved for perfect scattering. The ray optics technique detected the single scattered light relative to the normal line, and the scattering angle was estimated using a goniometer. The optical behaviour of the phantoms is characterized by the scattering coefficient ( $\mu_s$ ), absorption coefficient ( $\mu_a$ ), anisotropy factor ( $g$ ), and the penetration depth ( $\delta$ ). The scattering and absorption coefficients were deduced from the total attenuation coefficient ( $\mu_t$ ) applying the Lambert-Beer law relation (Equation 6.1) and (Equation 6.2) and minimizing multiple scattering effects [151]:

$$\mu_t = -\frac{1}{L} \ln\left[\frac{P}{P_0}\right] \quad (6.1)$$

$$\mu_t = \mu_a + \mu_s \quad (6.2)$$

Where  $L$  is the sample thickness,  $P_0$  is the power of the incident beam and  $P$  is the power of transmitted light.

The slime phantom material possesses negligible absorption properties, hence the assumption that  $\mu_t \approx \mu_s$  was considered for the pure sample. The anisotropy factor ( $g$ ) was computed using the Henyey-Greenstein (H-G) phase function with Wolfram Mathematica valid in the limit of single scattering where the exit angle dependence of transmitted intensity is expressed as Equation 6.3 and  $\theta$  the mean scattering angle [152].

$$P(\theta) = K \left[ \frac{1 - g^2}{(1 + g^2 - 2g\cos(\theta))^{\frac{3}{2}}} \right], \quad (6.3)$$

This information allowed for the evaluation of the effective attenuation coefficient ( $\mu_{eff}$ ) with Equation 6.4 and its inverse value, the penetration depth ( $\delta$ ) is represented in Equation 6.5.

$$\mu_{eff} = \sqrt{3\mu_a[\mu_a + (1 - g)\mu_s]} \quad (6.4)$$

$$\delta = \frac{1}{\mu_{eff}} \quad (6.5)$$

### 6.3 Results and discussion

The suitability of polyvinyl alcohol (PVA) slimes as an enabling material to create optical phantoms that mimic the optical properties and are shapeable to a healthy and diseased biological tissue under various imaging modalities was investigated. Phantoms with similar and controllable optical properties as lung carcinoma, post-menopausal uterus, and cancerous brain tissues were successfully fabricated. Tables 6.2-6.4 give the power of the incident and transmitted laser light through thicknesses of each phantom type. Each data reported is the mean of the four repeated measurements on each slice's thickness. The range of optical thicknesses ( $L$ ) and concentration of  $\text{Al}_2\text{O}_3$  was tested in this study, and  $L \leq 3$  mm showed significantly minor multiple scattering effects. The scattering angle increases with the thickness of the slime phantom sample as the number of particles increases, in agreement with Rutherford's scattering explanation.

The linear attenuation coefficient ( $\mu_t$ ) for all phantom types is represented by the slope of the linear curve on  $\ln(\frac{P}{P_0})$  against thickness ( $L$ ) graph (Figures 6.2-6.4).  $R^2 \approx 1$  is the correlation coefficient with the error bars indicating the degree of uncertainty for each phantom thickness.

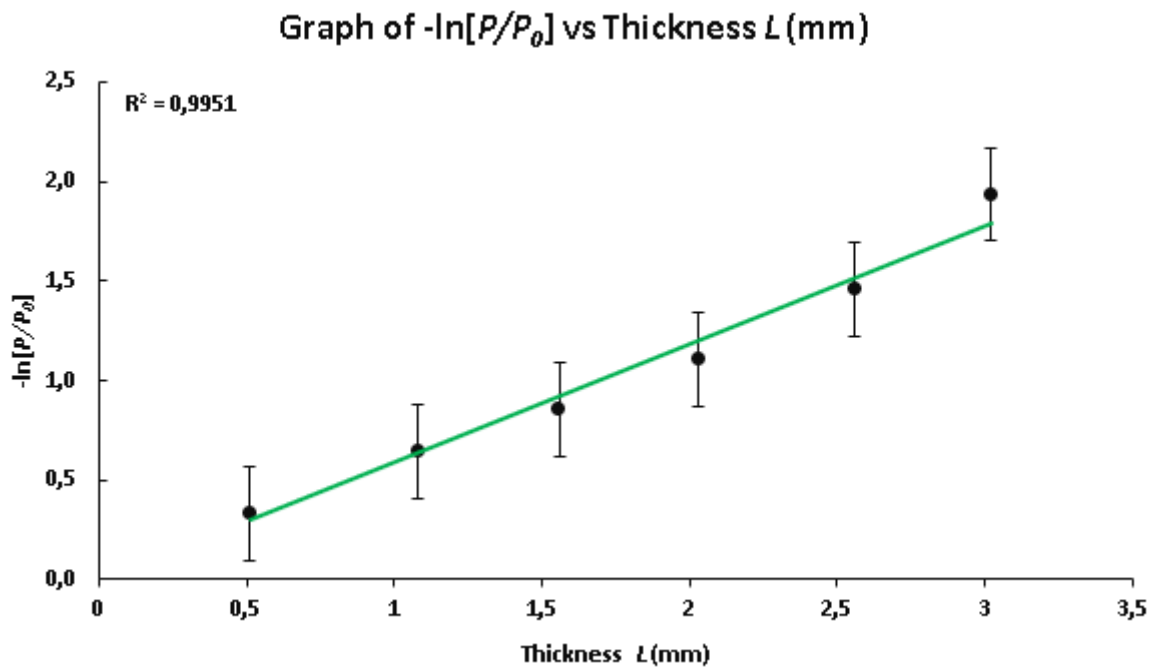
The optical coefficients are evaluated based on the hypothesis that the absorption coefficient ( $\mu_a$ ) of the India ink and the scattering coefficient ( $\mu_s$ ) of the slime glue act additionally to create the total attenuation coefficient ( $\mu_t$ ) of the phantom tissues are presented in Table 6.5. The anisotropy factor ( $g$ ) was the average of the six values computed by Equation 6.3 using Wolfram Mathematica applicable in the pure and scattering samples. Furthermore,  $g$  ranges from -1 to 1, and as  $g$  approaches 1, the distribution peaks in the forward direction. The presented values were obtained from a series of measurements performed within several months, aided by the quantitative information on desired tissues in literature (Table 6.6). Possible variations might be indicative of the difficulties in accurately determining these coefficients, such as the complex nature of biological tissues, the number of samples available, age, and the direction and method of measurements [153–155]. This latter factor often limits the number of optical coefficients to be determined, and so many studies only report the penetration depth or effective attenuation coefficient value. Additionally, it is noted that marked changes occur, even when such obvious factors are missing [155].

To investigate the deformable capability of the fabricated phantoms and the stability of their optical properties over a period, they were assembled and filled within a latex shell mould with geometric features of desired tissues. The shell mould consisted of four layers of liquid latex (Mouldmaster, House of Handicrafts, Braintree, England) brushed on convenient models, avoiding the formation of bubbles [135].

The phantom slime materials contained in the latex moulds were covered with a glass plate for a straight surface removed after some minutes. The moulds were then sealed with a latex patch. The optical properties of the phantoms were monitored over two months and found to be consistent with possible dehydration-related changes.

**Table 6.2:** The power intensities through different thicknesses of the lung carcinoma slime phantom.

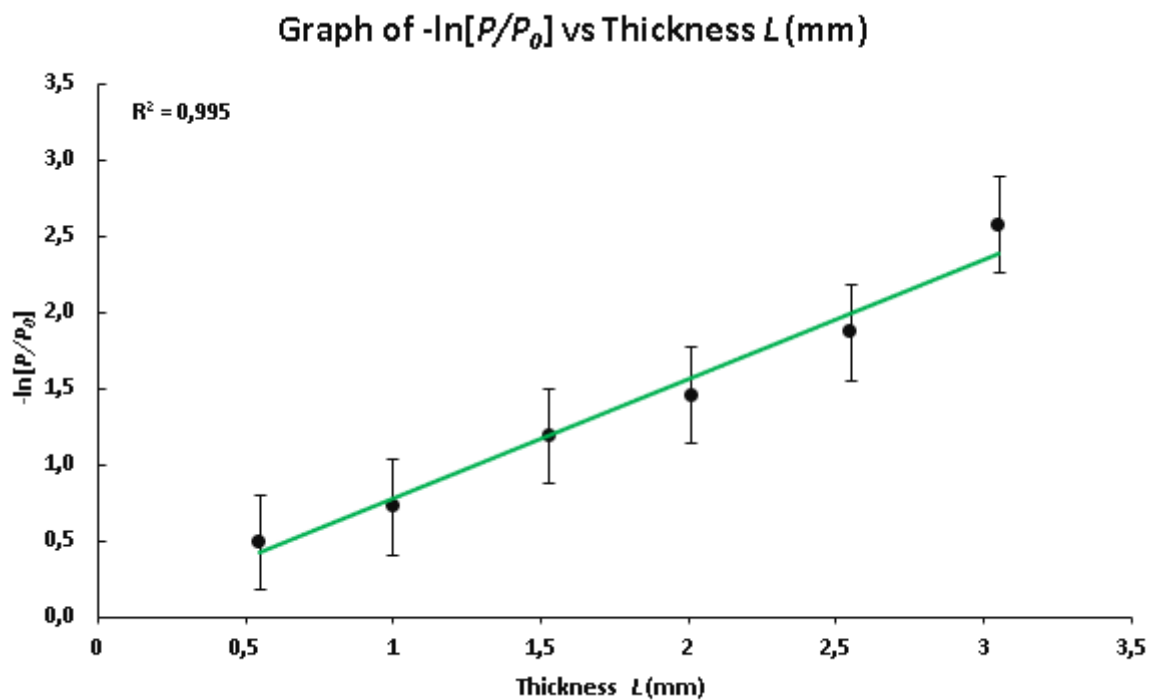
$L(\text{mm})$	Incident Power(mW)	Transmitted Power(mW)	$-\ln\left[\frac{P}{P_0}\right]$	$\theta(\text{deg})$	$g$
0.51	4.30	3.08	0.334	1.5	0.999
1.08	4.95	2.60	0.644	4	0.992
1.56	4.99	2.13	0.852	5.25	0.986
2.03	5.00	1.66	1.104	6.5	0.973
2.56	4.88	1.14	1.456	7	0.973
3.02	4.97	0.72	1.935	7.5	0.972



**Figure 6.2:** The logarithmic intensity as a function of thickness to determine the total attenuation coefficient for lung carcinoma slime phantom.

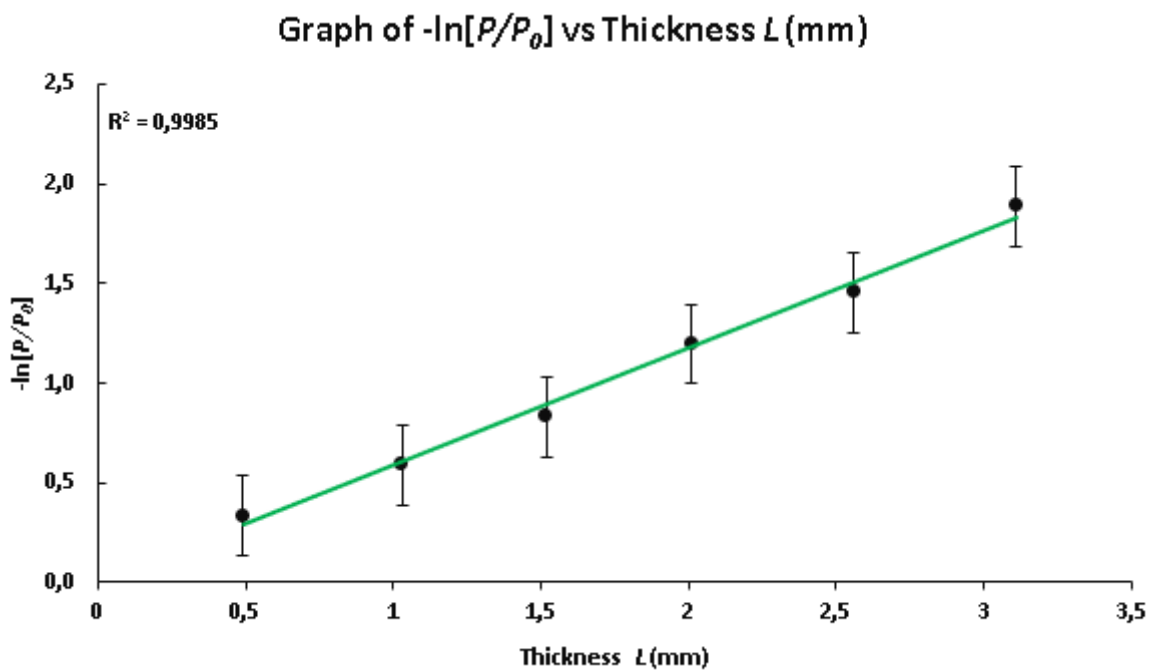
**Table 6.3:** The power intensities through different thicknesses of the post-menopausal uterus slime phantom.

$L(\text{mm})$	Incident Power(mW)	Transmitted Power(mW)	$-\ln[\frac{P}{P_0}]$	$\theta(\text{deg})$	$g$
0.55	4.04	2.48	0.488	5.5	0.985
1.00	4.05	1.97	0.721	6	0.982
1.53	5.11	1.56	1.188	7	0.977
2.01	5.01	1.17	1.456	9	0.957
2.55	5.10	0.79	1.868	9	0.969
3.05	5.09	0.39	2.576	10	0.972

**Figure 6.3:** Graph of logarithmic intensity data as a function of thickness to determine the total attenuation coefficient for the post-menopausal uterus slime phantom.

**Table 6.4:** The power intensities through different thicknesses of the brain tumour slime phantom.

$L(\text{mm})$	Incident Power(mW)	Transmitted Power(mW)	$-\ln[\frac{P}{P_0}]$	$\theta(\text{deg})$	$g$
0.49	4.03	2.89	0.333	4	0.993
1.03	4.21	2.34	0.588	4.8	0.982
1.52	4.39	1.89	0.830	6	0.982
2.01	4.62	1.40	1.195	7	0.977
2.56	4.58	1.07	1.453	8	0.973
3.11	4.67	0.71	1.888	9.5	0.966

**Figure 6.4:** Graph of logarithmic intensity data as a function of thickness to determine the total attenuation coefficient for brain tumour slime.

**Table 6.5:** Optical coefficients of fabricated tissues at 630 nm from this study

Fabricated tissues	$\mu_a$ (mm <sup>-1</sup> )	$\mu_s$ (mm <sup>-1</sup> )	$\mu'_s$ (mm <sup>-1</sup> )	$\mu_{eff}$ (mm <sup>-1</sup> )	$\delta$ (mm)
Lung Carcinoma	$0.334 \pm 0.004$	$0.258 \pm 0.005$	$0.0049 \pm 0.0009$	0.582	1.718
Post-menopausal Uterus	$0.210 \pm 0.001$	$0.572 \pm 0.165$	$0.0149 \pm 0.0004$	0.376	2.66
Malignant Brain tumour	$0.142 \pm 0.002$	$0.445 \pm 0.001$	$0.0089 \pm 0.0002$	0.254	3.94

**Table 6.6:** Optical properties reported for fabricated tissues in Literature at 630 nm.

Fabricated tissues	$\mu_a$ (mm <sup>-1</sup> )	$\mu_s$ (mm <sup>-1</sup> )	$\mu'_s$ (mm <sup>-1</sup> )	$\mu_{eff}$ (mm <sup>-1</sup> )	$\delta$ (mm)	[Ref]
Lung Carcinoma				0.546 - 0.654	1.53 - 1.83	[152, 153]
Post-menopausal Uterus	$0.0515 \pm 0.54$	$0.91 \pm 0.17$		0.351 - 0.429	2.33 - 2.85	[154]
Malignant Brain tumour				0.219 - 0.370	2.70 - 4.55	[156]

## 6.4 CONCLUSION

We have outlined the possibility of creating a reliable tissue-mimicking material with controllable deformable properties using a cost-effective and easy-to-follow procedure. The method was based on polyvinyl alcohol (PVA) slime materials with direct comparison to the lung carcinoma, post-menopausal uterus, and malignant brain tumour tissue's optical coefficients found in the literature at selected wavelengths.

For our experiments, we did not consider oxygenation, blood content, the stage of the menstrual cycle (for the uterus) with morphological and structural changes, and other tissue conditions but focused on simulating the optical tissue properties. Nevertheless, the selected phantom matrix and procedure provide the flexibility to include significant healthy and cancerous tissue features.

Further measurements are required to understand better the durability and the difference between the tissue types with increasing deformation to aid their use in op-



tical imaging research and applications. There are limited probable sources of errors in this study. First, the optical properties of the tissue-like phantom were determined using the additive law of optical coefficients. The accuracy of the law has been tested by comparison with experimentally predicted optical coefficients, with less than a 5% difference [157]. Second is the rough estimation of scattering angle and unseen multiple lights scattering. The sample was sliced to a significantly small thickness while maintaining rigid slices to satisfy the condition of single scattering. Moreover, our experimental setup used an optical collimator to limit the field of view and prevent most scattered light from reaching the power meter (detectors). Lastly, the slime phantoms of arbitrary size and shape were generated within a latex shell. However, the optical property of the latex is reported to have a negligible influence on phantom sample measurements [135].

### **Declaration of Competing Interest**

The authors declare no conflict of interest.

### **ACKNOWLEDGEMENTS**

This work was financially supported through a research allowance from the corresponding author by the University of KwaZulu-Natal.

## Chapter 7

# Conclusion and Future work

This study successfully developed realistic phantom tissues using PVA slime with optical properties similar to human tissues. The in-expensive experimental design and repeatability make it an efficient method for determining phantom tissues' optical properties. The set-up was extended to measure the phase function on thin slices and determine the anisotropy factor. The scattering function of the simulated slime phantoms showed a strong forward peak, indicating anisotropy scattering as actual human tissues. This created the possibility of predicting various optical properties of medical and clinical interest. The predicted optical parameters (absorption and scattering coefficient, effective attenuation coefficient, and penetration depth) were stable and comparable to the human brain, lung carcinoma, post-menopausal uterus, and malignant brain tumour at laser wavelengths of 532 nm and 630 nm.

Furthermore, the created slime phantoms were flexible to the actual human tissues' anatomical shape. Tissue phantoms with relative ease of creation and a high degree of spatial homogeneity and reproducibility are efficient and reliable in developing non-invasive models for light propagation.

The dependence of India Ink and aluminium oxide on optical absorption and scattering were also quantified. Accurate tissue-mimicking phantoms were created by carefully adjusting the concentrations of the absorption and scattering agents. Using microspheres (with well-defined size distributions) as scatterers can likely improve the scattering effects. However, due to the expensive nature of these particles, we highly recommend the aluminium oxide particles since they match the transport scattering coefficients appropriately. Moreover, thinner tissue slices limit multiple scattering effects.

The recipe presented enables simple and safe reproducibility of anatomically realis-

---

tic phantoms useful for laser-based applications. Furthermore, these new phantoms will provide very valuable information for correct dosimetry and the timely understanding of biological effects in imaging systems.

This low-cost bio-mimic material would also be ideal for training and practical purposes specifically in medical education allowing for a detailed explanation of the steps required in a medical procedure.

Further studies, to verify the compatibility and effectiveness of the fabricated phantom models across multiple imaging modalities in a real clinical setting will be evaluated. Additionally, investigating the optical properties of slime phantoms over a broad range of wavelengths computationally and with a measuring device such as a Digital Camera would be an excellent extension for this study. This would help to demonstrate the optimal wavelength range for therapeutic and diagnostic light applications. Further research is also required to take advantage of the proposed phantoms as a helpful tool for cancer imaging by introducing cancer cells to phantom samples.

# References

- [1] R. Srinivasan, D. Kumar, and Megha Singh. Optical tissue-equivalent phantoms for medical imaging. 15(2):pp 42–47.
- [2] Ruikang K Wang, Jeremy C Hebden, and Valery V Tuchin. Recent developments in biomedical optics. *Phy.Med.Biol*, (49), 2004.
- [3] Gambhir SS. Molecular imaging of cancer with positron emission tomography. *Nature Reviews Cancer*, 2(11):pp.683–693, 2002.
- [4] Ametamey SM, Honer M., and Schubiger PA. Molecular imaging with pet. *Chemical reviews*, 108(5):pp.1501–16, 2008.
- [5] Silvestri GA, Gould MK, Margolis ML, Tanoue LT, McCrory D, Toloza E, and Detterbeck F. Noninvasive staging of non-small cell lung cancer. *ACCP evidenced-based clinical practice guidelines*. *Chest*, 132(3):pp.178s–201s, 2007.
- [6] Ghosh S, Soni J, and Purwar H. Differing self-similarity in light scattering spectra: A potential tool for pre-cancer detection. *Optical Society of America*, (1), 2011.
- [7] Rubin D.L, Greenspan H, and Brinkley J.F. Biomedical imaging informatics. *In Biomedical Informatics*, pages pp. 285–327, 2014.
- [8] Chen Chen, Florian Klampfl, Christian Knipfer, Max Riemann, Rajesh Kanawade, Florian Stelzle, and Michael Schmidt. Preparation of a skin equivalent phantom with interior micro-scale vessel structures for optical imaging experiments. (1).
- [9] M. Firbank and D. T. Delpy. A design for a stable and reproducible phantom for use in near infra-red imaging and spectroscopy. 38(6):847.
- [10] B. W. Pogue and M. S. Patterson. Review of tissue simulating phantoms for optical spectroscopy, imaging and dosimetry. 11(4):041102.

- 
- [11] Frederick Ayers, Alex Grant, Danny Kuo, David J. Cuccia, and Anthony J. Durkin. Laser microbeam, medical program, beckman laser institute, university of ca, irvine modulated imaging, inc., aliso viejo, ca, and beckman laser institute photonic incubator. fabrication and characterization of silicone-based tissue phantoms with tunable optical properties in the visible and near infrared domain. page 6870:687007.
  - [12] Alexander V. Bykov Valery V. Tuchin Malgorzata Jedrzejewska-Szczerska1 Maciej S. Wrobel, 1 Alexey P. Popov. Nanoparticle-free tissue-mimicking phantoms with intrinsic scattering. *BIOMEDICAL OPTICS EXPRESS* 2088, 7(6), 2016.
  - [13] A. V. Priezzhev A. V. Bykov, A. P. Popov and R. Myllyla. Multilayer tissue phantoms with embedded capillary system for oct and doct imaging. *Proc. SPIE*, 2011.
  - [14] D. Fixler and R. Ankr. Subcutaneous gold nanorods [corrected] detection with diffusion reflection measurement. *J. Biomed. Opt*, 18(6):061226, 2013.
  - [15] Vardaki M.Z and Kourkoulis N. Tissue phantoms for biomedical applications in raman spectroscopy: A review. *Biomedical engineering and computational biology*, 11, 2020.
  - [16] H. ed. Jelinkova. Lasers for medical applications: diagnostics, therapy and surgery. elsevier. *Journal of Biomedical Optics*, 2013.
  - [17] H Kato and T Ishida. Development of an agar phantom adaptable for simulation of various tissues in the range 5-40 mhz.(hyperthermia treatment of cancer). *Phys. Med. Biol*, 22(221), 1987.
  - [18] Matthieu Zellweger Nora Utke ' Daniel Braichotte Jean-Pierre Ballini Hubert van den Bergh Georges Wagnieres, Shangguan Cheng. An optical phantom with tissue-like properties in the visible for use in pdt and fluorescence spectroscopy. *Phys. Med. Biol*, 42, 1997.
  - [19] Paola Taroni Alessandro Torricella Rinaldo Cudeddu, Antonio Pifferi and Gianluca Valentini. A solid tissue phantom for photon migration studies. *Phys Med. Biol*, 42:1971–1979, 1997.
  - [20] Pascal F. Chapon Peter J. Milne Sergio G. Mendoza Dvid B. Denham Jean Marie A. Parel David S. Rpbinson M.D Nelson Salas Jr, Fabrice Manns. Development of a tissue phantom for experimental studies on laser interstitial thermotherapy of breast cancer. *Biomedical Optics*, 3907, 2000.

- 
- [21] Bruno Farina Stefano Tmatis Manuela Lualdi, Antonio Colombo. Aphantom with tissue-like optical properties in the visible and near infrared for use in photomedicine. *Lasers in Surgery and Medicine*, 28(3):237–43, 2001.
  - [22] Gibson A. P Hebden J. C, Price B. D and Royle G. A soft defromable tissue-equivalent phantom for diffuse optical tomography. *Physics in Medicine and Biology*, 51(21):p.5581, 2006.
  - [23] Beer S. Maeder U. Burg J.M. Schlupp P. Schmidts T. Runkel F. Bergmann, T. and M Fiebich. Development of a skin phantom of the epidermis and evaluation by using fluorescence techniques. In *Optical Diagnostics and Sensing XI: Toward Point-of-Care Diagnostics; and Design and Performance Validation of Phantoms Used in Conjunction with Optical Measurement of Tissue III*, Vol. 7906:pp. 125–133, 2011, February.
  - [24] Z.G. Portakal, J.W. Phillips, S.M. Shermer, C.E. Richards, E. Spezi, L.J. Garcia, T. Perrett, D.G. Lewis, and N. Tuncel. Creating a tissue mimicking phantom appropriate for relaxometry, diffusion imaging and ultrasound elastography. *Abstracts / Physica Medica*, 32:196–221, 2016.
  - [25] A.N. Yusoff, A. Z. Ding1, N. Azman1, M. N. A. Awang, and H. Abdul Manan. Homogeneity and stability of poly (vinyl alcohol) slime phantom with different borax concentration. *Solid State Science and Technology*, 27(1 and 2):51–67, 2019.
  - [26] Baxter GD. Therapeutic lasers: Theory and practice. edinburgh: Churchill livingstone. April 4, 1994.
  - [27] Z Luksiene. Photodynamic therapy: mechanism of action and ways to improve the efficiency of treatment. *Medicina*, 39(12):pp.1137–1150, 2003.
  - [28] Abergel RP, Lyons RF, White RA, Lask G, Matsuoka LY, Dwyer RM, and Uitto J. Skin closure by nd:yag laser welding. 1968.
  - [29] B.P. Chan. Biomedical applications of photochemistry. *International Society for Optics and Photonics*, 16(5):pp.509–522.
  - [30] J Hecht. Understanding lasers: an entry-level guide. *John Wiley and Sons*, 2018.
  - [31] Jephias Gwamuri1, Prof. Ashok V Gholap, Dr Tahani S Mohamed Shartir, and Prof Paul K Bauh-Bassuah. Investigating light propagation in turbid media by evaluating optical properties of phantom tissues. 2014.
  - [32] B. Cem Sener. Biomedical optics and lasers. *Department of Oral and Maxillofacial Surgery Faculty of Dentistry, Marmara University, Istanbul, Turkey*, 2015.

- 
- [33] H elinkova. Lasers for medical applications: diagnostics, therapy and surgery. elsevier. 2013.
- [34] C.Scolaro M.Cutroneo, L.Torrisi. Laser applications in biomedical field.
- [35] T.J Dougherty, C.T. Gomer, and B.M. Henderson et a. Photodynamic therapy. *JNatl Cancer Inst*, 90(12):pp.889– 9, 1998.
- [36] Julia L. Sandell and Timothy C. Zhu. A review of in-vivo optical properties of human tissues and its impact on pdt. *J. Biophotonics*, 4((11-12)):773–787, 2011.
- [37] Calzavara-Pinton PG, Venturini M, and Sala R. Photodynamic therapy: update 2006. part 1: Photochemistry and photobiology. *j eur acad dermatol venereol*, 21:293–302, 2007.
- [38] Qiang YG, Zhang XP, Li J, and Huang Z. Photodynamic therapy for malignant and non-malignant diseases: clinical investigation and application. *Chin Med J (Engl)*, 20(119):845–57, 2006.
- [39] L.F. de Freitas and M.R. Hamblin. Proposed mechanisms of photobiomodulation or low-level light therapy. *IEEE Journal of selected topics in quantum electronics*, 22(3):pp.348–364, 2016.
- [40] Bleier BS, Cohen NA, Chiu AG, O'Malley BW Jr, Doghramji L, and Palmer JN. Endonasal laser tissue welding: first human experience. *am j rhinol allergy*. 24(3):244–6, 2010.
- [41] Esposito G, Rossi F, Matteini P, Puca A, Albanese A, Sabatino G, Maira G, and Pini R. Present status and new perspectives in laser welding of vascular tissues. *J Biol Regul Homeost Agents*, 25(2):145–52, 2011.
- [42] Bloom JD, Bleier BS, Goldstein SA, Carniol PJ, Palmer JN, and Cohen NA. Laser facial nerve welding in a rabbit model. *arch facial plast surg*. 14(1):52–8, 2011.
- [43] Youssef TF, Ahmed MR, and Kassab AN. Utilization of co(2) laser for temporal fascia graft welding in myringoplasty: an experimental study on guinea pigs. *ORL J Otorhinolaryngol Relat Spec*, 72(2):119–23, 2011.
- [44] Hu L, Lu Z, Wang B, Cao J, Ma X, Tian Z, Gao Z, Qin L, Wu X, Liu Y, and Wang L. Closure of skin incisions by laser-welding with a combination of two near-infrared diode lasers: preliminary study for determination of optimal parameters. *J Biomed Opt*, 16(3):038001, 2011.

- 
- [45] Xia SJ. Two-micron (thulium) laser resection of the prostate-tangerine technique: a new method for bph treatment. *Asian J Androl*, 11(3):277–81, 2009.
- [46] Ryu SW, Lee SH, and Yoon HJ. A comparative histological and immunohistochemical study of wound healing following incision with a scalpel, co(2) laser or er:cr:ysgg laser in the guinea pig oral mucosa. *Acta Odontol Scand*, 11(3):277–81, 2011.
- [47] Nubile M, Carpineto P, Lanzini M, Calienno R, Agnifili L, Ciancaglini M, and Mastropasqua L. Femtosecond laser arcuate keratotomy for the correction of high astigmatism after keratoplasty. *Ophthalmology*, 116(6):1083–92, 2009.
- [48] Yang SS, Hsieh CH, Lee YS, and Chang SJ. Diode laser (980 nm) enucleation of the prostate: a promising alternative to transurethral resection of the prostate. *Lasers Med Sci*, 116(6):1083–92, 2012.
- [49] Saccomandi P, Schena E, Di Matteo FM, Pandolfi M, Martino M, Rea R, and Silvestri S. Laser interstitial thermotherapy for pancreatic tumor ablation: Theoretical model and experimental validation. *Conf Proc IEEE Eng Med Biol Soc*, pages 5585–8, 2011.
- [50] Yang SS, Hsieh CH, and Lee YS. Chang sj (2012) diode laser (980 nm) enucleation of the prostate: a promising alternative to transurethral resection of the prostate. *Lasers Med Sci*, 2012.
- [51] Lee JC, Kim JW, Lee YJ, Lee SR, Park CR, and Jung JP. Surgical management of auricular infantile hemangiomas. *Korean J Thorac Cardiovasc Surg*, 44(4):311–3, 2011.
- [52] Hochman M, Adams DM, and Reeves TD. Current knowledge and management of vascular anomalies: I. hemangiomas. *Arch Facial Plast Surg*, 13(3):145–51, 2011.
- [53] B.C. Wilson. Measurement of tissue optical properties: methods and theories. In *Optical-thermal response of laser-irradiated tissue*. Springer, Boston, MA, page 233–303, 1995.
- [54] G.R. Bergman. Evaluation of exposure to optical radiation used in diagnostic and treatment in medicine and dentistry. 2004.
- [55] V.V. Tuchin. Tissue optics and photonics: light-tissue interaction. *Biomedical Photonics and Engineering*, 1(2), 2015.
- [56] D.H. Sliney and B.C Freasier. Evaluation of optical radiation hazards. *Applied Optics*, 12(1):1–24, 1973.



- 
- [57] Zora Gajinov, Milan MATIC, Sonja PRCIC, and Verica DURAN. Optical properties of the human skin. *Serbian Journal of Dermatology and Venereology*, 2(4):131–136, 2010.
- [58] Mie G. Beitrage zur optik truber medien speziell kolloidaler metallosungen. *Ann Phys.*, 25:pp377–445, 1908.
- [59] M. Firbank. The design, calibration and usage of a solid scattering and absorbing phantom for near infra red spectroscopy. *University of London, University College London (United Kingdom).*, 25:pp377–445, 1994.
- [60] Stryland E.W.V., M. Williams D.R. Bass, and W.L. Wolfe. Handbook of optics volume ii devices, measurements. *Handbook of Optics Volume II Devices, Measurements, and Properties 2nd edition by Michael Bass, Eric W. Van Stryland, David R. Williams, William L. Wolfe New York, NY: McGraw-Hill, INC, 1995.*
- [61] J. Eichler, J. Knof, and H. Lenz. Measurements on the depth of penetration of light in tissue, radiat. environ. *Biophys*, 14:239–242, 1977.
- [62] Stryland E.W.V., M. Williams D.R. Bass, and W.L. Wolfe. Handbook of optics volume ii devices, measurements. *Handbook of Optics Volume II Devices, Measurements, and Properties 2nd edition by Michael Bass, Eric W. Van Stryland, David R. Williams, William L. Wolfe New York, NY: McGraw-Hill, INC, 1995.*
- [63] Imai D.-Mizuno S. Maki H. Shinozaki O. Tanikawa, Y. and Y. Yamada. Design and fabrication of a solid simplified head phantom. *In Optical Tomography and Spectroscopy of Tissue: Theory, Instrumentation, Model, and Human Studies II*, Vol. 2979:pp. 429–436, 1997.
- [64] Chung DE, Wysock JS, Lee RK, Melamed SR, Kaplan SA, and Te AE. Outcomes and complications after 532 nm laser prostatectomy in anticoagulated patients with benign prostatic hyperplasia. 186(3):977–81, 2011.
- [65] H. Abdussamad Abbas and G.E Triplett. Infrared transmission characteristics and laser tissue interaction of albino pigskin using pulsed nir laser light. *International Scholarly Research Notices*, 2013.
- [66] Germon T.J.-Barnett N.J. Manara A.R. Young, A.E. and R.J Nelson. Behaviour of near-infrared light in the adult human head: implications for clinical near-infrared spectroscopy. *British journal of anaesthesia*,, 84(1):pp.38–42, 2000.
- [67] C.S. Enwemeka. Attenuation and penetration of visible 632.8 nm and invisible infra-red 904nm light in soft tissues. *Laser Therapy*, 13(1):95–101, 2000.

- 
- [68] Ansam M. Salman, Amal F. Jaffar, Alaa Ayyed, and Jabur Al-Taie. Studying of laser tissue interaction using biomedical tissue. *Al-Nahrain Journal for Engineering Sciences*, 20(4):894–903, 2017.
  - [69] B.W. Pogue and M.S. Patterson. Review of tissue simulating phantoms for optical spectroscopy, imaging and dosimetry. *Journal of Biomedical Optics*, 11(4):041102, 2006.
  - [70] Ishimiaru A. Wave propagation and scattering in random media. *New York: Academic Press*, 1, 1978.
  - [71] Daniel J. E. "optical sensing for tissue differentiation". 18 November 1978.
  - [72] Ansari MA and Mohajerani E. Mechanisms of laser-tissue interaction: I. optical properties of tissue. *J Lasers Med Sci*, 2(3):119–25, 2011.
  - [73] Bass M. Handbook of optics volume i: Fundamentals, techniques, and design 2nd ed. united stated of america: Mc graw-hill.
  - [74] Valery V. Tuchin. Tissue optics and photonics: Light-tissue interaction. *J. of Biomedical Photonics and Eng*, 1(1):3–21, 2015.
  - [75] Adriana Taddeucci, Fabrizio Martelli, Marco Barilli, Marco Ferrari, and Giovanni Zaccanti. Optical properties of brain tissue. *JOURNAL OF BIOMEDICAL OPTICS*, 1(1):117–123, (JANUARY 1996).
  - [76] C. A Alter S. L Jacques and S. A Prahl. Angular dependence of hene laser light scattering by human dermis. *Laser Life Sci*, pages 309–334, 1987.
  - [77] M. Essenpreis P. Van der Zee and D. T Delpy. Optical properties of brain tissue. *Proc SPIE 1888*, pages 454–465, 1993.
  - [78] R. Marchesini, A. Bertoni, S. Andreola, E. Melloni, and A. E. Sichirollo. Ex-tinction and absorption coefficients and scattering function of human tissue in vitro. *Appl. Op*, 28(12):2318–2324, 1989.
  - [79] G. Zaccanti and P. Brusaglioni. Method of measuring the phase function of a turbid medium in the small scattering angle range. *Appl. Opt*, 28(11):2156–2164, 1989.
  - [80] W.F. Cheong, Prahl S.A., and A.J. Welch. A review of the optical properties of biological tissues. *IEEE journal of quantum electronics*, 26(12):2166–2185, 1990.
  - [81] T. Johansson. Applications of laser spectroscopy to analytical chemistry, environmental monitoring and medicine. *Dissertation thesis, Lund Institute of Technology, Lund, Sweden*, 2002.

- 
- [82] M. J. C. van Gemertand, A. J. Welch, and H. Kogelnik. Optical thermal response of laser-irradiated tissue. 1995.
- [83] Wyman DR Patterson MS, Wilson BC. The propagation of optical radiation in tissue i models of radiation transport and their application. *Lasers in Med. Sci.*, pages pp155–68, 1991.
- [84] H. C van de Hulst. Multiple light scattering. *New York Academic*, 2, 1980.
- [85] Lapaeva L. G and Rogatkin D. A. Improved kubelka-munk approach for determination of tissues optical properties in biomedical noninvasive reflectance spectroscopy. in saratov fall meeting 2006: Coherent optics of ordered and random media vii. *International Society for Optics and Photonics.*, Vol. 6536:p. 65360Z, 2007 June.
- [86] Gershun A. A. Selected papers on photometry and illumination engineering. 1958.
- [87] S. A. Prahl, M. Keijzer, S. L. Jacques, and A. J. Welch. A monte carlo model of light propagation in tissue. *SPIE Institute Series*, Vol. IS(5):102, 1989.
- [88] A. N. Witt. Multiple scattering in reflection nebulae i. a monte carlo approach. *Astrophys. J*, vol. S35:pp. 1–6, 1977.
- [89] Shusen Xie, Hui Lj, Buhong ja Wei Zheng, and Zhiwei Huang. Determination of optical properties of normal and carcinomatous lung tissues at violet and red wavelengths. *The International Society for Optical Engineering*, 2002.
- [90] Bass M. Handbook of optics volume ii: Devices, measurements, and properties 2nd ed. *United States of America: McGraw-Hill, inc.*, 1995.
- [91] Chen J Svaasand L.O Warloe T Gierexsky K.E Peng Q, Juzeniene A and Moan J. Lasers in medicine. *Reports on Progress in Physics*, 71(5):pp.056701, 2008.
- [92] Kolarsick P.A, Kolarsick M.A, and C Goodwin. Anatomy and physiology of the skin. *Dermatology Nurses' Association*, 3(4):pp.203–213, 2011.
- [93] J Kanitakis. Anatomy, histology and immunohistochemistry of normal human skin. *European Journal of Dermatology*, 12(4):390–401, 2002.
- [94] Masayuki Yagi and Yoshikazu Yonei. Glycative stress and skin aging. *Glycative Stress Research*, 5(1):050– 054, 2018.
- [95] J. M. Murkin and M. Arango. Near-infrared spectroscopy as an index of brain and tissue oxygenation. *British Journal of Anaesthesia*, 103:i3–i13, 2009.

- 
- [96] Shahabi L Amirlak B. Skin anatomy. 2017.
- [97] Biga LM. Anatomy and physiology. the integumentary system 5.1: layers of the skin. 2019.
- [98] M. T. Prange and S. S. Margulies. Regional, directional, and age-dependent properties of the brain undergoing large deformation. *J. Biomech. Eng.*, 124(2):pp. 244–252, 2002.
- [99] K. B. Arbogast and S. S. Margulies. Material characterization of the brainstem from oscillatory shear tests. *J. Biomech.*, 31(8):pp. 801–807, 1998.
- [100] Niederhuber JE. Cancer of the central nervous system. in: Abelloff’s clinical oncology. 6th ed. elsevier. 2020.
- [101] Herms F. Basset-Seguin N. Update in the management of basal cell carcinoma. *Acta Derm Venereol.*, 100(11), 2020.
- [102] Sloane E. Anatomy and physiology: an easy learner. *Jones and Barlett learning*, 1994.
- [103] Y. Watanabe and C. Constantinou. Phantom materials in radiology. *Encyclopedia of medical devices and instrumentation*, 2006.
- [104] Koval G, Blair G, and Jacques SL. In vivo determination of optical properties of normal and tumor tissue with white light reflectance and an empirical light transport model during endoscopy. *Journal of Biomedical Optics*, 10(3), 2005.
- [105] Popov A.P. Bykov A.V. Kinnunen M. Jedrzejewska-Szczerska M. Wrobel, M.S. and V.V. Tuchin. Multi-layered tissue head phantoms for noninvasive optical diagnostics. *Journal of Innovative Optical Health Sciences*, 8(03):p.1541005, 2015.
- [106] Lentsch G.R. Trieu B. Ponticorvo A. Saager-R.B. Kennedy, G.T. and A.J. Durkin. Design and fabrication of solid phantoms for nir water fraction studies. In *Design and Quality for Biomedical Technologies X*, Vol. 10056:pp. 41–46, 2017.
- [107] E. Casassa, A. Sarquis, and C. Van Dyke. *Journal of Chemical Education*, 63(1):57, 1986.
- [108] Di Ninni, Fabrizio Martelli, and Giovanni Zaccanti. The use of india ink in tissue-simulating phantoms. *Optics express*, 18(26):26854–26865, 2010.
- [109] Amina S. Muhammad A. Hina A. Omowumi-K.T. Abolanle, K.A.A. and Sunday O.O Omowumi, O.A. Brain tumor: An overview of the basic clinical manifestations and treatment. *Glob. J. Cancer Ther*, 6(1):038–041, 2020.

- 
- [110] L. Fass. Imaging and cancer: a review. . *Mol Oncol*, 2:115–152, 208.
  - [111] Baleato-Gonzalez S. Padhani A.R. Luna-Alcalá A. Vallejo-Casas J.A. Sala E. Vilanova J.C. Koh D.M. Herranz-Carnero M. Garcia-Figueiras, R. and H.A Vargas. Insights imaging. 10(1):1–35, 2019.
  - [112] Maisey M.N.-Townsend D.W. Valk P.E. Maisey-M. N Bailey, D.L. Positron emission tomography. *Springer-Verlag, London*, 2005.
  - [113] D.J. Brenner and E.J Hall. Computed tomography an increasing source of radiation exposure. *N Engl J Med*, 357(22):2277–2284, 2007.
  - [114] Song-A. W. Huettel, S. A. and G McCarthy. Functional magnetic resonance imaging. *Sinauer Associates, Sunderland, United States.*, 2004.
  - [115] M Gu. Advanced optical imaging theory. *Springer, Berlin, Heidelberg.*, 2000.
  - [116] Veeravagu A.-Hsu A.R. Hou, L.C. and V.C Tse. *Neurosurg Focus.*, 20(4):E5, 2006.
  - [117] Liu Y.-Berezin M.Y. Achilefu S Solomon, M. Optical imaging in cancer research: basic principles, tumor detection, and therapeutic monitoring. *Med Princ Pract.*, 20(5):397–415, 2011.
  - [118] S. J. Yeager D. Emelianov-S.Y M. Mehrmohammadi, M. Yoon. *Curr Mol Imaging.*, 2:89–105, 2013.
  - [119] H. H. Kato and T Ishida. Development of an agar phantom adaptable for simulation of various tissues in the range 5-40 mhz (hyperthermia treatment of cancer). *Phys Med Biol.*, 37(2):221–226, 1987.
  - [120] D.N. Hopkins. Determination of the linear attenuation coefficients and build-up factors of mcp-96 alloy for use in tissue compensation and radiation protection. *MSc Dissertation in Physics, Ball State University, Indiana.*, 2010.
  - [121] Shapey J. Maneas E. Saeed S.R.-Bradford R. Ourselin-S. Vercauteren T. Mackle, E. C. and A.E Desjardins. Patient-specific polyvinyl alcohol phantom fabrication with ultrasound and x-ray contrast for brain tumor surgery planning. *J. Vis. Exp.*, 161, 2020.
  - [122] Kennedy B. F. Kennedy K.M. Bisailon C.E.-Curatolo A. Campbell-G. Pazos V. Lamouche, G. and D. D Sampson. Review of tissue simulating phantoms with controllable optical, mechanical and structural properties for use in optical coherence tomography. *Biomed Opt Express.*, 3(6):1381, 2012.

- 
- [123] Price B.D. Gibson A.P. Hebden, J.C. and G. Royle. A soft deformable tissue-equivalent phantom for diffuse optical tomography. *Phys. Med. Biol.*, 51(21):5581–5590, 2006.
- [124] Zhu Y. Wang J. Jiang C. Guo, K. and J. Yu. Characterizing the viscoelastic properties of a tissue-mimicking phantom for ultrasound elasticity imaging studies. *IOP Conf. Ser.: Mater. Sci. Eng.*, 490(2):022–035, 2019.
- [125] Keisuke M. Kuroki K. Liu L. Inoue-K. T. Hayase-T. Kosukegawa, H. and O. Makoto. Measurements of dynamic viscoelasticity of poly (vinyl alcohol) hydrogel for the development of blood vessel biomodeling. *J. Fluid Sci. Technol.*, 3(4):533–543, 2008.
- [126] Caldera F. Poli T. Oscar C Riedo, C. Poly(vinyl alcohol)-borate hydrogels with improved features for the cleaning of cultural heritage surfaces. *Herit Sci.*, 3(23), 2015.
- [127] Ding A.Z. Azman N. Awang M. N. A. Yusoff, A. N. and H. Abdul Manan. Homogeneity and stability of poly (vinyl alcohol) slime phantom with different borax concentration. *ECS J. Solid State Sci. Technol*, 27(1 and 2):51–67, 2019.
- [128] Tulip J. Arnfield, M.R. and M.S McPhee. Optical propagation in tissue with anisotropic scattering. *IEEE Trans Biomed Eng.*, 35:372–385., 1988.
- [129] G. Zaccanti and P Brusciaglioni. Method of measuring the phase function of a turbid medium in the small scattering angle range. *App. Opt.*, 28:2156–2164, 1989.
- [130] J. Pu, Y. Chen and W Wang. Investigation of scattering coefficients and anisotropy factors of human cancerous and normal prostate tissues using mie theory. *Proc. SPIE*, 8941, 2014.
- [131] Muller P. J. Wilson, B.C. and J.C Yanche. Instrumentation and light dosimetry for intra-operative photodynamic therapy (pdt) of malignant brain tumours. *Phys. Med. Biol.*, 31(2):125–133, 1986.
- [132] P.J Muller and B.C Wilson. An update on the penetration depth of 630 nm light in normal and malignant human brain tissue in vivo. *Phys. Med. Biol.*, 31(11):1295–1297, 1986.
- [133] L.O. Svaasand and R Ellingsen. Optical properties of human brain. *Photochem. Photobiol*, 38(3):293–299, 1983.

- 
- [134] Anbil S. Bulin A. L. Obaid G. Ichikawa M. Mallidi, S. and T Hasan. Beyond the barriers of light penetration: Strategies, perspectives and possibilities for photodynamic therapy. *Theranostics*, 6(13):2458–2487, 2016.
  - [135] A.P. Gibson J.C. Hebden, B.D. Price and G. Royle. A soft deformable tissue-equivalent phantom for diffuse optical tomography. *Physics in Medicine and Biology*, 51(21):5581, 2006 Oct 16.
  - [136] R.S. Poston D.D. Royston and S.A. Prahl. Optical properties of scattering and absorbing materials used in the development of optical phantoms at 1064 nm. *J Biomed Opt.*, 1(1):110–6, 1996 Jan.
  - [137] A. M Ivory F. Leek G.P. Liney Y. Liu P. Miloro R. Rai A. Robinson A.J. Shih C.K McGarry, L.J Grattan and B. Zeqiri. Tissue mimicking materials for imaging and therapy phantoms: a review. *Phys. Med. Biol*, 65, 2020.
  - [138] M. Zellweger N. Utke D. Braichotte J. P. Ballini G. Wagnières, S. Cheng and H. van den Bergh. An optical phantom with tissue-like properties in the visible for use in pdt and fluorescence spectroscopy. *Phys Med Biol*, 42(7):1415–26, 1997.
  - [139] B. Lamien H.R. Orlande S. Eibner R.A Jaime, R.L Basto and O. Fudym. Fabrication methods of phantoms simulating optical and thermal properties. *Procedia Engineering*, 59:30–36, 2013.
  - [140] L. T. Tan B. D. Price, A. P. Gibson and G. J. Royle. An elastically compressible phantom material with mechanical and x-ray attenuation properties equivalent to breast tissue. *Phys. Med. Biol*, 55(4):1177–1188, 2010.
  - [141] G. Liao S. Gravelyn M. Schmitt K. Badu L. Heroïn N. Zulina, O. Caravaca and M. J. Gora. “colon phantoms with cancer lesions for endoscopic characterization with optical coherence tomography,”. *Biomed. Opt. Express* 12, pages 955–968, 2021.
  - [142] K.M. Kennedy C.E. Bisailon A. Curatolo G. Campbell G. Lamouche, B.F. Kennedy and D.D Sampson V. Pazos. Review of tissue simulating phantoms with controllable optical, mechanical, and structural properties for use in optical coherence tomography. *Biomed Opt Express*, 3(6):1381–1398, 2012.
  - [143] D. V. Zlatev J. C. Liao G. T. Smith, K. L. Lurie and A. K. Ellerbee Bowden. Multimodal 3d cancer-mimicking optical phantom. *Biomed Opt Express*, 7(2):648–662., 2016.

- 
- [144] G. Burçin. Design and fabrication of silicone-based composite tissue-mimicking phantoms for medical training. *PhD Thesis, Sabanci University*, 7(2), 2018.
- [145] D. Kuo D. J. Cuccia F. Ayers, A. Grant and A. J. Durkin. Fabrication and characterization of silicone-based tissue phantoms with tunable optical properties in the visible and near-infrared domain. san jose, california, usa. *In Proceedings of the international society for optics and photonics SPIE 6870.*, 7(2), February 21 (2008).
- [146] C. Cooper M.L. Killian B.A Ogunnaike G. McIlvain, E. Ganji and C.L. Johnson. Reliable preparation of agarose phantoms for use in quantitative magnetic resonance elastography. *J Mech Behav Biomed Mater.*, 97:65–73, 2019.
- [147] M. Firbank and D.T. Delpy. A design for a stable and reproducible phantom for use in near-infrared imaging and spectroscopy. *Phys. Med. Biol.*, 38:847–853, 1993.
- [148] M. Adel Sayah O. F. Farhat M. S. Ahmad A. A. Oglat, M. Alshipli and A. Abuelsamen. Fabrication and characterization of epoxy resin added rhizophora spp. particleboards as phantom materials for computer tomography (ct) applications. *J. Adhes*, pages 1 – 18, 2021.
- [149] N. Azman M.N.A. Awang A.N Yusoff, A.Z. Ding and H.A Manan. Homogeneity, and stability of polyvinyl alcohol slime phantom with different borax concentration. *J Solid State Sci Technol*, 27(1 and 2):51–67, 2019.
- [150] S. Sha. Evaluation of prone breast pet/ct imaging using phantoms. *Master's thesis, Duke University*, 2019.
- [151] S. Sha. Evaluation of prone breast pet/ct imaging using phantoms. *Master's thesis, Duke University*, 2019.
- [152] S. A. Prahl W. F. Cheong and A. J. Welch. A review of the optical properties of biological tissues. *IEEE J. Quantum Electron*, 26(12):2166–2185, 1990.
- [153] A. Pérez S. Stolik, J.A Delgado and L. Anasagasti. Measurement of the penetration depths of red and near-infrared light in human “ex vivo” tissues. *J Photochem Photobiol B*, 57(2-3):90–93, 2000.
- [154] L.O. Svaasand R.C. Haskell Y. Tadir S.J. Madsen, P. Wyss and B.J. Tromberg. Determination of the optical properties of the human uterus using frequency-domain photon migration and steady-state techniques. *Phys Med Biol.*, 39(8):1191–202, 1994.



- [155] C. P. Lowdell I. Driver and D. V. Ash. "in vivo measurement of the optical interaction coefficients of human tumors at 630 nm,". *Phys Med Biol.*, 36(6):805–813, 1991.
- [156] P.J. Muller B.C. Wilson and J.C Yanch. Instrumentation and light dosimetry for intra-operative photodynamic therapy (pdt) of malignant brain tumours. *Phys Med Biol.*, 31(2):125–33, 1986.
- [157] B. Farina S. Tomatis M. Lualdi, A. Colombo and R. Marchesini. A phantom with tissue-like optical properties in the visible and near-infrared for use in photomedicine. *Laser Surg. Med.*, 28(3):237–243, 2001.